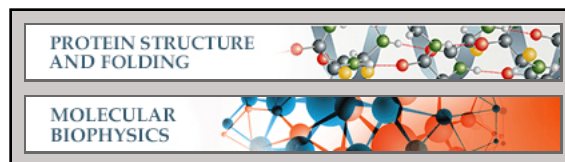


**Protein Structure and Folding:
Biophysical and Structural
Characterization of the
Thioredoxin-binding Domain of Protein
Kinase ASK1 and Its Interaction with
Reduced Thioredoxin**



Dalibor Kosek, Salome Kylarova, Katarina
Psenakova, Lenka Rezabkova, Petr Herman,
Jaroslav Vecer, Veronika Obsilova and Tomas
Obsil

J. Biol. Chem. 2014, 289:24463-24474.

doi: 10.1074/jbc.M114.583807 originally published online July 17, 2014

Access the most updated version of this article at doi: [10.1074/jbc.M114.583807](https://doi.org/10.1074/jbc.M114.583807)

Find articles, minireviews, Reflections and Classics on similar topics on the [JBC Affinity Sites](#).

Alerts:

- [When this article is cited](#)
- [When a correction for this article is posted](#)

[Click here](#) to choose from all of JBC's e-mail alerts

This article cites 44 references, 18 of which can be accessed free at
<http://www.jbc.org/content/289/35/24463.full.html#ref-list-1>

Biophysical and Structural Characterization of the Thioredoxin-binding Domain of Protein Kinase ASK1 and Its Interaction with Reduced Thioredoxin*

Received for publication, May 22, 2014, and in revised form, July 15, 2014. Published, JBC Papers in Press, July 17, 2014, DOI 10.1074/jbc.M114.583807

Dalibor Kosek^{‡§1}, Salome Kylarova^{‡§1}, Katarina Psenakova^{‡§}, Lenka Rezabkova[‡], Petr Herman[¶], Jaroslav Vecer[¶], Veronika Obsilova[§], and Tomas Obsil^{‡§2}

From the [‡]Department of Physical and Macromolecular Chemistry, Faculty of Science, Charles University in Prague, 12843 Prague, the [§]Institute of Physiology, Academy of Sciences of the Czech Republic, 14220 Prague, and the [¶]Institute of Physics, Faculty of Mathematics and Physics, Charles University in Prague, 12116 Prague, Czech Republic

Background: Thioredoxin is a physiological inhibitor of ASK1.

Results: The catalytic motif of thioredoxin is essential for its binding to ASK1 and the interaction does not involve intermolecular disulfide bonds.

Conclusion: Thioredoxin-binding domain of ASK1 is a rigid domain that interacts with reduced thioredoxin through a large binding interface.

Significance: Structural basis of the interaction between ASK1 and reduced thioredoxin.

Apoptosis signal-regulating kinase 1 (ASK1), a mitogen-activated protein kinase kinase kinase, plays a key role in the pathogenesis of multiple diseases. Its activity is regulated by thioredoxin (TRX1) but the precise mechanism of this regulation is unclear due to the lack of structural data. Here, we performed biophysical and structural characterization of the TRX1-binding domain of ASK1 (ASK1-TBD) and its complex with reduced TRX1. ASK1-TBD is a monomeric and rigid domain that forms a stable complex with reduced TRX1 with 1:1 molar stoichiometry. The binding interaction does not involve the formation of intermolecular disulfide bonds. Residues from the catalytic WCGPC motif of TRX1 are essential for complex stability with Trp³¹ being directly involved in the binding interaction as suggested by time-resolved fluorescence. Small-angle x-ray scattering data reveal a compact and slightly asymmetric shape of ASK1-TBD and suggest reduced TRX1 interacts with this domain through the large binding interface without inducing any dramatic conformational change.

Apoptosis signal-regulating kinase 1 (ASK1)³ (MAP3K5), a member of the mitogen-activated protein kinase kinase family, activates c-Jun N-terminal kinase and p38 MAP kinase signaling pathways in response to various stress stimuli, including oxidative stress, endoplasmic reticulum stress, and calcium ion influx (1–3). ASK1 plays a key role in the pathogenesis of

multiple diseases including cancer, neurodegeneration, and cardiovascular diseases and is considered a promising therapeutic target (reviewed by Ref. 4). Human ASK1 consists of 1,374 amino acids with the serine/threonine kinase domain located in the middle of the molecule flanked by two coiled-coil (CC) motifs, which are important for homo-oligomerization of ASK1 (5, 6). ASK1 under non-stress conditions forms a homo-oligomer by direct interaction through the C-terminal CC domain and interacts with several other proteins including thioredoxin-1 (TRX1) and the 14-3-3 protein, thus forming a high molecular mass complex called ASK1 signalosome (1, 7, 8). Both TRX1 and the 14-3-3 protein are physiological inhibitors of ASK1. In response to oxidative stress they dissociate from ASK1, this allows the homo-oligomerization and recruitment of tumor necrosis factor receptor-associated factors 2 and 6 to the N-terminal region of ASK1 and accelerates the autophosphorylation of Thr⁸³⁸ within the activation loop resulting in ASK1 activation (1, 9, 10).

Thioredoxins (TRXs) are small dithiol oxidoreductases ubiquitously present in species ranging from archaea to mammals. TRXs perform various biological functions including the reduction of protein disulfide bonds in the reducing cellular compartments, the supply of reducing equivalents to redox enzymes, and the regulation of several transcription factors and proteins through either a direct reduction of their cysteine groups or different mechanisms (reviewed by Ref. 11). TRXs are involved in the regulation of NF- κ B (12), the *Escherichia coli* T7 polymerase complex (13), or Jab-1 (14). The TRX molecule consists of a five-stranded β -pleated sheet that forms a hydrophobic core surrounded by four α -helices. The highly conserved redox catalytic motif ³¹WCGPC³⁵ links the second β -strand to the second α -helix and the two cysteine residues within this sequence (Cys³² and Cys³⁵ in human TRX1) are responsible for TRX-dependent redox activity (15).

TRX1 interacts with the ASK1 region located between residues 46 and 277 and this interaction is thought to inhibit the

* This work was supported by Czech Science Foundation Project 14-10061S, Grant Agency of Charles University Project 568912, and Academy of Sciences of the Czech Republic Research Project RVO:67985823 of the Institute of Physiology.

¹ Both authors contributed equally.

² To whom correspondence should be addressed: Faculty of Science, Charles University, Hlavova 8, 12843 Prague, Czech Republic. Tel.: 420-221951303; Fax: 420-224919752; E-mail: obsil@natur.cuni.cz.

³ The abbreviations used are: ASK1, apoptosis signal-regulating kinase 1; ASK1-TBD, TRX1-binding domain of ASK1; AUC, analytical ultracentrifugation; CC, coiled-coil; SAXS, small angle x-ray scattering; SV, sedimentation velocity; TRX1, thioredoxin 1.

activation of ASK1 through blocking its homo-oligomerization via an adjacent N-terminal CC motif (1, 9). The Cys²⁵⁰ residue, located within this region of ASK1, is crucial for the oxidative stress-dependent signaling downstream of ASK1 and likely involved in TRX1 binding (16, 17). However, the precise mechanism of TRX1 binding to ASK1, as well as its dissociation, is still unclear due to the lack of structural data on the TRX-binding domain of ASK1 (ASK1-TBD). Several studies suggested that under oxidative stress conditions TRX1 is oxidized on Cys³² and Cys³⁵ within the redox catalytic motif and the formation of an intramolecular disulfide bond between these two cysteine residues causes the dissociation of TRX1 from ASK1 through an unknown mechanism, thus allowing the activation of ASK1 (1, 9, 18). It is, however, unclear whether the interaction between TRX1 and ASK1 is based on the non-covalent interactions only or if it also involves the formation of intermolecular disulfide bond(s). The latter possibility was suggested by Nadeau *et al.* (17, 19) who proposed another mechanism for ASK1 activation. The authors suggest the oxidative stress induces the formation of intermolecular disulfide bonds between ASK1 molecules and this oxidation is required for the activation of ASK1 kinase function. In their model, the interaction between TRX1 and ASK1 involves a formation of intermolecular disulfide bond(s) and the TRX1-dependent inhibition of ASK1 is mediated by its thiol reductase activity because only the oxidized and disulfide bond-containing oligomeric form of ASK1 enables activation.

To better understand the interaction between TRX1 and ASK1, we prepared and performed detailed biophysical and structural characterization of the isolated ASK1-TBD (sequence 88–302) and its complex with reduced TRX1. The results show that ASK1-TBD is a monomeric and rigid domain that forms a stable complex with reduced TRX1 with 1:1 molar stoichiometry. The binding interaction does not involve the formation of intermolecular disulfide bonds. Residues Cys³² and Cys³⁵ as well as Trp³¹ from the catalytic WCGPC motif of TRX1 are essential for complex stability with Trp³¹ being directly involved in binding interaction as suggested by time-resolved tryptophan fluorescence. SAXS data revealed a compact and slightly asymmetric shape of ASK1-TBD and suggest reduced TRX1 interacts with this domain through the large binding interface without inducing any dramatic conformational change. Molecular modeling indicated the TRX1 binding site is located close to the N-terminal end of a ~50 residue long α -helix, which forms the C terminus of ASK1-TBD. Our results also show the ASK1 residue Cys²⁵⁰ is likely located either at or in close vicinity of TRX1-binding surface.

EXPERIMENTAL PROCEDURES

Expression and Purification of TRX-binding Domain of ASK1—DNA encoding four different N-terminal fragments of human ASK1 (residues 46–302, 88–302, 46–322, and 88–322) were ligated into pST39 (20) using the XbaI and BamHI sites and pRSFDuet-1 (Novagen) using BamHI and PstI sites. Modified pRSFDuet-1 containing the sequence of the His₆-tagged GB1 domain of protein G inserted into the first multiple cloning site was a gift of Evzen Boura (Institute of Organic Chemistry and Biochemistry AS CR, Prague, Czech Republic). ASK1-

(88–302) (in pST39) was expressed as a C-terminal His₆ tag fusion protein by leakage expression at 30 °C for 20 h and purified from *E. coli* BL21 (DE3) cells using chelating Sepharose Fast Flow (GE Healthcare Life Sciences) according to standard protocols. Eluted ASK1-TBD was dialyzed against buffer containing 20 mM Tris-HCl (pH 7.5), 200 mM NaCl, 1 mM EDTA, 5 mM DTT, 10% (w/v) glycerol and purified using size-exclusion chromatography on a HiLoad 26/60 Superdex 75 column (GE Healthcare Life Sciences). All mutants were generated by using the QuikChange site-directed mutagenesis kit (Stratagene) and mutations were confirmed by sequencing.

Expression and Purification of TRX1—The expression construct for human TRX1 (C73S mutant) was a gift of Katja Becker (Justus-Liebig-Universität, Giessen, Germany). TRX1 was expressed as an N-terminal His₆ tag fusion protein by isopropyl 1-thio- β -D-galactopyranoside induction for 20 h at 30 °C and purified from *E. coli* BL21 (DE3) cells using chelating Sepharose Fast Flow (GE Healthcare Life Sciences) according to standard protocols. Eluted TRX1 was dialyzed against buffer containing 20 mM Tris-HCl (pH 7.5), 200 mM NaCl, 1 mM EDTA, 5 mM DTT, 10% (w/v) glycerol and purified using size-exclusion chromatography on Superdex 75 10/300 GL column (GE Healthcare Life Sciences). All mutants were generated by using the QuikChange site-directed mutagenesis kit (Stratagene), and mutations were confirmed by sequencing.

Preparation of Oxidized TRX1—TRX1 (140 μ M in buffer containing 20 mM Tris-HCl (pH 7.5) and 200 mM NaCl) was incubated with 100-fold molar excess of H₂O₂ in a total volume of 500 μ l for 15 min at 37 °C (21). Oxidation reaction was stopped by adding 2 units of catalase (Sigma).

Time-resolved Fluorescence Measurements—Fluorescence intensity and anisotropy decays were measured on a time-correlated single photon counting apparatus, as described previously (22). Tryptophan emission was excited at 298 nm by a tripled output of the Ti:Sapphire laser. Tryptophan fluorescence was isolated at 355 nm by a combination of monochromator and a stack of UG1 and BG40 glass filters (Thorlabs) placed in front of the input slit. Fluorescence decays were typically accumulated in 1024 channels with a time resolution of 50 ps/channel until 10⁵ counts in the decay maximum were reached. Samples were placed in a thermostatic holder, and all experiments were performed at 23 °C in a buffer containing 20 mM Tris-HCl (pH 7.5), 200 mM NaCl, and 5 mM DTT. The TRX1 concentration was 10 μ M; the ASK1-TBD concentration was 30 μ M (or 10 μ M in experiments with Trp-containing mutants of ASK1-TBD). Fluorescence decays were assumed to be multiexponential according to the formula,

$$I(t) = \sum_i \alpha_i \cdot \exp(-t/\tau_i) \quad (\text{Eq. 1})$$

where τ_i and α_i are the fluorescence lifetime components and the corresponding amplitudes, respectively. Emission decays $I(t)$ were analyzed by a maximum entropy method (23). The program yields a set of amplitudes, α_i , representing the lifetime distribution. Typically, we have chosen 100 lifetimes equidistantly spaced in a logarithmic scale, ranging from 20 ps to 20 ns. The mean emission lifetime was calculated as,

$$\tau_{\text{mean}} = \sum_i f_i \tau_i = \sum_i (\alpha_i \tau_i^2) / \sum_i (\alpha_i \tau_i) \quad (\text{Eq. 2})$$

where f_i are the fractional intensities of corresponding lifetime components. Fluorescence anisotropy $r(t)$ was obtained by a simultaneous reconvolution of parallel $I_{\parallel}(t)$ and perpendicular $I_{\perp}(t)$ polarized components. The anisotropies $r(t)$ were analyzed for a series of exponentials by a model-independent maximum entropy method without setting assumptions about the shape of the correlation time distributions (23),

$$r(t) = \sum_i \beta_i \cdot \exp(-t/\phi_i) \quad (\text{Eq. 3})$$

where amplitudes β_i represent the distribution of the correlation times ϕ_i . They are related to the initial anisotropy r_0 by the following formula.

$$\sum_i \beta_i = r_0 \quad (\text{Eq. 4})$$

Typically we used 100 correlation times equidistantly spaced in the logarithmic scale from 100 ps to 200 ns.

Analytical Ultracentrifugation (AUC)—Sedimentation velocity (SV) experiments were performed using a ProteomLab™ XL-I analytical ultracentrifuge (Beckman Coulter). Samples were dialyzed against buffer containing 20 mM Tris-HCl (pH 7.5), 200 mM NaCl, and 2 mM 2-mercaptoethanol before analysis. Experiments with oxidized TRX1 were performed in buffer containing 20 mM Tris-HCl (pH 7.5), and 200 mM NaCl. The buffer density, viscosity, and partial specific volume of all proteins were estimated using the program SEDNTERP. SV experiments of ASK1-TBD and TRX1 were conducted at various loading concentrations and molar ratios in charcoal-filled Epon centerpieces with 12-mm optical path length, 20 °C, and 48,000 rpm rotor speed (An-50 Ti rotor, Beckman Coulter). All sedimentation profiles were recorded with interference optics. The diffusion-deconvoluted sedimentation coefficient distributions $c(s)$ were calculated from raw interference data using the software package SEDFIT. For experiments with mixtures of TRX1 and ASK1-TBD at various molar ratios, this procedure was followed by the integration of calculated distributions to determine the overall weight-averaged s -values (s_w). Constructed s_w isotherms were fitted with $A + B \rightleftharpoons AB$ model as implemented in the software package SEDPHAT with known s_w values of individual components as prior knowledge. Resulting parameters were verified and loading concentrations were corrected using global Lamm equation modeling also implemented in SEDPHAT software (24, 25).

Small Angle X-ray Scattering—SAXS data were collected on the European Molecular Biology Laboratory (EMBL) P12 beamline on the storage ring PETRA III (Deutsches Elektronen Synchrotron (DESY), Hamburg, Germany). The ASK1-TBD, TRX1, and ASK1-TBD·TRX1 complex were measured in concentration ranges of 1.2–4.6, 1.4–12, and 1.5–11.9 mg ml⁻¹, respectively. The data were averaged after normalization to the intensity of the transmitted beam, and the scattering of buffer was subtracted using PRIMUS (26). The forward scattering $I(0)$ and the radius of gyration R_g were evaluated using the Guinier

approximation (27). These parameters were also computed from the entire scattering pattern using the program GNOM (28), which provides the distance distribution functions $P(r)$ and the maximum particle dimensions D_{max} . The solute apparent molecular mass (MM_{exp}) was estimated by comparison of the forward scattering with that from reference solutions of bovine serum albumin (molecular mass 66 kDa). *Ab initio* molecular envelopes were computed by the program DAMMIN (29), which represents the protein by an assembly of densely packed beads. Multiple iterations of DAMMIN were averaged using the program DAMAVER (30). The averaged envelopes were then used as final SAXS structures.

Circular Dichroism Measurements—The far-UV CD spectra were measured in a quartz cuvette with an optical path length of 1 mm (Starna, USA) using a J-810 spectropolarimeter (Jasco, Japan). The conditions of the measurements were as follows: a spectral region of 200–260 nm, a scanning speed of 10 nm min⁻¹, a response time of 8 s, a resolution of 1 nm, a bandwidth of 1 nm, and a sensitivity of 100 mdeg. The final spectrum was obtained as an average of 5 accumulations. The spectra were corrected for a baseline by subtracting the spectra of the corresponding polypeptide-free solution. The CD measurements were conducted at 22 °C in buffer containing 20 mM Tris-HCl (pH 7.5), 200 mM NaCl, and 2 mM 2-mercaptoethanol. The ASK1-TBD and TRX1 concentrations were 8 μM. After baseline correction, the final spectra were expressed as a mean residue ellipticities Q_{MRW} (deg cm² dmol⁻¹ res⁻¹) and calculated using the equation,

$$[Q]_{\text{MRW}} = \frac{\theta_{\text{obs}} M_w}{c l N_R 10} \quad (\text{Eq. 5})$$

where θ_{obs} is the observed ellipticity in mdeg, c is the protein concentration in mg ml⁻¹, l is the path length in cm, M_w is the protein molecular weight, and N_R is the number of amino acids in the protein (31). The near-UV CD spectra were measured in a quartz cuvette with an optical path length of 1 cm (Starna, USA) in a spectral region of 250–320 nm. The final spectrum was obtained as an average of 15 accumulations. The ASK1-TBD and TRX1 concentrations were 26 μM.

Protein Structure Modeling—Because ASK1 sequence 88–302 does not show any homology to known structures, its structural models were created by *ab initio* modeling using I-TASSER (32), Phyre2 (33), and Robetta (34) servers. The agreement between the calculated scattering curves of theoretical models and the experimental SAXS data were evaluated using CRY SOL (35).

RESULTS

Preparation of ASK1-TBD and Its Complex with TRX1—It has previously been shown ASK1-TBD is located between residues 46 and 277 within the N-terminal part of ASK1 (1, 9). We expressed several constructs of human ASK1 consisting of residues 46–302, 88–302, 46–322, and 88–322 with either the C-terminal His₆ tag or the N-terminal His₆-GB1 tag and tested their solubility and stability. Only the construct consisting of the C terminally His-tagged ASK1 sequence 88–302 exhibited sufficient expression yield, solubility, and stability, and thus was used for further studies. To avoid TRX1 homo-dimerization

due to the intermolecular disulfide bond formation by the non-active site Cys⁷³ residue under high protein concentrations, we decided to use the mutant C73S of human TRX1 (denoted in this work as TRX1), rather than the wild-type protein, throughout this work. This mutation has no effect on the activity or the structure of human TRX1 (36, 37).

Biophysical Characterization of the Interaction between ASK1-TBD and Reduced TRX1—The AUC was used for the biophysical characterization of prepared ASK1-TBD and its interaction

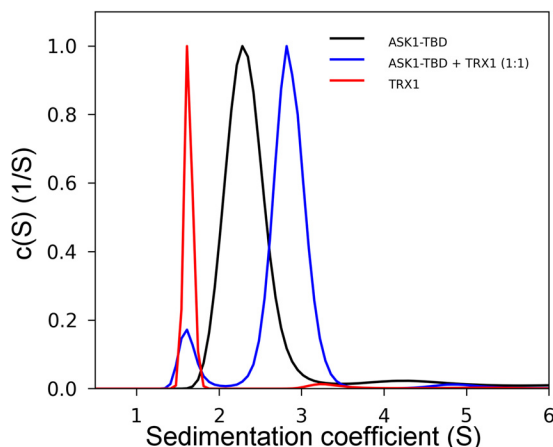


FIGURE 1. **Sedimentation velocity ultracentrifugation.** The normalized continuous sedimentation coefficient distributions, $c(s)$, for ASK1-TBD alone (black), TRX1 alone (red), and ASK1-TBD and TRX1 mixed in the molar ratio 1:1 (blue) are shown. All experiments were performed under reducing conditions.

with TRX1 under reducing conditions. The normalized continuous sedimentation coefficient distributions $c(s)$ from the SV AUC experiments revealed the reduced TRX1 and ASK1-TBD form a complex with a weight-averaged sedimentation coefficient (corrected to 20.0 °C and the density of water), $s_{w(20,w)}$, of 3.0 S, whereas TRX1 and ASK1-TBD alone show single peaks with $s_{w(20,w)}$ values of 1.6 and 2.4 S, respectively (Fig. 1). The observed values of $s_{w(20,w)}$ for TRX1 and ASK1-TBD correspond to molecular masses of ~ 12 and ~ 25 kDa, respectively, suggesting both proteins are monomers in solution (theoretical molecular mass of TRX1 and ASK1-TBD are 12.99 and 25.57 kDa, respectively). In addition, the observed value of $s_{w(20,w)}$ of 3.0 S for the ASK1-TBD-TRX1 complex corresponds to molecular mass of ~ 33 kDa, suggesting the 1:1 molar stoichiometry of the complex (theoretical molecular mass = 38.6 kDa). To obtain the apparent equilibrium dissociation constant (K_D) of the ASK1-TBD-TRX1 complex, a range of concentrations and different molar ratios of ASK1-TBD and reduced TRX1 were examined using SV AUC (Fig. 2A). Analysis of the isotherm of weight-averaged s values (s_w isotherm) as a function of TRX1 concentration revealed the best-fit K_D of $0.3 \pm 0.1 \mu\text{M}$ using a 1:1 Langmuir binding model. This confirms the ASK1-TBD and TRX1 form a complex with a 1:1 molar stoichiometry. Because all SV AUC experiments were performed in the presence of the reducing agent 2-mercaptoethanol and obtained SV AUC data can be adequately fitted using the reversible Langmuir-type kinetic model ($A + B \rightleftharpoons AB$), it is reasonable to assume the interaction between ASK1-TBD and TRX1 under

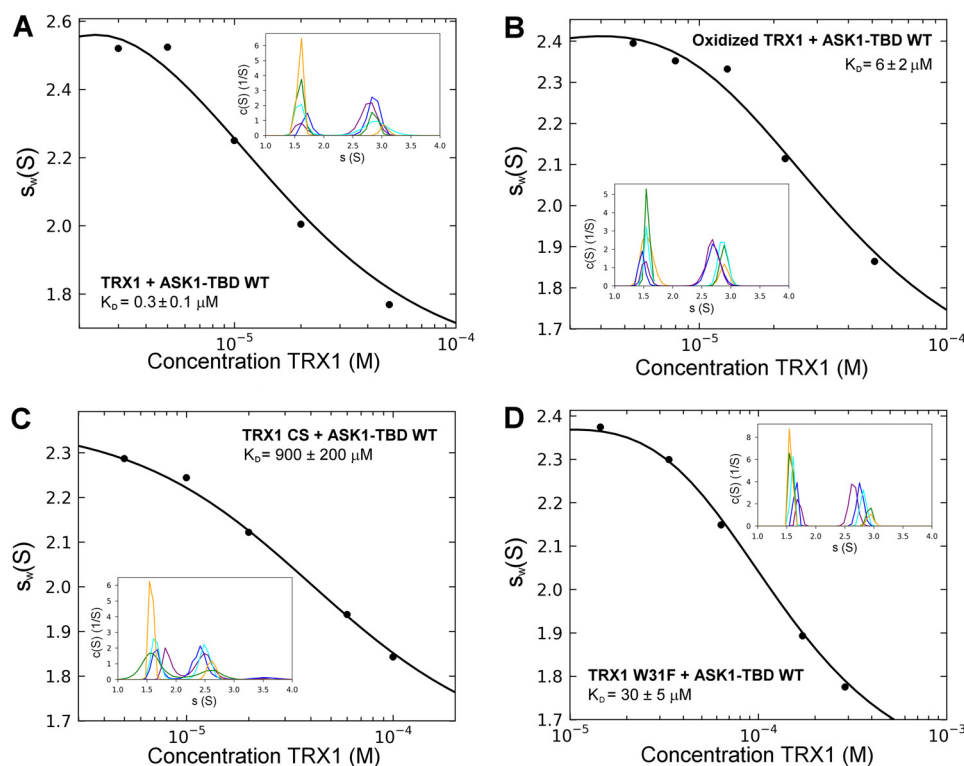


FIGURE 2. **Sedimentation velocity ultracentrifugation.** A, isotherm of weight-averaged sedimentation coefficients s_w (s_w isotherm) obtained from SV experiments of mixtures of ASK1-TBD WT ($5 \mu\text{M}$) and reduced TRX1 ($3\text{--}50 \mu\text{M}$). B, the s_w isotherm obtained from SV experiments of mixtures of ASK1-TBD WT ($5 \mu\text{M}$) and oxidized TRX1 ($3\text{--}50 \mu\text{M}$). TRX1 was oxidized by incubation with a 100-fold molar excess of H_2O_2 for 15 min at 37 °C (21). C, the s_w isotherm obtained from SV experiments of mixtures of ASK1-TBD WT ($20 \mu\text{M}$) and reduced TRX1 CS mutant ($5\text{--}100 \mu\text{M}$). D, the s_w isotherm obtained from SV experiments of mixtures of ASK1-TBD W31F mutant ($20 \mu\text{M}$) and reduced TRX1 ($15\text{--}290 \mu\text{M}$). The insets show the sedimentation coefficient distributions $c(s)$ of mixtures of ASK1-TBD and TRX1 at various concentrations and molar ratios underlying the s_w data points.

reducing conditions does not involve the formation of intermolecular disulfide bonds. No significant amount of the mixed disulfide ASK1-TBD-TRX1 complex was observed even upon the 36-h long incubation of an equimolar mixture of ASK1-TBD and TRX1 in the absence of the reducing agents (Fig. 3), further corroborating that intermolecular disulfide bonds are not involved in complex formation.

Oxidized TRX1 Binds ASK1-TBD with Significantly Lower Binding Affinity Compared with Reduced TRX1—Several studies have shown the oxidation of TRX1 disrupts its binding to ASK1 (1, 9, 18). Therefore, we next examined the interaction between oxidized TRX1 and ASK1-TBD using SV AUC. Oxidized TRX1 was prepared by incubation with 100-fold molar excess of H₂O₂ for 15 min at 37 °C. Such oxidation was previously shown to produce well defined TRX1 containing two-disulfide bridges (Cys³²-Cys³⁵, Cys⁶²-Cys⁶⁹) (21). The *s_w* isotherm was determined over a range of loading concentrations of oxidized TRX1 and ASK1-TBD (Fig. 2B). The analysis of

obtained data revealed oxidized TRX1 exhibits a significantly lower binding affinity for ASK1-TBD compared with reduced TRX1 with the best-fit *K_D* of $6 \pm 2 \mu\text{M}$ using a 1:1 Langmuir binding model, confirming the oxidation of TRX1 disrupts its interaction with ASK1.

Structural Integrity of the Catalytic WCGPC Motif of TRX1 Is Essential for the Binding to ASK1-TBD—The redox-inactive mutant TRX1-CS where both Cys residues (Cys³² and Cys³⁵) from the catalytic ³¹WCGPC³⁵ motif were replaced by Ser does not bind to ASK1 (1, 9, 18). To test whether this is also true for the interaction with the isolated ASK1-TBD, SV AUC experiments were conducted and the *s_w* isotherm was determined over a range of loading concentrations of TRX1-CS and ASK1-TBD (Fig. 2C). These data revealed negligible binding affinity (*K_D* was estimated to be of $\sim 900 \pm 200 \mu\text{M}$) for the TRX1-CS mutant, in agreement with previous reports. In addition, the catalytic ³¹WCGPC³⁵ motif of human TRX1 contains a conserved Trp³¹, which is located in close proximity to the catalytic Cys residues and undergoes a conformational change upon oxidation of Cys³² and Cys³⁵ or their mutation to Ser (37, 38). Both oxidized TRX1 and the TRX1-CS mutant exhibit significantly reduced binding to ASK1 (1, 9, 18), suggesting possible involvement of Trp³¹ in this interaction. To check the importance of this residue, TRX1 mutant W31F was prepared and its binding to ASK1-TBD was investigated using SV AUC (Fig. 2D). Indeed, the obtained SV data revealed significantly lower binding affinity of the W31F mutant to ASK1-TBD (*K_D* of $30 \pm 5 \mu\text{M}$), confirming the importance of this residue for ASK1-TBD-TRX1 complex stability.

Trp³¹ of TRX1 Is Directly Involved in the Interaction with ASK1-TBD—Because Trp³¹ is the only tryptophan residue in human TRX1 and ASK1-TBD does not contain any tryptophan residue, the time-resolved tryptophan fluorescence intensity and anisotropy decay measurements were used to further study the involvement of Trp³¹ in TRX1 binding to ASK1-TBD. Both time-resolved fluorescence intensity and anisotropy decays were analyzed using a singular-value decomposition maximum entropy method as previously described (23). Complex formation significantly increased the mean excited state lifetime (τ_{mean}) of Trp³¹ from 1.62 to 3.34 ns (Table 1). This could reflect the ASK1-induced conformational change in TRX1, which affects interaction of Trp³¹ with its surroundings. The observed increase in τ_{mean} could also reflect a direct interaction of ASK1-TBD with this residue, reducing its contacts with the polar environment or altering quenching interactions in its vicinity.

Measurements of the emission anisotropies revealed significantly different mobility of TRX1 Trp³¹ in the presence and

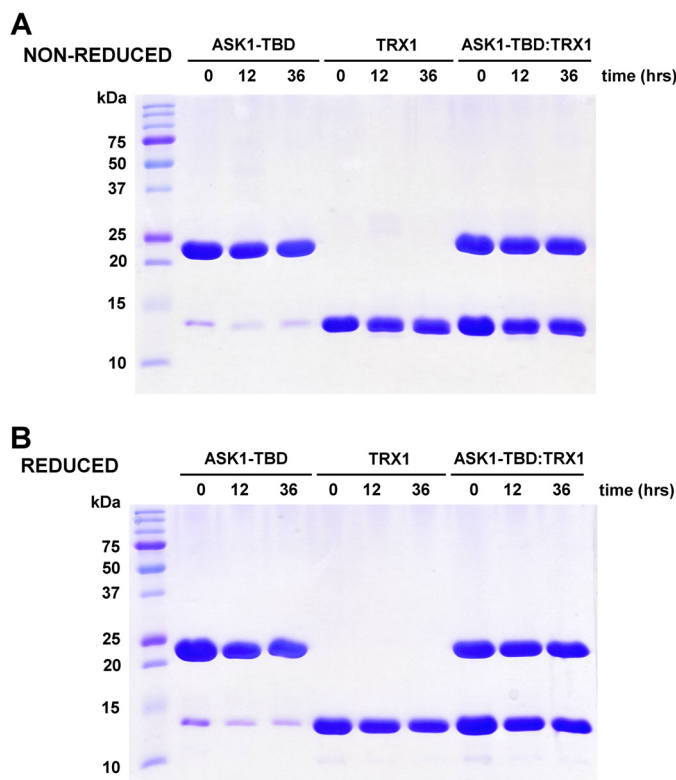


FIGURE 3. Non-reduced (A) and reduced (B) 15% SDS-PAGE of purified ASK1-TBD, TRX1, and their mixture (with 1:1 molar ratio) after the incubation in a buffer containing 20 mM Tris-HCl (pH 7.5), 200 mM NaCl, and 1 mM EDTA (and no reducing agents) for 0, 12, and 36 h at 4 °C.

TABLE 1
Summary of time-resolved fluorescence measurements of Trp³¹ of TRX1

Sample	$\tau_{\text{mean}}^{a,b}$	$\beta_1^{c,d}$	$\phi_1^{c,e}$	$\beta_2^{c,d}$	$\phi_2^{c,e}$	$\beta_3^{c,d}$	$\phi_3^{c,e}$	$\beta_{\text{long}}^{c,d}$	$\phi_{\text{long}}^{c,e}$
TRX1 alone	ns		ns		ns		ns		ns
TRX1 + ASK1-TBD WT	1.62	0.018	<0.1	0.069	1.7			0.133	10
TRX1 + ASK1-TBD C250S	3.34					0.079	3.3	0.141	30
	4.52	0.026	<0.1	0.024	1.3	0.034	3.8	0.136	38

^a The mean fluorescence lifetime (τ_{mean}) was calculated using Equation 2.

^b S.D. = 0.05 ns.

^c The fluorescence anisotropies $r(t)$ were analyzed for series of exponentials (Equation 3), where the amplitudes β_i represent the distribution of the correlation times ϕ_i . Initial anisotropy of Trp³¹ for all samples is $r_0 = 0.22 \pm 0.01$. Amplitudes β_1 were calculated as $\beta_1 = r_0 - (\beta_2 + \beta_3 + \beta_{\text{long}})$ for each sample.

^d S.D. = 0.005.

^e S.D. = 15%.

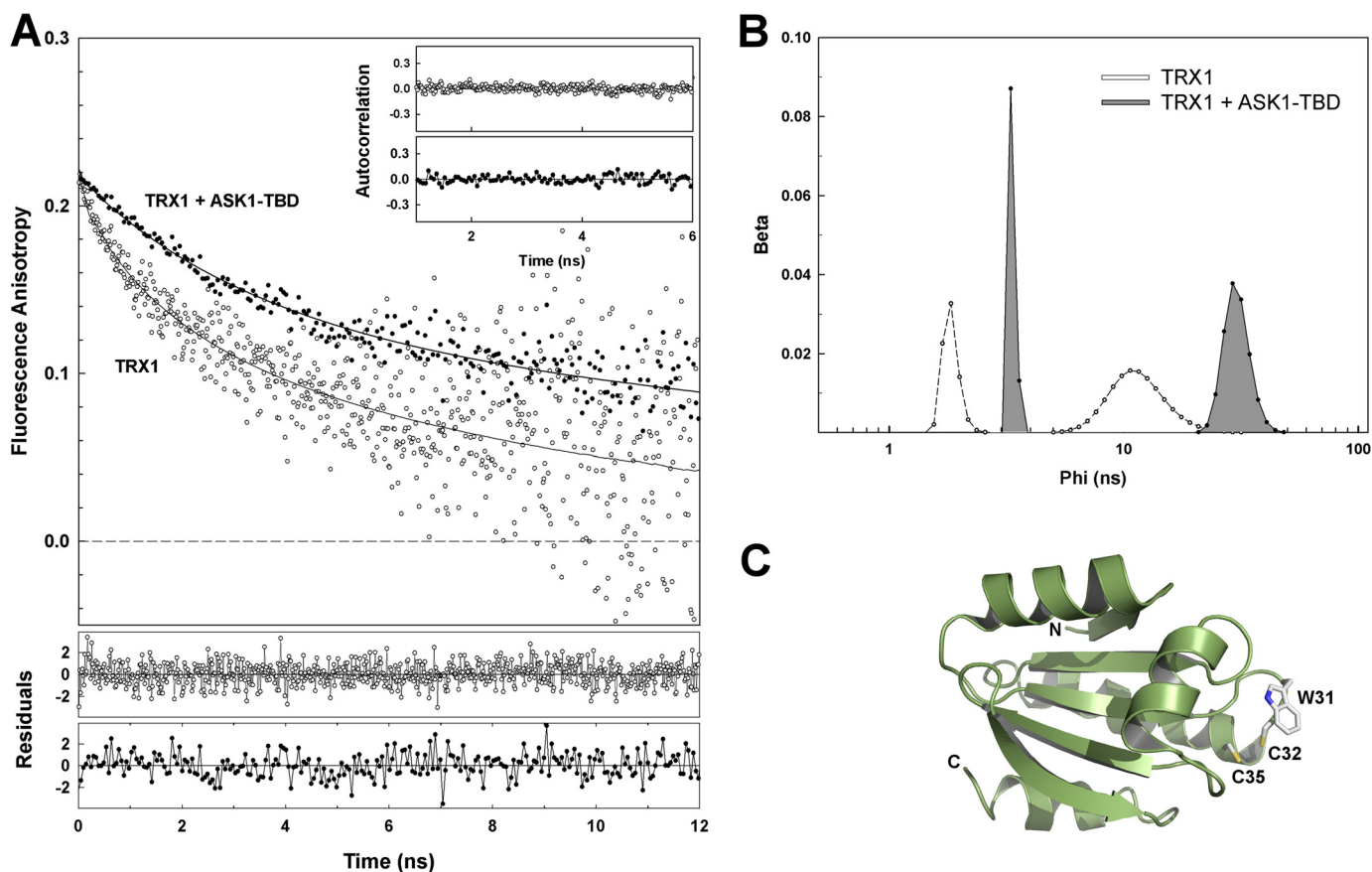


FIGURE 4. Time-resolved TRX1 Trp³¹ fluorescence anisotropy decay measurements. A, TRX1 Trp³¹ fluorescence anisotropy decays constructed from the raw polarized decay data for TRX1 in the absence (○) and presence (●) of ASK1-TBD. The weighted residuals of both fits (gray, TRX1 alone; black, TRX1 + ASK1-TBD) are shown in the lower panels. The fit quality is also demonstrated by the autocorrelation functions shown in the inset (gray, TRX1 alone; black, TRX1 + ASK1-TBD). B, rotational correlation time distributions of Trp³¹ (TRX1) in the absence and presence of ASK1-TBD. The unresolved component with very short correlation time ($\phi_1 < 100$ ps) observed in the fluorescence anisotropy decay of TRX1 alone is not shown. C, solution structure of reduced human TRX1 (38). Residues Trp³¹, Cys³², and Cys³⁵ are shown as sticks.

absence of ASK1-TBD as documented by the raw data presented in Fig. 4A. Visual inspection of early depolarization phases in Fig. 4A clearly reveals fluorescence of Trp³¹ depolarizes significantly faster in the absence than in the presence of ASK1-TBD. The depolarization rate can be directly related to the rotational freedom of the Trp³¹ residue. The slower depolarization means slower and/or more restricted local and segmental motion of the fluorophore (39). From this point of view, the binding of ASK1-TBD reduces segmental flexibility of the catalytic motif where Trp³¹ is located. This observation correlates with the decrease in τ_{mean} (Table 1), which could indicate the motional restriction of the catalytic motif results in lower accessibility of Trp³¹ to polar environment and/or suppressed quenching interactions in its vicinity. Rigorous data analysis is in full agreement with the visual observation. TRX1 alone revealed two classes of short correlation times, one very short unresolved ($\phi_1 < 100$ ps) and the second, ϕ_2 , close to 1.7 ns (Table 1, Fig. 4B). In addition, the third correlation time $\phi_{\text{long}} = 10$ ns was also present in the data. The recovered ϕ_{long} can be assigned to the overall rotational motion of TRX1, and its value is close to what would be expected for a globular protein with a molecular mass about 13 kDa (39). Complex formation resulted in a disappearance of the fastest decay component with the correlation time ϕ_1 belonging to the fastest Trp³¹ motion. At

the same time, the correlation time corresponding to the segmental motion increased from 1.7 to 3.3 ns ($\phi_2 \rightarrow \phi_3$, Table 1 and Fig. 4B). Complex formation also slightly decreased the sum of amplitudes of the fast anisotropy decay components β_{short} ($\beta_{\text{short}} = \beta_1 + \beta_2 + \beta_3$) indicating angular restriction of the motion. Altogether, these changes can be interpreted as a significantly reduced segmental flexibility of the catalytic motif, where Trp³¹ is located, upon the TRX1 binding to ASK1-TBD. In addition, the observed increase in the longest correlation time ϕ_{long} from 10 to 30 ns likely reflects the higher molecular mass of the complex compared with TRX1 alone and its value corresponds with the expected molecular mass of the complex (38.6 kDa). These results suggest Trp³¹ from the catalytic motif of TRX1 could be directly involved in its interaction with ASK1-TBD.

ASK1-TBD Is a Rigid Domain That Does Not Change Its Structure Upon the Binding of TRX1—To investigate the structural flexibility of ASK1-TBD, the time-resolved tryptophan fluorescence intensity and anisotropy decay measurements of single tryptophan residues inserted at four different positions within the ASK1-TBD (Trp¹³², Trp¹⁷⁵, Trp²⁴², and Trp²⁷²) were performed. The sequence of ASK1-TBD does not contain any tryptophan residue; phenylalanines located at these positions were replaced by tryptophans. Results of these measure-

ments are listed in Table 2. It can be noticed that all four mutants showed relatively long τ_{mean} ranging from 4.22 to 5.35 ns, indicating that all four Trp residues are likely buried and inaccessible to the polar environment (40). The analysis of fluorescence anisotropy decays revealed bimodal correlation time distributions (Table 2) with small amplitudes of the fast rotational and segmental motion of the fluorophore (β_1), suggesting regions around all four Trp residues, especially Trp inserted at position 242, are rigid. These data suggest that ASK1-TBD is a compact and rigid domain.

Next, CD spectroscopy was used to check whether the binding of TRX1 affects the overall structure of ASK1-TBD. The deconvolution of CD spectra using the K2D method (41) indicated that ASK1-TBD contains ~35% of α , ~20% of β , and ~45% of random structure. This estimation is in agreement with the theoretical prediction using PSIPRED (35% α , 15% β , and 50% random structure) (42). The far-UV CD spectrum of the ASK1-TBD·TRX1 complex (with 1:1 molar stoichiometry) showed no significant difference when compared with the sum of the individual CD spectra of ASK1-TBD and TRX1 (Fig. 5A), suggesting no significant changes in overall secondary structure upon complex formation. The comparison of near-UV CD spectra that give us the information about the tertiary structure

reveal significant differences only in the region from 275 to 295 nm (Fig. 5B). Because the CD signal in this region arises from the environments of Tyr and Trp residues (43), it is likely that the observed differences mainly reflect the structural change in the vicinity of TRX1 Trp³¹ upon complex formation as has also been suggested by time-resolved tryptophan fluorescence experiments (Table 1 and Fig. 4).

Low-resolution Structure of ASK1-TBD and Its Complex with TRX1 Obtained from SAXS Measurements—SAXS was used to obtain the visual insight into the structure of ASK1-TBD and its complex with TRX1. The experimental SAXS curves from the ASK1-TBD·TRX1 complex and ASK1-TBD alone are shown in Fig. 6A. The absence of aggregation in both samples was confirmed by the inspection of the SAXS data and the linearity of the Guinier region (*inset* in Fig. 6A). The apparent molecular masses of ASK1-TBD and the ASK1-TBD·TRX1 complex were estimated by comparison of the forward scattering intensity $I(0)$ with that from reference solutions of bovine serum albumin (Table 3). The estimated mass of 37 kDa for the ASK1-TBD·TRX1 complex corresponds well to a 1:1 stoichiometry (theoretical molecular mass = 38.6 kDa) in agreement with the results from SV AUC. Values of the R_g calculated both from the slope of the Guinier plot and from the distance distribution ($P(r)$) function suggest the complex is more asymmetric compared with ASK1-TBD alone (Table 3). This was further confirmed by the $P(r)$ function, which revealed maximum dimensions (D_{max}) of ASK1-TBD alone and the ASK1-TBD·TRX1 complex to be 82 and 99 Å, respectively (Fig. 6B). These D_{max} values corroborate a more extended and asymmetric shape of the complex compared with ASK1-TBD alone.

To obtain the information about the shape of these molecules, the *ab initio* envelopes were calculated from the scattering data using the program DAMMIN (Fig. 6, C and D). The reconstructed envelopes consist of an average of at least 10 individual reconstructions and the individual envelopes agreed well with each other, as determined using normalized spatial discrepancy. Normalized spatial discrepancy is a measure of the degree each of the selected envelopes differs from one another.

TABLE 2
Summary of time-resolved fluorescence measurements of single tryptophan (W) mutants of ASK1-TBD

ASK1-TBD Trp mutant	$\tau_{\text{mean}}^{a,b}$	$\beta_1^{c,d}$	$\phi_1^{c,e}$	$\beta_2^{c,d}$	$\phi_2^{c,e}$
	ns		ns		ns
W132	4.62	0.033	2.7	0.190	18
W175	5.35	0.038	2.0	0.180	18
W242	4.94	0.020	5.0	0.192	18
W272	4.22	0.032	2.5	0.162	16
				0.013	Aggr. (>50)

^a The mean fluorescence lifetime (τ_{mean}) was calculated using Equation 2.

^b S.D. = 0.05 ns.

^c The fluorescence anisotropies $r(t)$ were analyzed for series of exponentials (Equation 3), where the amplitudes β_i represent the distribution of the correlation times ϕ_i .

^d S.D. = 0.005.

^e S.D. = 15%.

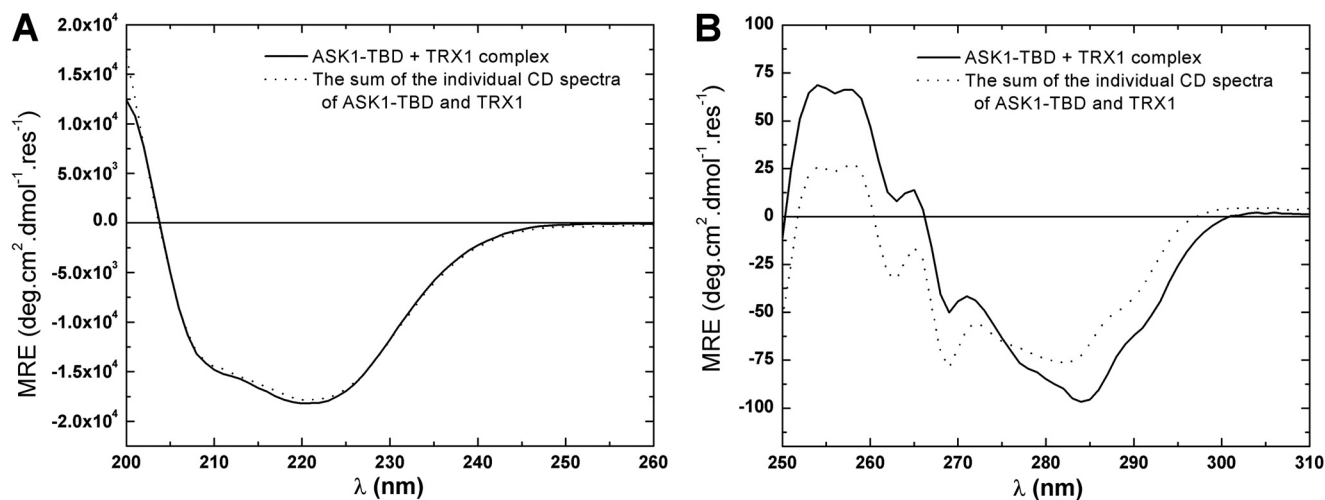


FIGURE 5. Circular dichroism measurements. A, the comparison of the far-UV CD spectrum of the ASK1-TBD·TRX1 complex (solid line) with the sum of the individual far-UV CD spectra of ASK1-TBD and TRX1 (dotted line). B, the comparison of the near-UV CD spectrum of the ASK1-TBD·TRX1 complex (solid line) with the sum of the individual near-UV CD spectra of ASK1-TBD and TRX1 (dotted line). Proteins were mixed with the 1:1 molar stoichiometry. The mean residue ellipticity (MRE) is plotted as a function of the wavelength.

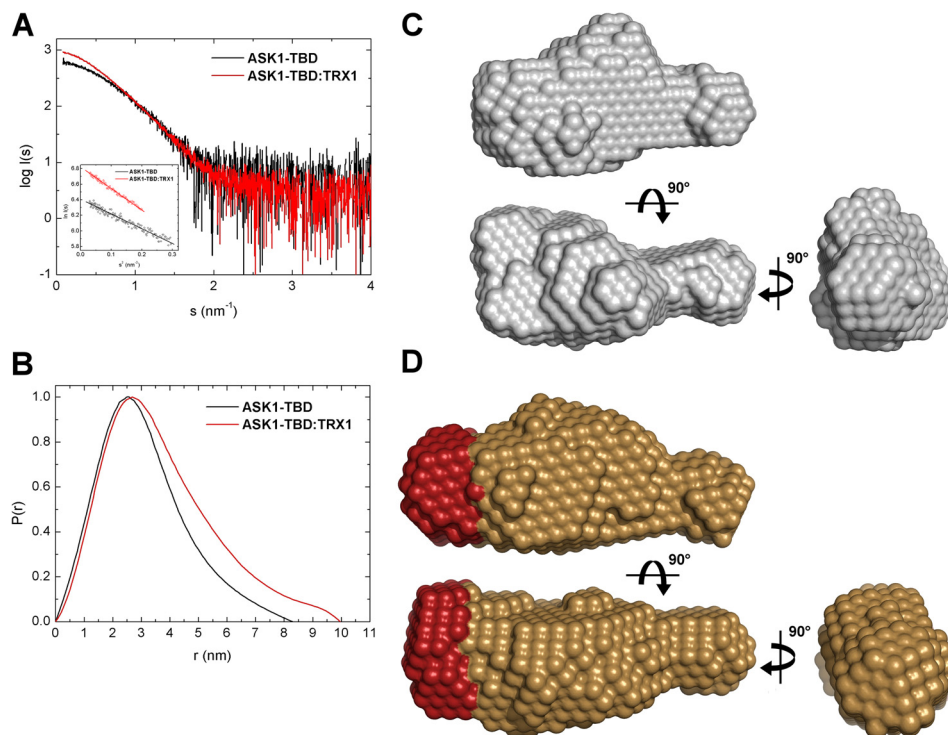


FIGURE 6. Structural characterization of ASK1-TBD and its complex with reduced TRX1 by SAXS. A, scattering intensity as a function of the scattering vector s ($s = 4\pi \sin(\theta)/\lambda$, where 2θ is the scattering angle and λ is the wavelength). Inset shows Guinier plots of ASK1-TBD and the ASK1-TBD-TRX1 complex at concentrations 2.3 and 6 mg/ml, respectively. B, distance distribution function $P(r)$. C, averaged and filtered DAMMIN shape envelope (spheres around the dummy residues) of ASK1-TBD. D, averaged and filtered DAMMIN shape envelope of the ASK1-TBD-TRX1 complex. The main difference between the envelope of the complex and those of ASK1-TBD alone is shown in red.

TABLE 3

Structural parameters determined from SAXS data

Sample	R_g^a	R_g^b	$M_{w,I(0)}^c$	D_{max}^d
	\AA		kDa	\AA
ASK1-TBD	23.7 ± 0.3	24.2 ± 0.2	~ 25	82
ASK1-TBD-TRX1	28.9 ± 0.2	29.3 ± 0.1	~ 37	99

^a Determined by Guinier approximation.

^b Determined from $P(r)$ function.

^c Estimated by comparison of the forward scattering intensity $I(0)$ with that from reference solutions of bovine serum albumin.

^d Determined by indirect Fourier transformation from SAXS data.

Values <1 are considered to indicate no systematic differences. Normalized spatial discrepancy values of 0.58 and 0.49 were obtained for envelopes of ASK1-TBD and the ASK1-TBD-TRX1 complex, respectively. The envelope for ASK1-TBD alone (Fig. 6C) shows this domain adopts a compact and slightly asymmetric conformation with one side being narrower than the other. The envelope of the complex (Fig. 6D) is similar and shows a more extended thicker part of the molecule, suggesting that TRX1 interacts with this thicker end of the ASK1-TBD molecule. The size ($\sim 20 \times \sim 35 \times \sim 30 \text{ \AA}$) and the shape of this additional area (shown in red in Fig. 6D) correspond well with the size and the shape of the TRX1 molecule. The comparison of both envelopes also suggests the interaction between TRX1 and ASK1-TBD is mediated through the large binding interface, rather than one or few contacts. In good agreement with results of CD measurements, the high similarity of obtained envelopes also indicates that TRX1 binding does not induce any dramatic structural change within ASK1-TBD, although we cannot rule out the possibility of a local conformational change that is beyond the resolution of this method.

Structural Modeling of the ASK1-TBD-TRX1 Complex—To further refine the structural details of ASK1-TBD and its complex with TRX1, a structural model of ASK1-TBD was generated. Because the sequence 88–302 of ASK1 lacks homology to any known structures, its models were created by *ab initio* modeling using I-TASSER, Phyre2, and Robetta servers (32–34). However, only one of the models calculated by the Robetta server showed reasonable agreement not only with the SAXS-based envelope (Figs. 7, A and B, the back-calculated scattering curve based on this model fits the SAXS data with χ^2 values of 0.91) but also with the secondary structure prediction and the results of time-resolved fluorescence measurements that suggested all Trp residues that replaced Phe residues at four different positions within ASK1-TBD are likely buried and located in relatively rigid areas (Table 2). The superposition of this model with the SAXS-based envelope is shown in Fig. 7A. The model indicates that the C-terminal part of ASK1-TBD contains a ~ 50 residue long α -helix that protrudes from the more spherical N-terminal part with the 3-layer α/β sandwich architecture. The comparison of SAXS-based envelopes suggests TRX1 interacts with the N-terminal bulkier part of ASK1-TBD. Fig. 7C shows a superposition of the SAXS envelope of the ASK1-TBD-TRX1 complex with its model, which was created by inserting a crystal structure of TRX1 (37) into the empty part of the complex envelope. The shape and size of the SAXS-based envelope allowed for the TRX1 molecule to be oriented by its catalytic WCGPC motif (Fig. 7C, shown in yellow) toward to ASK1-TBD consistent with the tryptophan fluorescence data, which suggested the involvement of Trp³¹ in binding to ASK1-

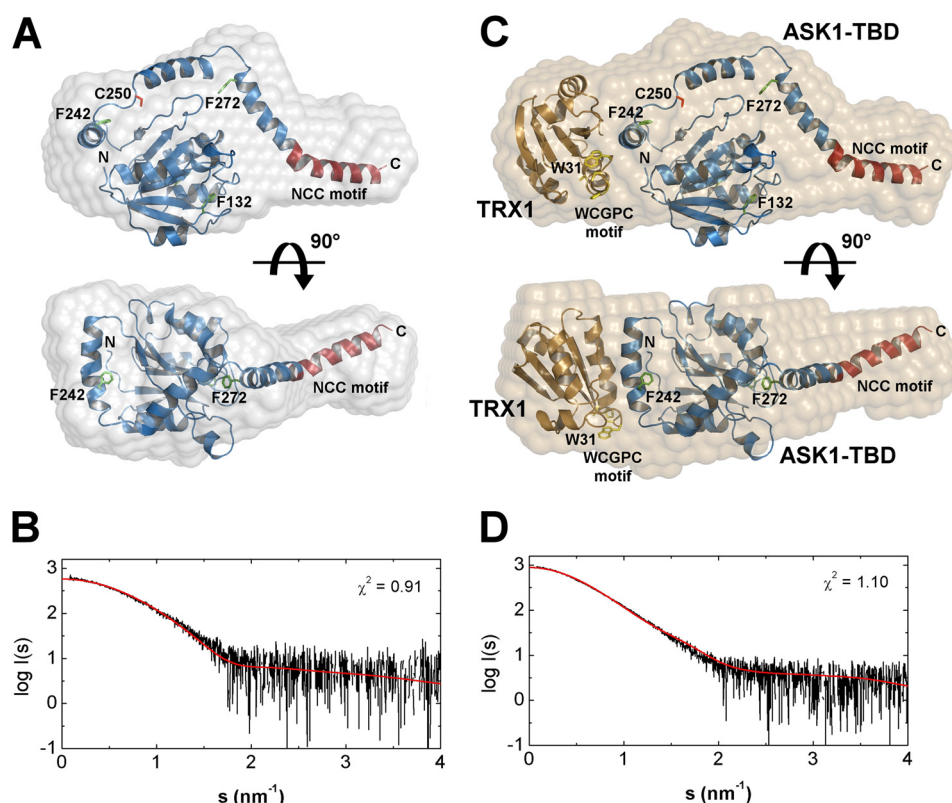


FIGURE 7. Superposition of SAXS envelopes with the *ab initio* models of ASK1-TBD and the ASK1-TBD-TRX1 complex. *A*, superposition of the SAXS envelope with the theoretical model of ASK1-TBD (sequence 88–302) obtained by *ab initio* modeling using Robetta (34). The N-terminal CC motif of ASK1 is shown in dark red. Phe residues that were mutated to Trp are shown in green. Cys²⁵⁰ is shown in red. *B*, comparison of the calculated scattering curve of the theoretical model of ASK1-TBD (red line) with the experimental scattering data (black line). *C*, superposition of the SAXS envelope with the model of the ASK1-TBD-TRX1 complex that was created using the theoretical model of ASK1-TBD and the crystal structure of human TRX1 (37). The catalytic ³¹WCGPC³⁵ motif of TRX1 is shown in yellow. *D*, comparison of the calculated scattering curve of the theoretical model of the ASK1-TBD-TRX1 complex (red line) with the experimental scattering data (black line).

TBD. The accuracy of this model was also assessed by calculating and comparing its theoretical SAXS scattering profile with the experimental scattering curve and the calculated scattering curve fitted the SAXS data well with χ^2 values of 1.10 (Fig. 7D).

ASK1 Residue Cys²⁵⁰ Is Located in the Vicinity of TRX1-binding Surface—The *ab initio* model of ASK1-TBD indicated that the TRX1-binding site is located in the vicinity of the Cys²⁵⁰ residue located at the N-terminal end of the long α -helix, which forms the C terminus of modeled ASK1-TBD (Fig. 7C). The mutation of this residue inhibits the interaction between ASK1 and TRX1 (16, 17). To check whether the same holds true for the isolated ASK1-TBD, mutant C250S was prepared and its interaction with TRX1 was characterized using both SV AUC and time-resolved fluorescence measurements. Analysis of the s_w isotherm as a function of reduced TRX1 concentration revealed that ASK1-TBD C250S exhibits a significantly lower binding affinity compared with WT with the best-fit K_D of $50 \pm 10 \mu\text{M}$ using 1:1 Langmuir binding model (Fig. 8A).

To further investigate the effect of the C250S mutation on the interaction between ASK1 and TRX1, time-resolved fluorescence measurements of Trp³¹ of TRX1 were performed. Measurements of the emission anisotropies revealed different hydrodynamic properties of TRX1 Trp³¹ when interacting with the ASK1-TBD C250S mutant compared with WT (Table 1 and Fig. 8B). Data analysis revealed four classes of correlation times, one unresolved and very short ($\phi_1 < 100$ ps), two longer corre-

sponding to segmental motions (ϕ_2 and ϕ_3 close to 1.3 and 3.8 ns, respectively), and the fourth correlation time $\phi_{\text{long}} = 38$ ns reflects the overall rotational motion of the complex (Table 1, Fig. 8B). The simultaneous presence of correlation times observed either for TRX1 alone (ϕ_1 and ϕ_2) or TRX1 bound to ASK1-TBD (ϕ_3) suggests an incomplete complex formation when only a portion of TRX1 is bound to ASK1-TBD C250S. This conclusion is fully consistent with results of SV AUC measurements showing that TRX1 interacts with ASK1-TBD C250S with weaker affinity compared with ASK1-TBD WT. Moreover, a significantly longer mean excited state lifetime of Trp³¹ was observed in this case. In particular, $\tau_{\text{mean}} = 4.52$ ns for the ASK1-TBD C250S-TRX1 complex compared with 3.34 ns for the ASK1-TBD WT-TRX1 complex. This suggests that Trp³¹ of TRX1 interacts with ASK1-TBD C250S by the altered way, likely as a result of either different conformations of ASK1-TBD or different interactions at the binding interface. Taken together, both SV AUC and time-resolved fluorescence measurements revealed the ASK1 Cys²⁵⁰ residue is likely located either at or in close vicinity of TRX1-binding site and is crucial for the interaction between ASK1 and TRX1.

DISCUSSION

In the present study, our main aim was to provide a structural insight into the interaction between ASK1 and reduced TRX1. TRX1, a ubiquitous oxidoreductase, was identified as a physiolog-

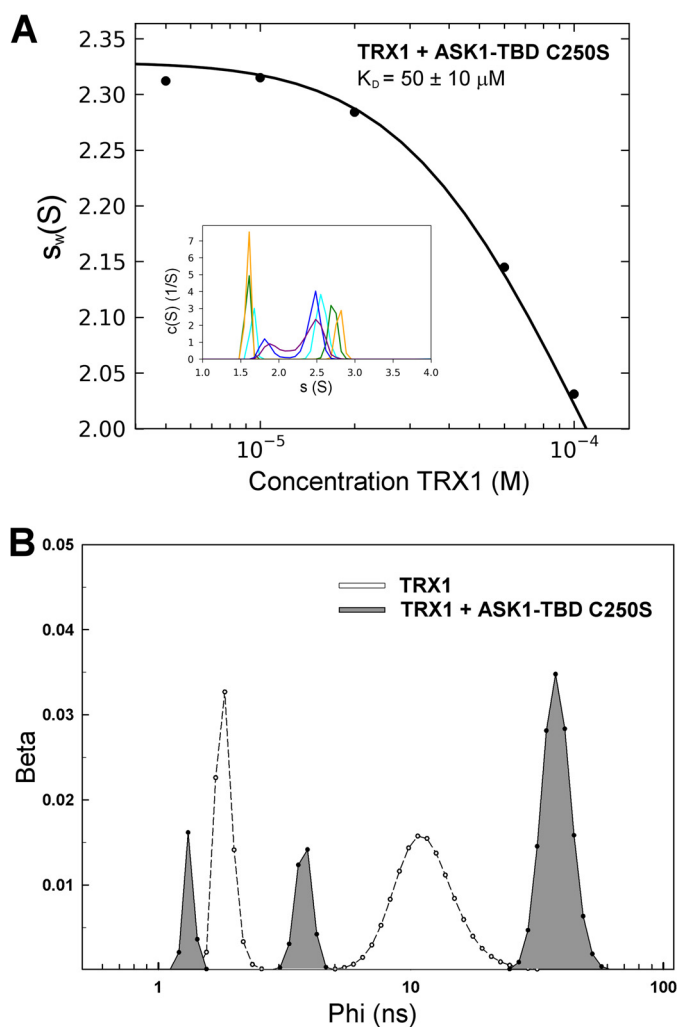


FIGURE 8. ASK1 residue Cys²⁵⁰ is important for the interaction between ASK1-TBD and TRX1. A, sedimentation velocity ultracentrifugation. The s_w isotherm obtained from SV AUC experiments of mixtures of ASK1-TBD C250S (20 μM) and TRX1 (5–100 μM). The inset shows the sedimentation coefficient distributions $c(s)$ of mixtures of ASK1-TBD C250S and TRX1 at various concentrations and molar ratios underlying the s_w data points. B, rotational correlation time distribution of Trp³¹ (TRX1) in the absence and presence of ASK1-TBD C250S. The unresolved component with very short correlation time ($\phi_1 < 100$ ps) observed in the fluorescence anisotropy decay of TRX1 alone is not shown.

ical inhibitor of ASK1, which interacts with the N-terminal region of ASK1 preventing homophilic oligomerization through the N-terminal CC domain of ASK1. Only the reduced form of TRX, but not the oxidized form where both Cys residues from the redox catalytic ³¹WCGPC³⁵ motif form an intramolecular disulfide bond, interacts with ASK1 (1, 9, 10, 18). However, the precise mechanisms of TRX1 binding to ASK1 as well as its dissociation are still unclear as no structural data are available on ASK1-TBD and its interaction with TRX1.

Screening of several constructs containing ASK1 sequences between residues 46 and 302 showed that only the C terminally His-tagged sequence 88–302 enables the preparation of a soluble and stable protein that binds reduced TRX1 with 1:1 molar stoichiometry and K_D of ~ 300 nM (Fig. 2A). On the other hand, oxidized TRX1 showed significantly lower binding affinity with K_D of $6 \pm 2 \mu\text{M}$ (Fig. 2B), confirming the oxidation of TRX1 hinders its interaction with ASK1. However, the mechanism

behind the lower binding affinity of oxidized TRX1 is still unclear. It has been suggested the oxidation of TRX1 generates an intramolecular disulfide bond between Cys³² and Cys³⁵ within the redox catalytic motif and this, in turn, causes the dissociation of TRX1 from ASK1 (1, 9, 18). This hypothesis is supported by the fact the redox inactive TRX1-CS mutant, in which both Cys³² and Cys³⁵ from the catalytic motif are replaced by Ser, does not bind to ASK1 (1, 9, 18). SV AUC experiments revealed that the TRX1-CS mutant exhibits negligible binding affinity for ASK1-TBD (with K_D of ~ 1 mM, Fig. 2C), confirming previous observations and suggesting these active site Cys residues play an important role in TRX1 binding to ASK1. In addition, our data also suggest that the interaction between ASK1-TBD and reduced TRX1 does not involve the formation of intermolecular disulfide bridges as SV AUC experiments were performed under reducing conditions and all obtained SV AUC data can be adequately fitted using the reversible Langmuir-type kinetic model.

Under strong oxidative conditions or at high protein concentrations human TRX1 forms homodimers covalently linked through the non-active site cysteine 73 (37). Because the TRX1 C73S mutant was used throughout this work to avoid formation of these homodimers, it is necessary to keep in mind data presented in this work cannot assess the potential role of this residue in the interaction between TRX1 and ASK1.

The catalytic motif of human TRX1 also contains a conserved tryptophan residue Trp³¹, which undergoes a subtle conformational change upon both TRX1 oxidation, when Cys³² and Cys³⁵ are disulfide linked, and the replacement of Cys³² and Cys³⁵ by Ser (the TRX1-CS mutant) (37, 38). Crystallographic analysis revealed that Trp³¹ is partially disordered in reduced form, but ordered in TRX1-CS and oxidized TRX1. This resemblance of TRX1-CS and oxidized TRX1 also likely contributes to the ability of the TRX1-CS mutant to act as a competitive inhibitor of thioredoxin reductase (44). Because both TRX1-CS and oxidized TRX1 were shown to be unable to bind to ASK1 (1, 9, 10, 18), it is entirely possible the similarity in the conformational behavior of Trp³¹ might contribute to their inability to bind to ASK1. Consistent with this hypothesis, results of our experiments strongly suggest that Trp³¹ is directly involved in TRX1 binding to ASK1-TBD. First, the W31F mutation significantly reduced TRX1 binding affinity for ASK1-TBD (Fig. 2D). Next, the time-resolved tryptophan fluorescence measurements showed the TRX1 binding to ASK1-TBD both increases τ_{mean} and suppresses the segmental dynamics of Trp³¹. In the free TRX1, Trp³¹ exhibits relatively short τ_{mean} and a fast emission depolarization, suggesting this residue is exposed to the solvent and highly mobile, in a good agreement with its surface-exposed location (Fig. 4C) as well as partially disordered nature observed in structural studies (37). The longer τ_{mean} and a slower and/or more restricted local and segmental motion of Trp³¹ in the presence of ASK1-TBD suggest the motional restriction of the catalytic motif and a lower accessibility of Trp³¹ to polar environment and/or suppressed quenching interactions in its vicinity upon complex formation (39, 40). Because Trp³¹ is located on the surface of the TRX1 molecule (Fig. 4C), it is reasonable to interpret observed changes as a direct involvement of this residue in TRX1 binding to ASK1-TBD.

The SAXS experiments revealed ASK1-TBD is monomeric in solution and adopts a compact and slightly asymmetric shape with one side being narrower than the other (Fig. 6C). The shape of the ASK1-TBD-TRX1 complex is similar but more extended within its thicker part (Fig. 6D). The comparison of obtained envelopes suggests that TRX1 interacts with the thicker end of the ASK1-TBD molecule through the large binding interface without inducing any dramatic structural change, although a local conformational change, which is beyond the resolution of this method, cannot be ruled out. *Ab initio* molecular modeling, although speculative as the 88–302 sequence of ASK1 lacks homology to any known structures, provided a structural model that shows reasonable agreement with the SAXS-based envelope, the secondary structure prediction, and the results of time-resolved tryptophan fluorescence measurements (Fig. 7, Table 2). This structural model suggests TRX1 interacts with the bulkier part of ASK1-TBD close to the N terminus of the long α -helix that protrudes from the more spherical part of ASK1-TBD and forms its C-terminal end. This long α -helix contains approximately one-half of the N-terminal CC motif of ASK1, based on the prediction using the COILS program (45), located between residues ~285 and 320 (shown in red in Fig. 7). It has been suggested the TRX1 binding to the N-terminal part of ASK1 blocks its homophilic interaction through this N-terminal CC motif that is required for ASK1 autophosphorylation and activation (9). Our structural model is consistent with this hypothesis as TRX1 binding close to the N-terminal end of this long α -helix might affect its conformation and its coiled-coil interactions. In addition, both SV AUC and the time-resolved fluorescence measurements suggested that ASK1 residue Cys²⁵⁰, which has been shown to be important for both TRX1 binding and the oxidative stress-dependent signaling downstream of ASK1 (16, 17), is located either at or in close vicinity of the TRX1-binding site (Fig. 8, Table 1) consistent with our structural model (Fig. 7).

Taken together, biophysical and structural characterization of the isolated TRX1-binding region of ASK1 revealed that this part of ASK1 is a monomeric and rigid domain that forms a stable equimolar complex with reduced TRX1. Residues from the catalytic ³¹WCGPC³⁵ motif of TRX1 are essential for TRX1 binding to ASK1-TBD and the interaction does not involve the formation of intermolecular disulfide bonds. Time-resolved tryptophan fluorescence suggested a direct involvement of Trp³¹ in the TRX1 binding to ASK1. SAXS data revealed a compact and slightly asymmetric shape of ASK1-TBD and suggested TRX1 interacts with this domain through the large binding interface without inducing any dramatic conformational change. Molecular modeling indicated the TRX1-binding site is located close to the N-terminal end of a ~50-residue long α -helix that forms the C terminus of ASK1-TBD. In addition, our results also show that ASK1 residue Cys²⁵⁰ is likely located either at or in close vicinity to the TRX1-binding surface.

Acknowledgment—We thank Dr. Karen Iorio for critical reading of the manuscript.

REFERENCES

- Saitoh, M., Nishitoh, H., Fujii, M., Takeda, K., Tobiume, K., Sawada, Y., Kawabata, M., Miyazono, K., and Ichijo, H. (1998) Mammalian thioredoxin is a direct inhibitor of apoptosis signal-regulating kinase (ASK) 1. *EMBO J.* **17**, 2596–2606
- Nishitoh, H., Matsuzawa, A., Tobiume, K., Saegusa, K., Takeda, K., Inoue, K., Hori, S., Kakizuka, A., and Ichijo, H. (2002) ASK1 is essential for endoplasmic reticulum stress-induced neuronal cell death triggered by expanded polyglutamine repeats. *Genes Dev.* **16**, 1345–1355
- Takeda, K., Matsuzawa, A., Nishitoh, H., Tobiume, K., Kishida, S., Nomiya-Tsuiji, J., Matsumoto, K., and Ichijo, H. (2004) Involvement of ASK1 in Ca²⁺-induced p38 MAP kinase activation. *EMBO Rep.* **5**, 161–166
- Kawarazaki, Y., Ichijo, H., and Naguro, I. (2014) Apoptosis signal-regulating kinase 1 as a therapeutic target. *Expert Opin. Ther. Targets* **18**, 651–664
- Tobiume, K., Saitoh, M., and Ichijo, H. (2002) Activation of apoptosis signal-regulating kinase 1 by the stress-induced activating phosphorylation of pre-formed oligomer. *J. Cell Physiol.* **191**, 95–104
- Bunkoczi, G., Salah, E., Filippakopoulos, P., Fedorov, O., Müller, S., Sobott, F., Parker, S. A., Zhang, H., Min, W., Turk, B. E., and Knapp, S. (2007) Structural and functional characterization of the human protein kinase ASK1. *Structure* **15**, 1215–1226
- Noguchi, T., Takeda, K., Matsuzawa, A., Saegusa, K., Nakano, H., Gohda, J., Inoue, J., and Ichijo, H. (2005) Recruitment of tumor necrosis factor receptor-associated factor family proteins to apoptosis signal-regulating kinase 1 signalosome is essential for oxidative stress-induced cell death. *J. Biol. Chem.* **280**, 37033–37040
- Zhang, L., Chen, J., and Fu, H. (1999) Suppression of apoptosis signal-regulating kinase 1-induced cell death by 14–3-3 proteins. *Proc. Natl. Acad. Sci. U.S.A.* **96**, 8511–8515
- Fujino, G., Noguchi, T., Matsuzawa, A., Yamauchi, S., Saitoh, M., Takeda, K., and Ichijo, H. (2007) Thioredoxin and TRAF family proteins regulate reactive oxygen species-dependent activation of ASK1 through reciprocal modulation of the N-terminal homophilic interaction of ASK1. *Mol. Cell Biol.* **27**, 8152–8163
- Liu, H., Nishitoh, H., Ichijo, H., and Kyriakis, J. M. (2000) Activation of apoptosis signal-regulating kinase 1 (ASK1) by tumor necrosis factor receptor-associated factor 2 requires prior dissociation of the ASK1 inhibitor thioredoxin. *Mol. Cell Biol.* **20**, 2198–2208
- Powis, G., and Montfort, W. R. (2001) Properties and biological activities of thioredoxins. *Annu. Rev. Biophys. Biomol. Struct.* **30**, 421–455
- Qin, J., Clore, G. M., Kennedy, W. M., Huth, J. R., and Gronenborn, A. M. (1995) Solution structure of human thioredoxin in a mixed disulfide intermediate complex with its target peptide from the transcription factor NFκB. *Structure* **3**, 289–297
- Huber, H. E., Russel, M., Model, P., and Richardson, C. C. (1986) Interaction of mutant thioredoxins of *Escherichia coli* with the gene 5 protein of phage T7: the redox capacity of thioredoxin is not required for stimulation of DNA polymerase activity. *J. Biol. Chem.* **261**, 15006–15012
- Hwang, C. Y., Ryu, Y. S., Chung, M. S., Kim, K. D., Park, S. S., Chae, S. K., Chae, H. Z., and Kwon, K. S. (2004) Thioredoxin modulates activator protein 1 (AP-1) activity and p27 Kip1 degradation through direct interaction with Jab1. *Oncogene* **23**, 8868–8875
- Holmgren, A., Söderberg, B. O., Eklund, H., and Brändén, C. I. (1975) Three-dimensional structure of *Escherichia coli* thioredoxin-S2 to 2.8-Å resolution. *Proc. Natl. Acad. Sci. U.S.A.* **72**, 2305–2309
- Zhang, R., Al-Lamki, R., Bai, L., Streb, J. W., Miano, J. M., Bradley, J., and Min, W. (2004) Thioredoxin-2 inhibits mitochondria-located ASK1-mediated apoptosis in a JNK-independent manner. *Circ. Res.* **94**, 1483–1491
- Nadeau, P. J., Charette, S. J., and Landry, J. (2009) REDOX reaction at ASK1-Cys²⁵⁰ is essential for activation of JNK and induction of apoptosis. *Mol. Biol. Cell* **20**, 3628–3637
- Liu, Y., and Min, W. (2002) Thioredoxin promotes ASK1 ubiquitination and degradation to inhibit ASK1-mediated apoptosis in a redox activity-independent manner. *Circ. Res.* **90**, 1259–1266
- Nadeau, P. J., Charette, S. J., Toledano, M. B., and Landry, J. (2007) Disul-

- fide bond-mediated multimerization of Ask1 and its reduction by thioredoxin-1 regulate H₂O₂-induced c-Jun NH₂-terminal kinase activation and apoptosis. *Mol. Biol. Cell* **18**, 3903–3913
20. Tan, S. (2001) A modular polycistronic expression system for overexpressing protein complexes in *Escherichia coli*. *Protein Expr. Purif.* **21**, 224–234
21. Hashemy, S. I., and Holmgren, A. (2008) Regulation of the catalytic activity and structure of human thioredoxin 1 via oxidation and S-nitrosylation of cysteine residues. *J. Biol. Chem.* **283**, 21890–21898
22. Rezabkova, L., Kacirova, M., Sulc, M., Herman, P., Vecer, J., Stepanek, M., Obsilova, V., and Obsil, T. (2012) Structural modulation of phosphatidylcholine by phosphorylation and 14-3-3 protein binding. *Biophys. J.* **103**, 1960–1969
23. Vecer, J., and Herman, P. (2011) Maximum entropy analysis of analytically simulated complex fluorescence decays. *J. Fluoresc.* **21**, 873–881
24. Schuck, P. (2000) Size-distribution analysis of macromolecules by sedimentation velocity ultracentrifugation and lamm equation modeling. *Biophys. J.* **78**, 1606–1619
25. Dam, J., Velikovskiy, C. A., Mariuzza, R. A., Urbanke, C., and Schuck, P. (2005) Sedimentation velocity analysis of heterogeneous protein-protein interactions: Lamm equation modeling and sedimentation coefficient distributions *c(s)*. *Biophys. J.* **89**, 619–634
26. Roessle, M. W., Klaering, R., Ristau, U., Robrahn, B., Jahn, D., Gehrmann, T., Konarev, P., Round, A., Fiedler, S., Hermes, C., and Svergun, D. (2007) Upgrade of the small-angle x-ray scattering beamline X33 at the European Molecular Biology Laboratory, Hamburg. *J. Appl. Crystallogr.* **40**, S190–S194
27. Guinier, A. (1939) La diffraction des rayons X aux très faibles angles: applications à l'étude des phénomènes ultra-microscopiques. *Ann. Phys. Paris* **12**, 161–237
28. Svergun, D. I. (1992) Determination of the regularization parameter in indirect-transform methods using perceptual criteria. *J. Appl. Crystallogr.* **25**, 495–503
29. Svergun, D. I. (1999) Restoring low resolution structure of biological macromolecules from solution scattering using simulated annealing. *Biophys. J.* **76**, 2879–2886
30. Volkov, V. V., and Svergun, D. I. (2003) Uniqueness of *ab initio* shape determination in small-angle scattering. *J. Appl. Crystallogr.* **36**, 860–864
31. Whitmore, L., and Wallace, B. A. (2004) DICHROWEB, an online server for protein secondary structure analyses from circular dichroism spectroscopic data. *Nucleic Acids Res.* **32**, W668–673
32. Zhang, Y. (2008) I-TASSER server for protein 3D structure prediction. *BMC Bioinformatics* **9**, 40
33. Kelley, L. A., and Sternberg, M. J. (2009) Protein structure prediction on the Web: a case study using the Phyre server. *Nat. Protoc.* **4**, 363–371
34. Song, Y., DiMaio, F., Wang, R. Y., Kim, D., Miles, C., Brunette, T., Thompson, J., and Baker, D. (2013) High-resolution comparative modeling with RosettaCM. *Structure* **21**, 1735–1742
35. Svergun, D., Barberato, C., and Koch, M. H. J. (1995) CRY SOL: a program to evaluate x-ray solution scattering of biological macromolecules from atomic coordinates. *J. Appl. Crystallogr.* **28**, 768–773
36. Forman-Kay, J. D., Clore, G. M., Stahl, S. J., and Gronenborn, A. M. (1992) ¹H and ¹⁵N resonance assignments and secondary structure of the human thioredoxin C62A, C69A, C73A mutant. *J. Biomol. NMR* **2**, 431–445
37. Weichsel, A., Gasdaska, J. R., Powis, G., and Montfort, W. R. (1996) Crystal structures of reduced, oxidized, and mutated human thioredoxins: evidence for a regulatory homodimer. *Structure* **4**, 735–751
38. Qin, J., Clore, G. M., and Gronenborn, A. M. (1994) The high-resolution three-dimensional solution structures of the oxidized and reduced states of human thioredoxin. *Structure* **2**, 503–522
39. Lakowicz, J. R. (1999) *Principles of Fluorescence Spectroscopy*, Second Ed., Kluwer Academic/Plenum Publishers, New York
40. Schuauerte, J. A., and Gafni, A. (1989) Long-lived tryptophan fluorescence in phosphoglycerate mutase. *Biochemistry* **28**, 3948–3954
41. Andrade, M. A., Chacón, P., Merelo, J. J., and Morán, F. (1993) Evaluation of secondary structure of proteins from UV circular dichroism spectra using an unsupervised learning neural network. *Protein Eng.* **6**, 383–390
42. Jones, D. T. (1999) Protein secondary structure prediction based on position-specific scoring matrices. *J. Mol. Biol.* **292**, 195–202
43. Kelly, S. M., and Price, N. C. (2000) The use of circular dichroism in the investigation of protein structure and function. *Curr. Protein Peptide Sci.* **1**, 349–384
44. Oblong, J. E., Berggren, M., Gasdaska, P. Y., and Powis, G. (1994) Site-directed mutagenesis of active site cysteines in human thioredoxin produces competitive inhibitors of human thioredoxin reductase and elimination of mitogenic properties of thioredoxin. *J. Biol. Chem.* **269**, 11714–11720
45. Lupas, A., Van Dyke, M., and Stock, J. (1991) Predicting coiled coils from protein sequences. *Science* **252**, 1162–1164

Cysteine residues mediate high-affinity binding of thioredoxin to ASK1

Salome Kylarova^{1,2}, Dalibor Kosek^{1,2}, Olivia Petrvalska^{1,2}, Katarina Psenakova^{1,2}, Petr Man^{3,4}, Jaroslav Vecer⁵, Petr Herman⁵, Veronika Obsilova² and Tomas Obsil^{1,2}

¹ Department of Physical and Macromolecular Chemistry, Faculty of Science, Charles University, Prague, Czech Republic

² Institute of Physiology, The Czech Academy of Sciences, Prague, Czech Republic

³ BioCeV – Institute of Microbiology, The Czech Academy of Sciences, Vestec, Czech Republic

⁴ Department of Biochemistry, Faculty of Science, Charles University, Prague, Czech Republic

⁵ Institute of Physics, Faculty of Mathematics and Physics, Charles University, Prague, Czech Republic

Keywords

ASK1; cysteine; disulfide bond; mass spectrometry; TRX

Correspondence

T. Obsil, Department of Physical and Macromolecular Chemistry, Faculty of Science, Charles University, Prague, Czech Republic

Fax: +420 224919752

Tel: +420 221951303

E-mail: obsil@natur.cuni.cz

V. Obsilova, Institute of Physiology, The Czech Academy of Sciences, Prague, Czech Republic

Fax: +420 241062488

Tel: +420 241062191

E-mail: veronika.obsilova@fgu.cas.cz

(Received 3 August 2016, accepted 1 September 2016)

doi:10.1111/febs.13893

Apoptosis signal-regulating kinase 1 (ASK1, MAP3K5) activates p38 mitogen-activated protein kinase and the c-Jun N-terminal kinase in response to proinflammatory and stress signals. In nonstress conditions, ASK1 is inhibited by association with thioredoxin (TRX) which binds to the TRX-binding domain (ASK1-TBD) at the N terminus of ASK1. TRX dissociates in response to oxidative stress allowing the ASK1 activation. However, the molecular basis for the ASK1:TRX1 complex dissociation is still not fully understood. Here, the role of cysteine residues on the interaction between TRX1 and ASK1-TBD in both reducing and oxidizing conditions was investigated. We show that from the two catalytic cysteines of TRX1 the residue C32 is responsible for the high-affinity binding of TRX1 to ASK1-TBD in reducing conditions. The disulfide bond formation between C32 and C35 within the active site of TRX1 is the main factor responsible for the TRX1 dissociation upon its oxidation as the formation of the second disulfide bond between noncatalytic cysteines C62 and C69 did not have any additional effect. ASK1-TBD contains seven conserved cysteine residues which differ in solvent accessibility with the residue C250 being the only cysteine which is both solvent exposed and essential for TRX1 binding in reducing conditions. Furthermore, our data show that the catalytic site of TRX1 interacts with ASK1-TBD region containing cysteine C200 and that the oxidative stress induces intramolecular disulfide bond formation within ASK1-TBD and affects its structure in regions directly involved and/or important for TRX1 binding.

Introduction

Apoptosis signal-regulating kinase 1 (ASK1, also known as MAP3K5), a member of the mitogen-activated protein kinase kinase kinase (MAP3K) family, activates the p38 mitogen-activated protein kinase and the c-Jun N-terminal kinase in response to proinflammatory and stress signals [1]. ASK1 is activated by

various types of stimuli, such as oxidative stress, endoplasmic reticulum stress, calcium influx, tumor necrosis factor α , and lipopolysaccharide and its activity plays a key role in the pathogenesis of several diseases including cancer, neurodegeneration, and cardiovascular diseases (reviewed by [2,3]). According to the

Abbreviations

ASK1, apoptosis signal-regulating kinase 1; ASK1-TBD, thioredoxin-binding domain of ASK1; AUC, analytical ultracentrifugation; DSF, differential scanning fluorimetry; IAA, 2-iodoacetamide; SV, sedimentation velocity; TRX, thioredoxin.

current model of ASK1 regulation in oxidative stress, ASK1 forms a silent high molecular mass complex called ASK1 signalosome in nonstress conditions by direct interaction through the C-terminal, coiled-coil domain [4]. In this complex, the ASK1 activity is inhibited by association with thioredoxin (TRX) interacting with the N-terminal region of ASK1, and the 14-3-3 protein recognizing phosphorylated motif at the C terminus of the kinase domain [5–7]. In response to oxidative stress, TRX and the 14-3-3 protein dissociate allowing the recruitment of tumor necrosis factor receptor-associated factors 2 and 6 to the N-terminal region of ASK1. This, in turn, results in homooligomerization of ASK1 through its N-terminal coiled-coil motif, autophosphorylation of activation loop at T838 and ASK1 activation [8,9].

Thioredoxins, a class of small dithiol oxidoreductases, perform various biological functions including the reduction of protein disulfide bonds, the supply of reducing equivalents to redox enzymes, and the regulation of transcription factors and proteins through either a direct reduction of their cysteine groups or different mechanisms (reviewed by [10]). The sequence of mammalian TRX1 contains five cysteine residues (Fig. 1A) from which two (C32 and C35) are embedded within the highly conserved catalytic motif W³¹CGPC³⁵, where they provide the sulfhydryl groups responsible for TRX-dependent redox activity [11]. The formation of an intramolecular disulfide bond between these two cysteine residues upon their oxidation is thought to cause the dissociation of TRX1 from signalosome resulting in the activation of ASK1 under oxidative stress conditions [5,7,8]. The three nonactive-site cysteines of TRX1 are located at positions 62, 69, and 73 and it has been suggested that these three residues are also important for the function of TRX1 [12]. In addition, residues C62 and C69 have been shown to form a second intramolecular disulfide bond under oxidizing conditions [13,14], but whether its formation plays any role in TRX1 dissociation from ASK1 is unknown.

It has recently been shown that the N-terminal TRX-binding domain of ASK1 (ASK1-TBD) is a monomeric protein which binds reduced TRX1 with 1:1 molar stoichiometry through the relatively large binding interface without undergoing any dramatic conformational change [15]. However, the molecular basis for the ASK1-TBD:TRX1 complex dissociation upon the oxidative stress is still not fully understood. For example, it is still unclear how the intramolecular disulfide bond formation within the catalytic site of TRX1 causes the complex dissociation and whether this process is the only factor responsible for

the complex dissociation under the oxidative stress. Moreover, the sequence of ASK1-TBD contains seven conserved Cys residues (Fig. 1B) and it is entirely possible that some of these residues might form intra- and/or intermolecular disulfide bond(s) under the oxidative stress, thus affecting the structure of ASK1-TBD. If this is the case then the oxidation of ASK1-TBD might be another factor that contributes to the dissociation of its complex with TRX1.

In this work, we investigated the role of cysteine residues on the interaction between TRX1 and ASK1-TBD in both reducing and oxidizing conditions. We show that from the two catalytic cysteines of TRX1 the residue C32 is responsible for the high-affinity binding of TRX1 to ASK1-TBD in reducing conditions. The disulfide bond formation between C32 and C35 within the active site of TRX1 is the main factor responsible for the TRX1 dissociation upon its oxidation as the formation of the second disulfide bond between non-catalytic C62 and C69 did not have any additional effect. We also show that cysteine residues of ASK1-TBD differ in solvent accessibility with C250 being the only cysteine which is both solvent exposed and essential for TRX1 binding in reducing conditions. Furthermore, our data show that the catalytic site of TRX1 interacts with ASK1-TBD region containing cysteine C200 and that the oxidative stress induces intramolecular disulfide bonds formation within ASK1-TBD and affects its structure in regions directly involved and/or important for TRX1 binding.

Results

Residue C32 of TRX1 is crucial for the high-affinity binding of TRX1 to ASK1-TBD in reduced conditions

Main objective of this work was to investigate the importance of individual cysteine residues for the interaction between TRX1 and ASK1-TBD. First, we focused our attention on TRX1 (Fig. 1A) and used site-directed mutagenesis to assess the role of its cysteines in the binding to ASK1-TBD. In our previous work, the sedimentation velocity analytical ultracentrifugation (SV AUC) was used to show that the TRX1 C73S mutant binds ASK1-TBD in reducing conditions with K_D value of $\sim 0.3 \mu\text{M}$ [15]. Therefore, the remaining TRX1 cysteine mutants (C32S, C35S, C62S, and C69S) were prepared and their binding to ASK1-TBD was characterized using the same approach. Mutations of these residues are known to

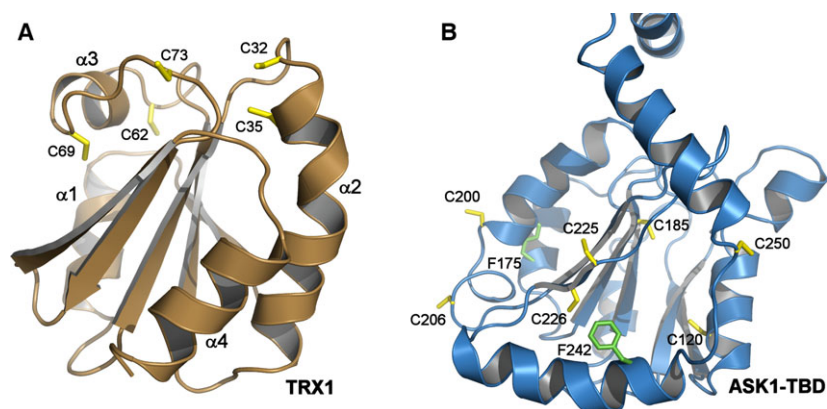


Fig. 1. Crystal structure of TRX1 and a theoretical model of ASK1-TBD. (A) Crystal structure of reduced human TRX1 [17]. Cysteine residues are shown as sticks. (B) Theoretical model of human ASK1-TBD (sequence 88-302) [15]. Cysteine residues are shown as yellow sticks. Phenylalanine residues (F175 and F242) that were replaced by tryptophans for time-resolved fluorescence experiments are shown in green.

have no significant effect on TRX1 structure [16,17]. For each TRX1 mutant, a range of different molar ratios of ASK1-TBD with reduced TRX1 were examined using SV AUC and the values of the apparent equilibrium dissociation constant (K_D) were estimated by analyzing the isotherms of weight-averaged sedimentation coefficients (s_w isotherms) as a function of TRX1 concentration (Fig. 2, panels A–E, Table 1). The normalized continuous sedimentation coefficient distributions $c(s)$ underlying the s_w data points obtained from SV experiments of mixtures of ASK1-TBD WT and TRX1 mutants are shown in insets in Fig. 2. These experiments revealed that only the TRX1 C32S mutant binds ASK1-TBD with a significantly lower binding affinity with the best-fit K_D of $12 \pm 3 \mu\text{M}$, whereas all other TRX1 mutants bind ASK1-TBD with similar affinities as TRX1 WT with the best-fit K_D values of $< 0.6 \mu\text{M}$. This strongly suggests that from the two catalytic cysteines of TRX1 the residue C32 is the one responsible for the high-affinity binding of TRX1 to ASK1-TBD under reducing conditions.

Disulfide bond formation between C32 and C35 is the main factor responsible for the ASK1-TBD: TRX1 complex dissociation upon TRX1 oxidation

Several studies suggested that the disulfide bond formation between the active-site cysteines, C32 and C35, is responsible for TRX1 dissociation from ASK1 [5,7,8]. However, the TRX1 oxidation has been shown to generate, besides this disulfide, also a second disulfide bond between the nonactive-site cysteines, C62 and C69, with a predicted effect on TRX structure as

C62 and C69 are 17 Å apart in the TRX1 molecule (Fig. 1A) [12,13,17]. To investigate the role of this second disulfide in the TRX1 dissociation from ASK1-TBD, TRX1 was oxidized using H_2O_2 for 15 min at 37 °C at two different molar ratios (protein: H_2O_2) of 1:5 (denoted here as ‘low-ox’ conditions) and 1:100 (denoted here as ‘high-ox’ conditions). Oxidation of TRX1 under high-ox conditions has been shown to induce the formation of two disulfide bonds, (C32–C35 and C62–C69) whereas oxidation under low-ox conditions produces TRX1 containing only one disulfide bond involving active-site cysteines C32 and C35 [12]. However, SV AUC experiments revealed that TRX1 WT forms dimers upon the oxidation even under low-ox conditions (Fig. 3A), likely due to the intermolecular disulfide bond formation by the nonactive-site cysteine C73 [17]. The dimerization via C73 blocks the active site due to the catalytic motif $\text{W}^{31}\text{CGPC}^{35}$ being part of the dimer interface [17] and since it is considered to be an *in vitro* artifact we decided to use TRX1 C73S mutant instead of TRX1 WT in these experiments. The quantification of free thiol groups before and after TRX1 C73S oxidation under low-ox and high-ox conditions revealed expected decrease in the number of free thiols consistent with the formation of one and two disulfides, respectively (Table 2). The analysis of the s_w isotherm determined for ASK1-TBD and TRX1 C73S oxidized under low-ox conditions revealed the best-fit K_D of $4 \pm 2 \mu\text{M}$ using a 1:1 Langmuir binding model, thus significantly lower binding affinity compared to reduced TRX1 C73S (Fig. 2F and Table 1). We have previously shown that TRX1 C73S oxidized under high-ox conditions binds to ASK1-TBD with the K_D value of

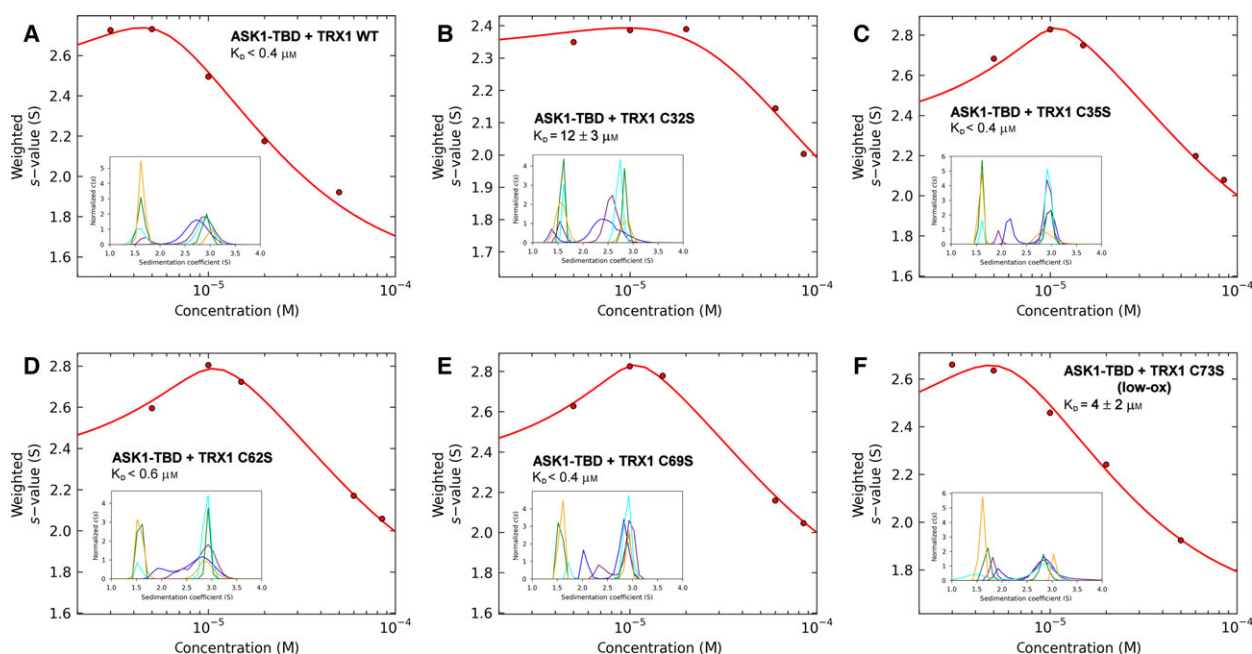


Fig. 2. Sedimentation velocity analytical ultracentrifugation analysis of complexes between TRX1 variants and ASK1-TBD. (A) Reduced TRX WT and ASK1-TBD WT. (B) Reduced TRX C32S and ASK1-TBD WT. (C) Reduced TRX C35S and ASK1-TBD WT. (D) Reduced TRX C62S and ASK1-TBD WT. (E) Reduced TRX C69S and ASK1-TBD WT. (F) Oxidized TRX C73S (low-ox conditions) and ASK1-TBD WT in buffer without reducing agents. Isotherm of weight-averaged sedimentation coefficients s_w were obtained from SV AUC experiments of mixtures of ASK1-TBD WT (5 μ M) and TRX1 (3–85 μ M). The insets show the sedimentation coefficient distributions $c(s)$ of mixtures of ASK1-TBD and TRX1 at various concentrations underlying the s_w data points (panels B–E: 5 μ M TRX1 blue, 10 μ M TRX1 purple, 20 μ M TRX1 cyan, 60 μ M TRX1 green, 85 μ M TRX1 orange; panels A and F: 3 μ M TRX1 blue, 5 μ M TRX1 purple, 10 μ M TRX1 cyan, 20 μ M TRX1 green, 50 μ M TRX1 orange).

Table 1. Binding affinities of TRX1 Cys mutants for ASK1-TBD.

TRX1 variant	K_D^a , μ M
WT reduced	< 0.4
C32S reduced	12 ± 3
C35S reduced	< 0.4
C62S reduced	< 0.6
C69S reduced	< 0.4
C73S reduced ^b	0.3 ± 0.1
C73S low-ox	4 ± 2
C73S high-ox ^b	6 ± 2

^a K_D values and their uncertainties were determined by analyzing the isotherms of weight-averaged sedimentation coefficients (s_w isotherm) as a function of TRX1 concentration using the SEDPHAT software [30,31].

^b These K_D values were reported in Kosek *et al.* [15].

6 ± 2 μ M [15]. No significant difference in binding affinities of TRX1 C73S oxidized in low-ox and high-ox conditions for ASK1-TBD suggests that the formation of the second disulfide bond between the nonactive-site cysteines C62 and C69 does not play any significant role in the dissociation of the TRX1:ASK1-TBD complex upon TRX1 oxidation.

Cysteine residues of ASK1-TBD differ in solvent accessibility

Apoptosis signal-regulating kinase 1-TBD contains seven conserved cysteine residues C120, C185, C200, C206, C225, C226, and C250 (Fig. 1B). Previous studies revealed that C250 is important for the TRX1 binding to ASK1 as its mutations (C250A, C250S) inhibited this interaction [15,18,19]. However, the role of other cysteine residues of ASK1-TBD, especially upon its oxidation, is unclear. Since the three-dimensional structure of ASK1-TBD is still unknown, we first investigated the solvent accessibility and reactivity of all cysteine residues from this domain. Here, we employed the experimental setup primarily designed for hydrogen/deuterium exchange mass spectrometry (HDX-MS) [20]. In this methodology the acidified protein sample is digested on immobilized pepsin column and directly analyzed by LC-MS/MS. LC-MS/MS analysis of peptides from ASK1-TBD treated by 2-iodoacetamide (IAA) under native conditions revealed that out of seven ASK1-TBD cysteine residues the cysteine C120 is the only one inaccessible as no modification of this residue was detected under conditions used in this experiment

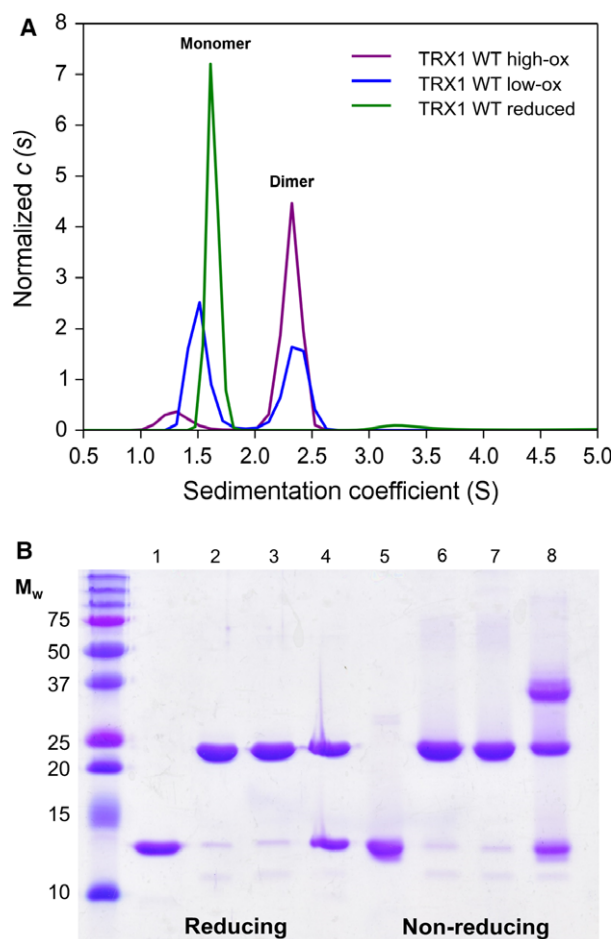


Fig. 3. Oligomerization of TRX1 and ASK1-TBD upon oxidation. (A) The normalized continuous sedimentation coefficient distributions, $c(s)$, for reduced TRX1 WT (green), TRX1 WT oxidized under high-ox (purple) and low-ox (blue) conditions. As noticed, TRX1 WT forms dimers upon oxidation with H_2O_2 . (B) 15% SDS/PAGE gel with ASK1-TBD WT and TRX1 C35,73S. Proteins (300 pmol TRX1 C35,73S and/or 300 pmol ASK1-TBD) were desalted into buffer containing 20 mM Tris-HCl (pH 7.5) and 200 mM NaCl. Then, selected samples of ASK1-TBD (samples 3 and 7) were oxidized under low-ox conditions. Nonoxidized samples were incubated at 4 °C for 24 h. All samples were then separated on SDS/PAGE under either reducing (samples 1–4) or nonreducing (samples 5–8) conditions. ASK1-TBD was oxidized by incubating with fivefold excess of H_2O_2 for 15 min at 37 °C. Oxidation reaction was stopped by adding five units of catalase. Lane 1: TRX1 C35,73S, lane 2: ASK1-TBD, lane 3: oxidized ASK1-TBD, lane 4: ASK1-TBD + TRX1 C35,73S, lane 5: TRX1 C35,73S, lane 6: ASK1-TBD, lane 7: oxidized ASK1-TBD, lane 8: ASK1-TBD + TRX1 C35,73S.

(Fig. 4A). All other cysteine residues reacted with the alkylating reagent to various extents. Residues C200, C206, and C250 were modified by IAA either completely or almost completely, (Fig. 4C, E) whereas just ~ 40% of the peptide containing residue C185 was

Table 2. The number of free thiol groups in reduced and oxidized samples of TRX1 and ASK1-TBD.

Protein	Reduced	Oxidized under low-ox conditions	Oxidized under high-ox conditions
TRX1 WT	4.9 ± 0.1	3.1 ± 0.4	0.4 ± 0.1
TRX1 C73S	3.8 ± 0.4	2.1 ± 0.4	0.1 ± 0.1
ASK1-TBD	7.1 ± 0.3	4.7 ± 0.2	n.d.

The values are shown as the mean ± SD of five experiments.

alkylated (Fig. 4B). In addition, approx. 80% of the peptide containing pair of adjacent cysteines, C225 and C226, was doubly alkylated while ~ 20% of this peptide was alkylated on just one cysteine residue (Fig. 4D). Detailed inspection of the MS/MS data, however, failed to prove whether there is any preference for modification of either of the two vicinal Cys residues. Altogether, these data suggest that the residue C185 and one from the pair C225, C226 are not fully exposed to the surface of ASK1-TBD.

Oxidation of ASK1-TBD leads to the formation of two intramolecular disulfide bonds

Next, the formation of disulfide bond(s) upon the ASK1-TBD oxidation was investigated. In these experiments, ASK1-TBD was oxidized using low-ox conditions as high-ox conditions caused heavy precipitation of the protein. The nonreducing SDS/PAGE revealed no significant formation of disulfide-linked ASK1-TBD homodimers or other multimers upon the oxidation (Fig. 3B, compare lanes 3 and 7). However, the quantification of free thiol groups before and after ASK1-TBD oxidation revealed a decrease in the number of free thiols from 7.1 ± 0.3 to 4.7 ± 0.2 , (Table 2) thus suggesting at least one intramolecular disulfide bond formation. This was further investigated by high-resolution mass spectrometry. Samples of ASK1-TBD were first analyzed directly (intact mass measurement). Details of the ultrahigh resolution ESI-FTMS spectra of intact ASK1-TBD in the presence of DTT, without DTT and after the oxidation are shown in Fig. 5A–C. The shift of the main peak toward the lower mass corresponds to the formation of 1–2 disulfide bonds upon oxidation while no such effect was observed to be induced by air oxidation (sample without DTT). In addition, virtually no Met, Trp or His oxidation was caused by H_2O_2 treatment under low-ox conditions and only the traces of sodiated and potassiated adducts were detectable. In order to obtain semi-quantitative estimation of the number of disulfide bonds formed upon oxidation, ASK1-TBD was also analyzed after oxidation followed by non-native

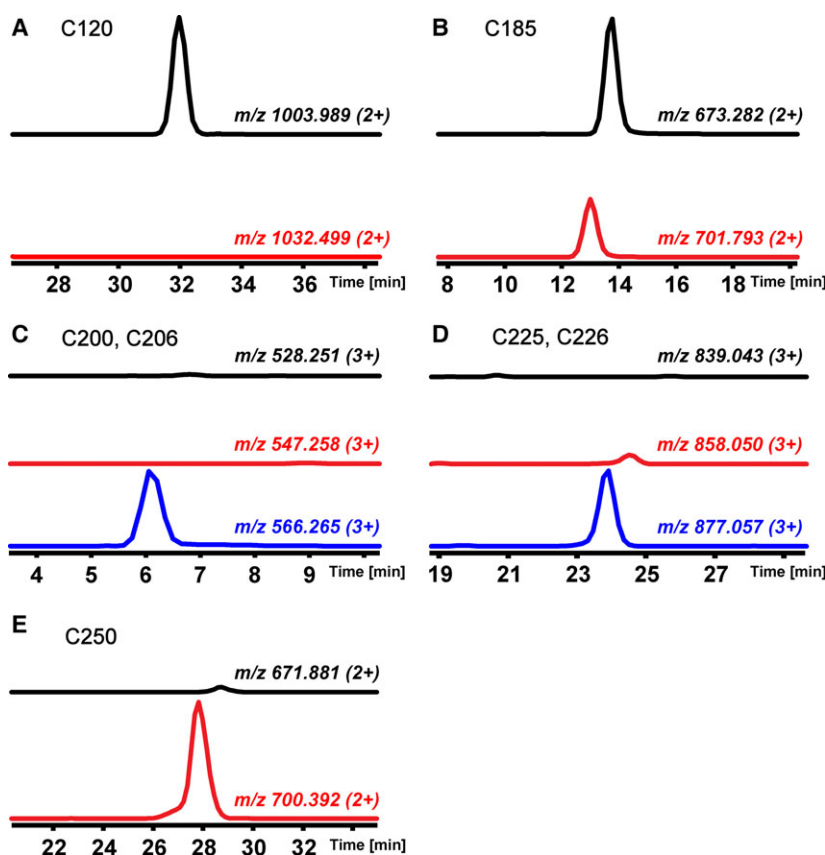


Fig. 4. Accessibility and reactivity of Cys residues in ASK1-TBD probed by alkylation with iodoacetamide. Extracted ion chromatograms for selected peptic peptides covering cysteines in the ASK1-TBD sequence are shown. Traces are colored according to the extent of modification—unmodified (black), singly (red), and doubly (blue) alkylated. The panels represent the following peptides: (A) ESEALQSLREACETVGATL (C120); (B) YCDTNSDSLQSL (C185); (C) KEICQKNTMCTGN (C200 and C206); (D) YTFVPYMITPHNKVYCCDSSF (C225 and C226); (E) ELLLGPICL (C250). Mass-to-charge (m/z) ratios used to plot the chromatograms are indicated above each trace.

alkylation (reaction carried out in the presence of denaturing agent). ASK1-TBD fully alkylated under denaturing conditions was used here as a control. Figure 5D–F shows details of the 22+ charge state of intact ASK1-TBD fully reduced (panel D), fully alkylated (panel E), and oxidized prior to the non-native alkylation (panel F). The spectrum of ASK1-TBD alkylated under denaturing conditions (Fig. 5E) shows the presence of seven to eight carbamidomethylations suggesting that besides all seven cysteine residues an additional carbamidomethylation also occurs on some other residue. The spectrum of oxidized and then alkylated ASK1-TBD (Fig. 5F) reveals the presence of two peak series. The more intense one validates the presence of ASK1-TBD containing three, five, or seven carbamidomethylations that correspond to the presence of two, one, and none disulfide bridges, respectively. The presence of proteins containing four, six, and eight carbamidomethylations (the less intense peak series in the spectrum) is due to the modification of

one noncysteine residue in the sequence of ASK1-TBD. These proteoforms, however, still correspond to the ASK1-TBD with two, one, and none disulfide bonds, respectively.

Following intact mass measurements we performed detailed analysis of the disulfide bonds pattern and of the extent to which these bonds are formed. For this, two different approaches were used, however, in both cases, ASK1-TBD after full alkylation and ASK1-TBD that underwent oxidation followed by alkylation, were digested with protease and the resulting peptides were identified by LC-MS/MS. In the first set of analyses the individual ASK1-TBD samples were digested with trypsin prior to the MS analysis. Several disulfide-linked peptides were identified leading to the assignment of the disulfide bond pattern as follows. C120 was not involved in any disulfide linkage at all. On the other hand, C200 formed disulfide with C206, while C225 was found to be bonded with C226. Interestingly weaker MS signals were also found for

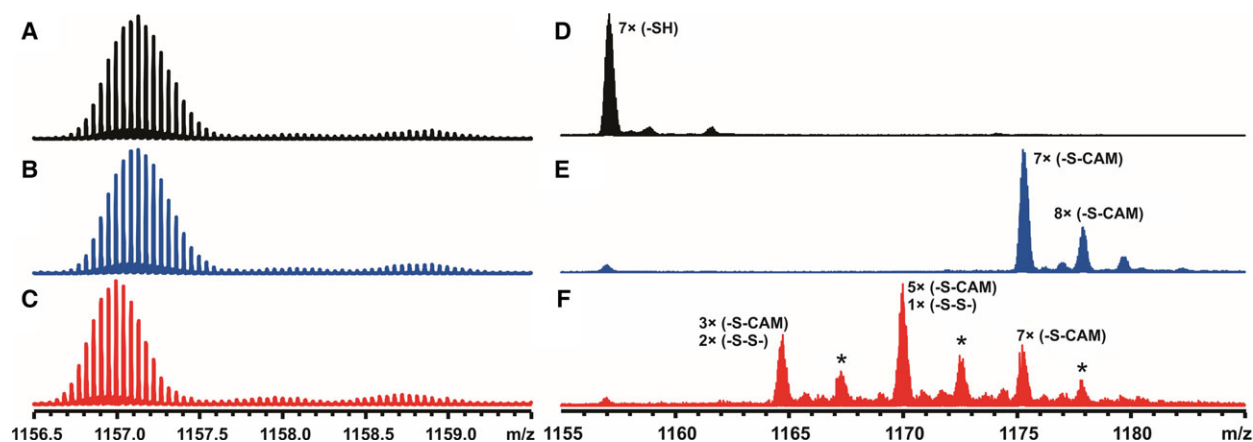


Fig. 5. Formation of disulfide bonds in ASK1-TBD monitored by high-resolution mass spectrometry. Detail of the isotopic profile of 22+ charge state of intact ASK1-TBD in the fully reduced form (A), after removal of DTT (B) and after oxidation under low-ox conditions (C). The apparent shift of the isotopic envelope toward the lower masses (panel C) corresponds to the formation of one to two disulfides. The mass region above the main peak also shows that the treatment with the peroxide caused virtually no oxidation beside the disulfide bond closing. (D–F) Monitoring of the disulfide bonds formation using alkylation and intact mass measurement. Detail of the 22+ charge state of intact ASK1-TBD for the fully reduced protein (D), protein alkylated by iodoacetamide under denaturing conditions (E) and protein alkylated under denaturing conditions after oxidation (F). Non-native alkylation (panel E) leads to full modification of all cysteine residues, however, slight overmodification on protein N terminus and/or some noncysteine residues can also be observed. Alkylation after oxidation (panel F) helps to estimate portion of the protein with no disulfide bond (7 × CAM), one disulfide (5 × CAM, 1 × -S-S-), and two disulfides (3 × -S-S-). CAM stands for carbamidomethylation, disulfide is described as ‘-S-S-’ and free sulfhydryl as ‘-SH’. Peaks labeled with an asterisk correspond to ASK1-TBD with CAM on noncysteine residue.

linkages C185–C200 and for C250 linked either to C225 or C226 (Fig. 6).

In order to obtain estimation of the extent to which these disulfide bonds were created, we employed the HDX-MS setup mentioned above. Based on this data, the assessment of protein amount injected in individual analyses was performed using noncystein peptides (Fig. 7). This showed that the amount of the analyzed protein is virtually identical for fully alkylated and oxidized and then alkylated ASK1-TBD, which is a necessary prerequisite for further comparisons. Next, the intensities of extracted ion chromatograms for selected Cys-containing peptides were plotted and compared. Based on the Fig. 7B we can conclude that the peptide bearing C185 was not changing its intensity upon oxidation and thus remained as a free sulfhydryl. On the other hand, the largest intensity decrease was observed for peptides covering C200, C206, C225, and C226, thus supporting their preferential involvement in disulfide bonds. Moreover, moderate signal drop was also observed for C185 and C250. Finally, these analyses also confirmed part of the results arising from trypsin digestion, namely formation of disulfide bonds C200–C206 and C225–C226. Altogether these data corroborated our previous findings from the native ASK1-TBD alkylation as well as from the disulfide bond assignment and from the intact mass measurements.

Disulfide bonds formation upon oxidation induces conformational change of ASK1-TBD

In our previous work, four ASK1-TBD mutants containing single tryptophan residues inserted at four different positions within the ASK1-TBD (positions 132, 175, 242, and 272) were used to study the flexibility of this domain [15]. Structural model of ASK1-TBD indicated that tryptophan residues inserted at positions 175 and 242 (using mutations F175W and F242W) might be located relatively close to cysteine residues involved in disulfide bonds formation upon oxidation (C200–C206 and C225–C226) (Fig. 1B). We therefore decided to use these two mutants to study potential structural changes induced by oxidation and disulfide bonds formation. The stability of all prepared mutants was checked using differential scanning fluorimetry (DSF). Mutants F175W and F242W did not exhibit any significant change in T_m compared to ASK1-TBD WT (Table 3). Fluorescence decay measurements revealed that the oxidation (low-ox conditions) significantly decreased the mean excited state lifetime τ_{mean} of ASK1-TBD F242W from 4.88 ± 0.02 ns, which was observed for the reduced protein, to 4.66 ± 0.05 ns obtained for the oxidized sample (Table 4). Statistical significance of the observed difference is supported by the bootstrap confidence-interval

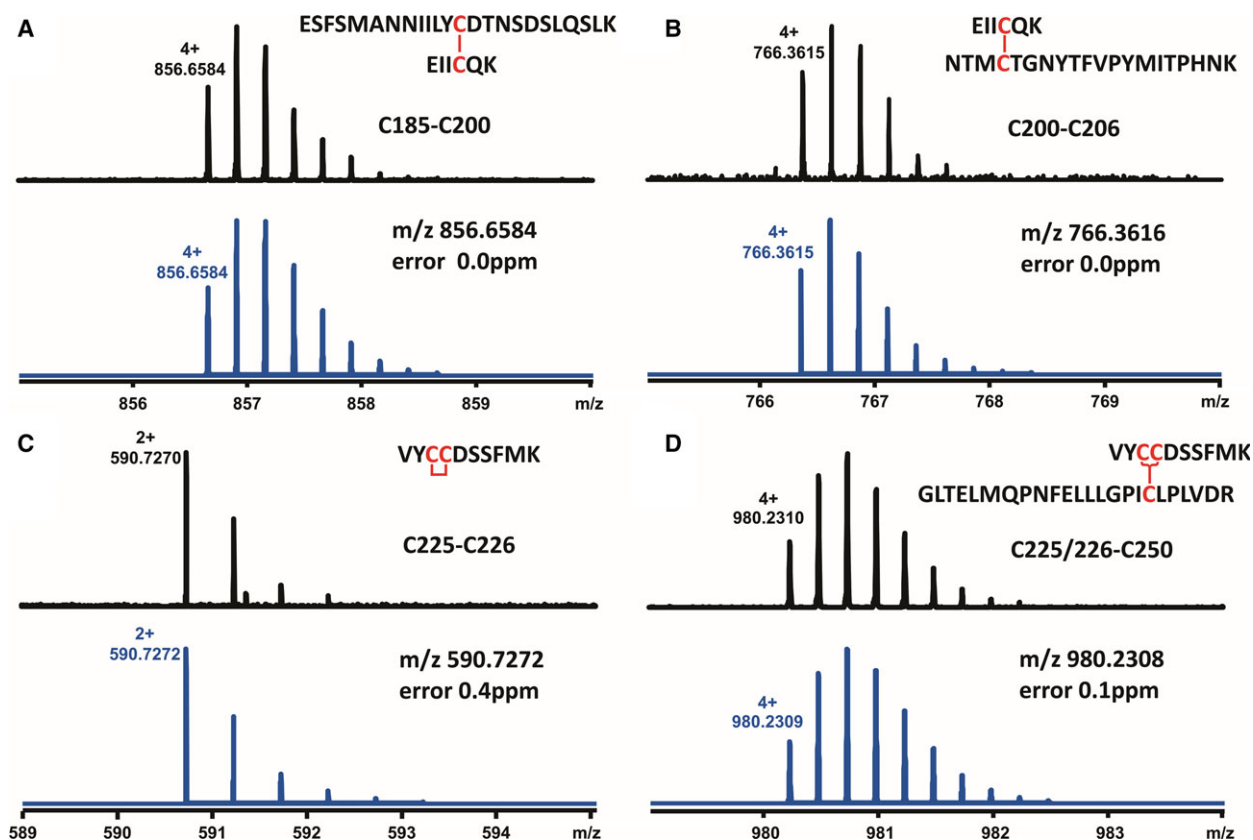


Fig. 6. Identification of disulfide bonds upon peroxide-mediated oxidation of ASK1-TBD. Detail of the isotopic pattern for each identified dipeptide is shown together with the theoretical spectrum (blue). Peptide sequences and the disulfide bond they contain are indicated in each panel together with the information about *m/z* value and the error of MS measurement.

analysis presented in Fig. 8A,B [21]. As can be noticed from the lifetime distribution analysis in Fig. 8C, the decrease in τ_{mean} is caused mainly by the oxidation-induced shortening of the three longest lifetime peaks representing together about 97% of the total fluorescence intensity. These three peaks dominate the mean excited state lifetime, since $\tau_{\text{mean}} = \sum_i (f_i \tau_i)$, where f_i represent intensity fraction of the i -th lifetime component τ_i [22]. The suppression of τ_{mean} of ASK1-TBD F242W indicates an increase in polarity and/or change in quenching interactions in the vicinity of W242 upon the oxidation and the disulfide bonds formation. On the other hand, no significant effect on τ_{mean} was found upon the oxidation of ASK1-TBD F175W (Table 4).

Analysis of the time-resolved emission anisotropy decays of reduced and oxidized samples of ASK1-TBD revealed two correlation times, one short ($\phi_1 = 0.4$ –1.2 ns) and the second close to 15 ns (ϕ_2). While the ϕ_1 likely reflects fast segmental motions, the ϕ_2 corresponds to the rotation of globular protein with M_w about 30 kDa and can be therefore

assigned to the overall rotational motion of ASK1-TBD [22]. While no change in segmental motion was observed upon the oxidation of ASK1-TBD F175W, the oxidation of ASK1-TBD F242W resulted in increased flexibility of an otherwise very rigid region containing W242, since the amplitude β_1 of almost undetectable segmental motion ($\beta_1 = 0.003$) increases upon oxidation to the value of 0.14 as documented in Table 4. Taken together, results of time-resolved tryptophan fluorescence measurements suggest that the oxidative stress induces structural change within the C terminal part of ASK1-TBD in the region containing residue 242 likely as a result of disulfide bond(s) formation.

The catalytic site of TRX1 interacts with ASK1-TBD region containing cysteine C200

Next, we attempted to measure the binding affinity of oxidized ASK1-TBD for TRX1 using the catalytically inactive TRX1 C35,73S mutant as these two mutations do not affect the complex formation (Fig. 2, Table 1).

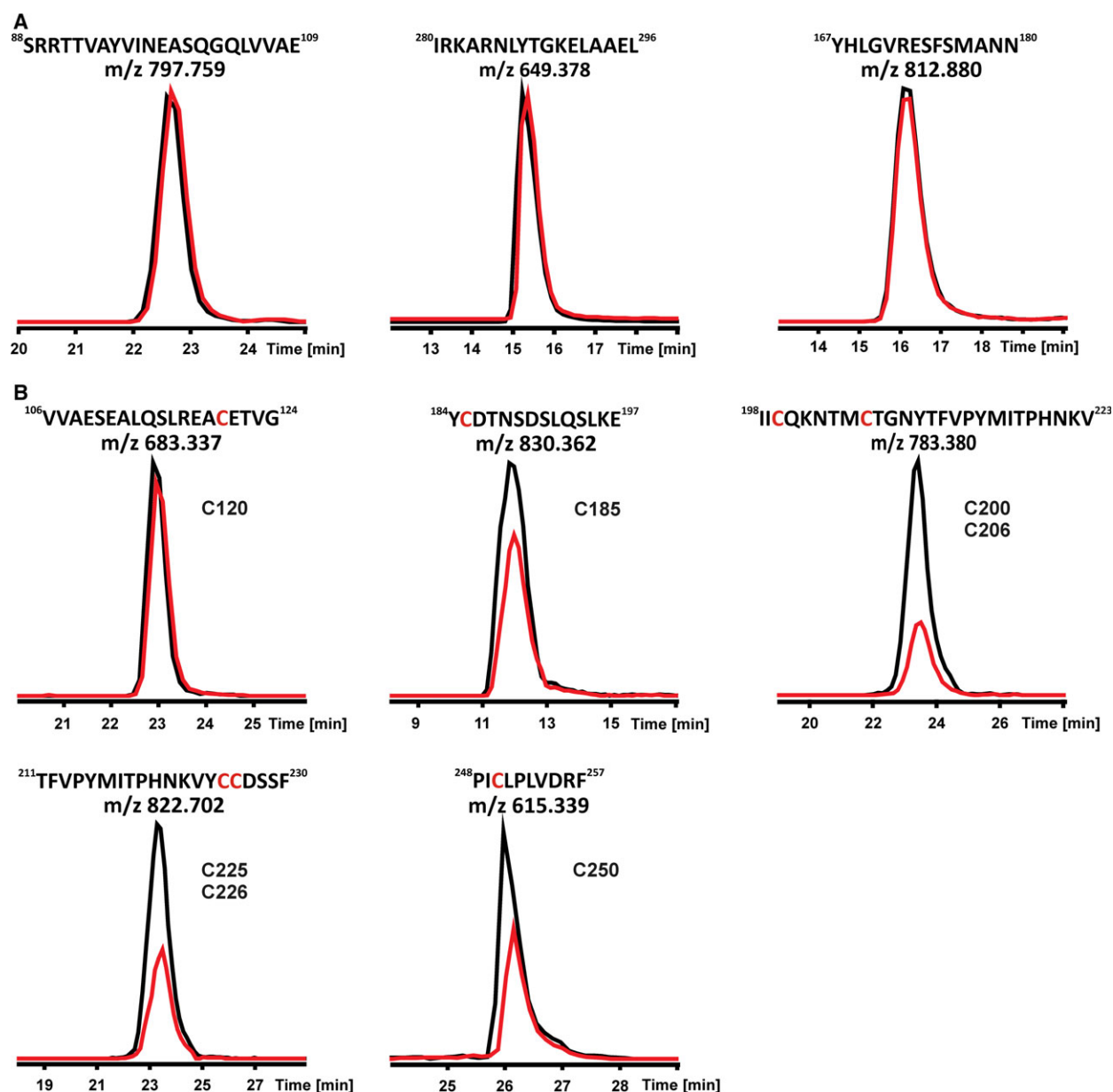


Fig. 7. Estimation of the involvement of cysteine residues in the disulfide bonds formation. Extracted ion chromatograms are compared for fully alkylated ASK1-TBD (black) and ASK1-TBD alkylated after oxidation/disulfide bond formation (red). Virtually identical loading in the analyses was verified by comparing chromatographic traces for noncysteine peptides (A). Decrease in the intensity of the chromatographic peak (B) indicates involvement of the particular Cys in disulfide bond. Sequence of the peptide with highlighted Cys residue in red, m/z value of the peptide and the number of the Cys residue on in ASK1-TBD sequence are shown in each panel.

However, and not surprisingly, the oxidized ASK1-TBD and TRX1 C35,73S in buffer without reducing agents formed the covalent adduct that prevented the binding affinity measurements. The catalytically inactive TRX1 with missing C35 is commonly used to identify proteins that interact with TRX1 as this mutation enables the formation of covalent complexes

containing mixed disulfide bond involving the N-terminal catalytic cysteine C32 [23]. ASK1-TBD and TRX1 C35,73S when incubated in buffer without reducing agents formed an adduct with molecular mass corresponding to the cross-linked ASK1-TBD:TRX1 complex (Fig. 3B, lane #8, theoretical M_w = 38.6 kDa). The LC-MS/MS analysis of this adduct revealed that

Table 3. Midpoint temperatures of the protein-unfolding transition (T_m) for ASK1-TBD mutants as determined using differential scanning fluorimetry (DSF).

ASK1-TBD variant	T_m , °C ^a
WT	49.2 ± 0.8
C120S	42.0 ± 0.1
C185S	47.3 ± 0.3
C200S	50.4 ± 0.3
C206S	49.5 ± 0.9
C225S	48.4 ± 0.1
C226S	47.9 ± 0.2
C250S	49.8 ± 0.1
F175W	49.0 ± 0.2
F242W	52.1 ± 0.1

^a Standard deviations were calculated from three different experiments.

Table 4. Summary of time-resolved tryptophan fluorescence measurements of ASK1-TBD mutants

Sample		τ_{mean}^a , ns	ϕ_1 , ns	β_1^b	ϕ_2 , ns	β_2
ASK1-TBD	Reduced	5.46 ± 0.02	1.2	0.027	15.0	0.21
F175W	Oxidized	5.44 ± 0.02	1.1	0.033	15.5	0.20
ASK1-TBD	Reduced	4.88 ± 0.02	1.2	0.003	14.5	0.23
F242W	Oxidized	4.66 ± 0.05	0.4	0.014	14.0	0.22

^a Mean lifetimes were calculated as $\tau_{\text{mean}} = \sum_i f_i \tau_i$, where f_i is an intensity fraction of the i -th lifetime component τ_i .

^b The anisotropies $r(t)$ were analyzed for a series of exponentials by a model-independent maximum entropy method without setting assumptions about the shape of the correlation time distributions [34], $r(t) = \sum_i \beta_i \exp(-t/\phi_i)$, where amplitudes β_i represent the distribution of the correlation times ϕ_i . Presented values are peak values of the multimodal distribution, amplitudes are integrated across corresponding peaks.

ASK1-TBD and TRX1 C35,73S are connected through disulfide bond connecting C32 of TRX1 and C200 of ASK1-TBD (Fig. 9). No other linkages involving other ASK1-TBD cysteine residues were detected. This strongly suggests that the catalytic site of TRX1 interacts with ASK1-TBD region containing residue C200.

Serine-scanning mutagenesis of Cys residues of ASK1-TBD

The serine-scanning mutagenesis was used to assess the importance of individual Cys residues of ASK1-TBD in TRX1 binding. To verify that the introduced mutations did not result in an overall destabilization of the ASK1-TBD structure, the stability of purified ASK1-TBD

cysteine mutants (C120S, C185S, C200S, C206S, C225S, C226S, and C250S) was checked by measuring the thermally induced protein denaturation using DSF. No significant differences in the temperature of the unfolding transition (T_m) were observed for prepared ASK1-TBD mutants with the exception of the C120S variant with the $T_m \sim 7$ °C lower compared to WT (Table 3). Significantly lower value of T_m indicates that this mutation destabilized the tertiary structure of ASK1-TBD. Moreover, modification of ASK1-TBD by iodoacetamide revealed that cysteine C120 is buried (Fig. 4A) suggesting that this residue cannot participate in TRX1 binding. Therefore, we decided to exclude the C120S mutant from further experiments. The binding of ASK1-TBD cysteine mutants (C185S, C200S, C206S, C225S, and C226S) to TRX1 WT under reducing conditions was investigated using SV AUC. The analysis of s_w isotherms revealed no significant differences in binding affinities of prepared mutants compared to ASK1-TBD WT (Tables 1 and 5, Fig. 10). This indicates that sulfhydryl groups of ASK1-TBD cysteine residues C185, C200, C206, C225, and C226S are not essential for the binding of TRX1 in reducing conditions. Thus, the only ASK1-TBD cysteine which is both solvent exposed and whose mutation significantly affects interaction with TRX1 is C250 [15,18,19]. This suggests that this residue is either directly involved in TRX binding and/or its replacement induces structural change within the TRX1-binding surface but without destabilizing the overall tertiary structure as indicated by DSF measurements (Table 3).

Discussion

Main aim of this study was to provide an insight into the role of cysteine residues in the interaction between ASK1-TBD and TRX1 which is disrupted by the oxidative stress. Previous studies suggested that the oxidation of TRX1 is the main factor responsible for the dissociation of this complex under oxidative stress conditions [5,7,8]. TRX1 oxidation leads to the formation of an intramolecular disulfide bond between the catalytic cysteines C32 and C35, and since structural studies revealed no dramatic conformational changes in TRX1 upon this disulfide bond formation [16,17], it is reasonable to speculate that one or both of these cysteine residues directly participate in TRX1 binding to ASK1-TBD. Binding experiments with TRX1 cysteine mutants revealed that only TRX1 C32S mutant failed to bind ASK1-TBD with high affinity, thus strongly suggesting that from the two catalytic cysteines the residue C32 is the prominent one required for the high-affinity binding of TRX1 to ASK1-TBD

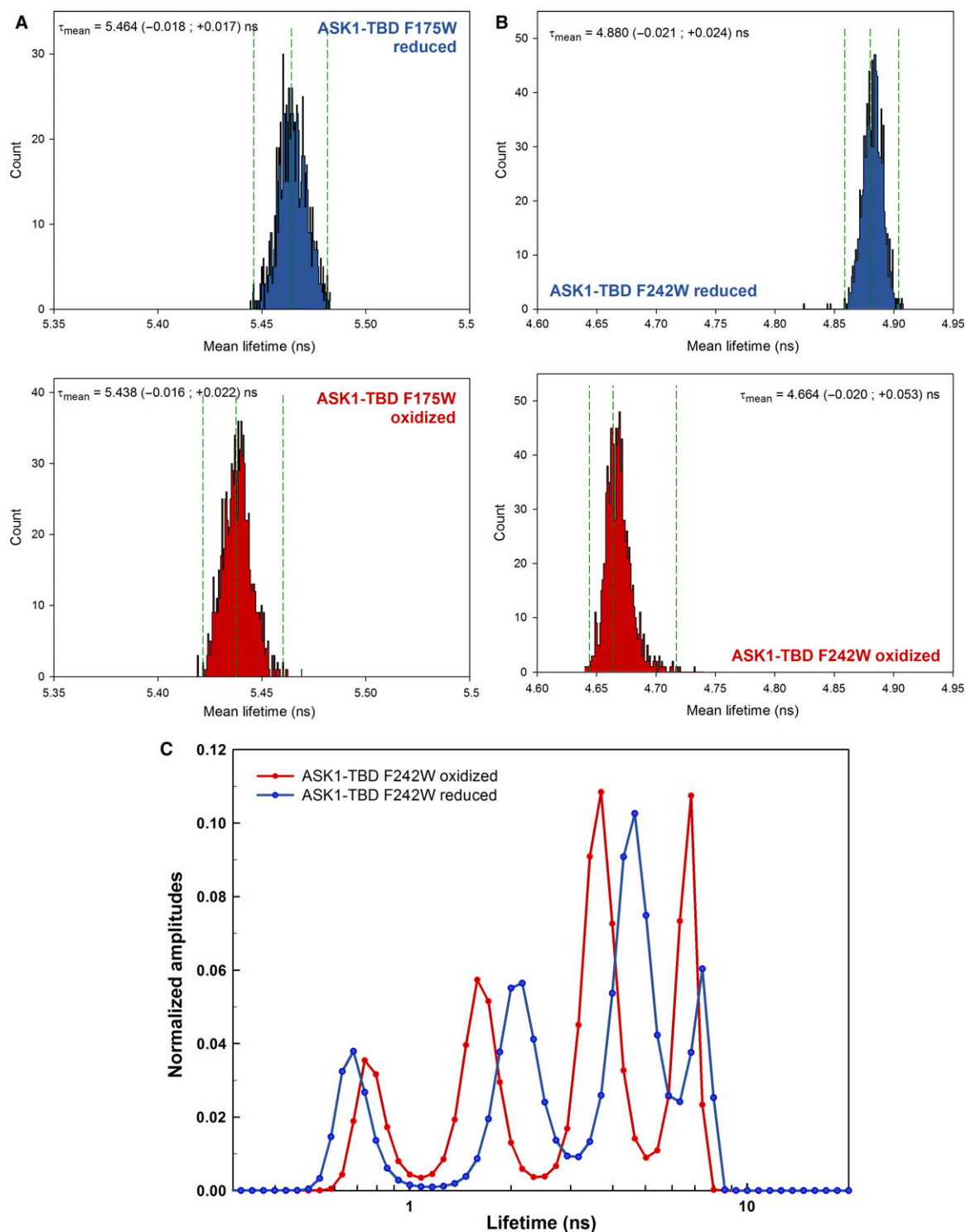


Fig. 8. Time-resolved tryptophan fluorescence measurements. Statistical confidence-interval analysis of the mean fluorescence lifetimes of ASK1-TBD F175W (A) and ASK1-TBD F242W (B) mutants in reduced and oxidized states. Histograms represent an occurrence frequency of the particular τ_{mean} as a result of 3000 bootstrap fitting cycles of raw data [21]. The distributions of ASK1-TBD F242W mutant show that the most probable τ_{mean} values are close to 4.88 and 4.66 ns with 99% confidence interval (three standard deviations) bordered by dashed lines. It is seen that confidence intervals given in Table 4 are therefore realistic estimates. (C) Excited state lifetime distributions of ASK1-TBD F242W in reduced (blue distribution) and oxidized (red distribution) states. As can be noticed, the three longest lifetime peaks dominating the mean excited state lifetime become shortened upon the ASK1-TBD oxidation. As a consequence, τ_{mean} of W242 is reduced.

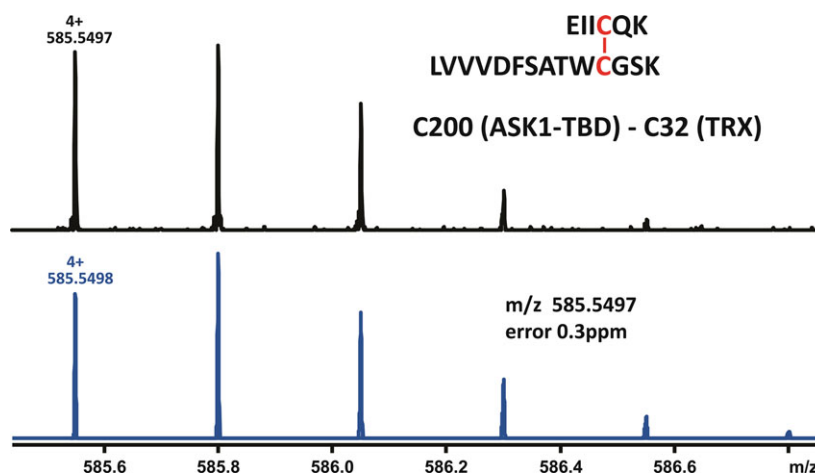


Fig. 9. Identification of the interprotein (ASK1-TBD:TRX1 C35,73S) disulfide bond. The upper spectrum shows detail of the isotopic envelope for quadruply charged ion at m/z 585.54966 corresponding to the ASK1-TBD:TRX1 C35,73S adduct peptide EIIC²⁰⁰QK–LVVVDFSATWC³²GPSK. The lower spectrum (blue) shows the theoretical spectrum which together with very low mass error of the assignment (0.3 ppm) verifies unambiguous identification of the interprotein linkage.

Table 5. Binding affinities of ASK1-TBD Cys mutants for TRX1 WT in reducing conditions.

ASK1-TBD mutant	K_D , μM^a
C185S	< 0.5
C200S	< 0.5
C206S	< 0.5
C225S	< 0.5
C226S	< 0.5
C250S ^b	50 ± 10

^a K_D values and their uncertainties were determined by analyzing the isotherms of weight-averaged sedimentation coefficients (s_w isotherm) as a function of TRX1 concentration using the SEDPHAT software [30,31].

^b This K_D value was reported in Kosek *et al.* [15] using the reduced TRX1 C73S mutant.

in reducing conditions (Table 1 and Fig. 2). Cysteine C32 is located just next to the tryptophan W31 which has also been shown to participate in TRX1 binding to ASK1-TBD, [15] thus further confirming that the catalytic W³¹CGPC³⁵ motif forms an important part of the ASK1-binding surface of TRX1. In comparison with cysteine C35, the residue C32 is located at the surface of TRX1 (Fig. 1A) and possesses a significantly lower pK_a (~6.7) [24]. Whether this is of importance for the interaction between TRX1 and ASK1-TBD is unclear but it is entirely possible that the thiolate of TRX1 cysteine C32 might be involved in either coulombic and/or sulfur–aromatic interactions with ASK1-TBD and the disulfide bond formation between C32 and C35 removes these interactions, thus destabilizing the complex.

Human TRX1 possesses three nonactive-site cysteines located at positions 62, 69, and 73, out of which C62 and C69 form an intramolecular disulfide bond under stronger oxidizing conditions and this disulfide bond formation is predicted to significantly affect TRX1 conformation by disrupting the helix α_3 of TRX1 (Fig. 1A) [13,14]. Therefore, we next investigated whether this disulfide bond formation has any additional effect on binding affinity between oxidized TRX1 and ASK1-TBD. However, our binding affinity experiments revealed that TRX1 containing just one intramolecular disulfide bond between the catalytic cysteine residues (C73S mutant oxidized under low-ox conditions) binds to ASK1-TBD with the similar affinity as TRX1 containing two disulfide bonds (C73S mutant oxidized under high-ox conditions [15]) (Fig. 2F and Table 1). This suggests that (a) the intramolecular disulfide bond formation between C32 and C35 is the main factor responsible for the complex dissociation upon the oxidation of TRX1, and that (b) the region containing cysteines C62 and C69 (the helix α_3 , Fig. 1A) is not a part of the ASK1-TBD-binding surface of TRX1.

It has previously been suggested that the oxidation of ASK1 might also participate in the activation of ASK1 kinase function [19,25]. ASK1-TBD possesses seven conserved Cys residues, (Fig. 1B) thus it is reasonable to speculate that some of these residues might form intra- or intermolecular disulfide bond(s) under oxidative stress conditions. Since the structure of ASK1-TBD is still unknown, we first investigated the solvent accessibility of these residues. Since we

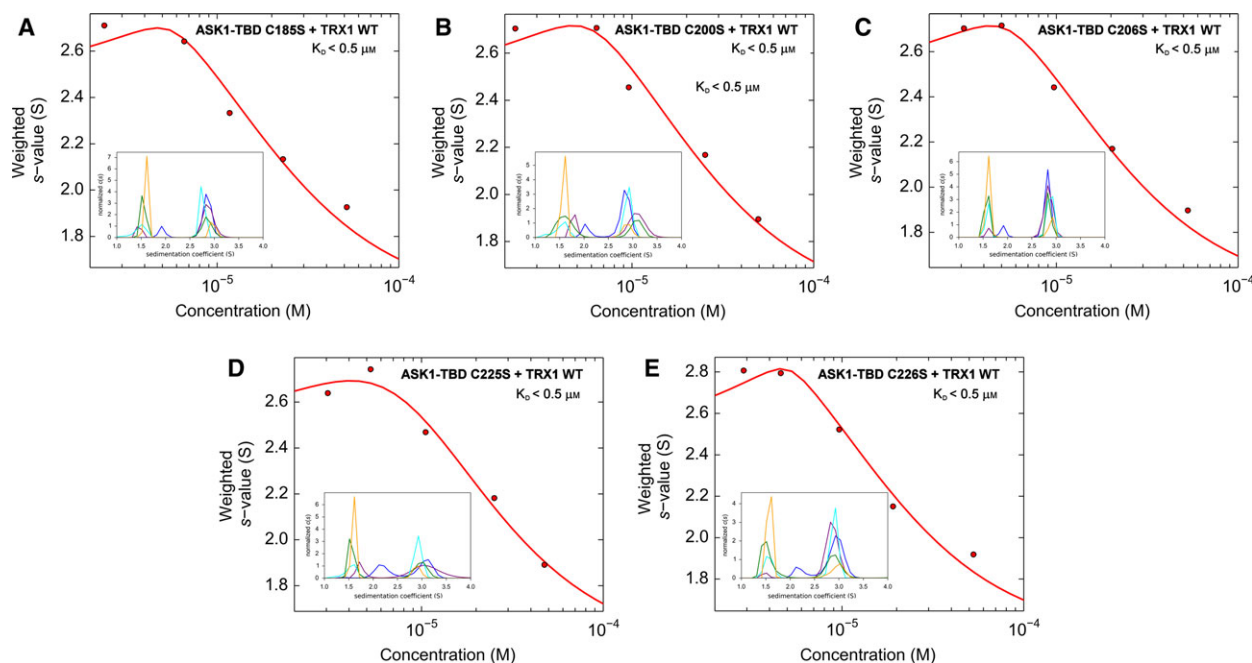


Fig. 10. Sedimentation velocity analytical ultracentrifugation analysis of complexes between reduced TRX1 WT and ASK1-TBD variants: ASK1-TBD C185S (A), ASK1-TBD C200S (B), ASK1-TBD C206S (C), ASK1-TBD C225S (D), and ASK1-TBD C226S (E). Isotherms of weight-averaged sedimentation coefficients s_w were obtained from SV AUC experiments of mixtures of ASK1-TBD (5 μ M) and TRX1 WT (3–50 μ M). The insets show the sedimentation coefficient distributions $c(s)$ of mixtures of ASK1-TBD and TRX1 at various concentrations underlying the s_w data points (3 μ M TRX1 blue, 5 μ M TRX1 purple, 10 μ M TRX1 cyan, 20 μ M TRX1 green, 50 μ M TRX1 orange).

expected sample with only partially blocked Cys residues and under classical proteomic digestion protocol (pH neutral to slightly basic) spontaneous disulfide bond formation can be a problem, we employed an alternative setup based on HDX-MS protocol. The advantages of this methodology include immediate sample processing at low pH and low temperature during the analysis. Under such conditions artificial disulfide bond scrambling can be ruled out. In addition, pepsin digestion using immobilized pepsin column provides a set of overlapping peptides and when properly tuned, full sequence coverage can be easily reached. Alkylation experiments revealed that residues C200, C206, and C250 are fully exposed to the solvent, whereas residue C120 is completely buried and residues C185 and one from the pair C225, C226 are just partially exposed to the solvent (Fig. 4). These differences are consistent with the previously published theoretical model of ASK1-TBD [15] which predicted that residues C120 and C185 are buried within the compact N-terminal part with the 3-layer α/β sandwich architecture, whereas residues C200, C206, C225, C226, and C250 are located at the periphery of ASK1-TBD (Fig. 1B). This theoretical model also indicated that residues C200 and C206, besides adjacent residues

C225 and C226, are located close enough to each other to form a disulfide bond. Indeed, the analysis of ASK1-TBD oxidized under low-ox conditions suggested intramolecular disulfide bond formation C200–C206 and C225–C226 and to a small extent also C185–C200 and C225/C226–C250 (Figs 6 and 7). However, the functional impact of these changes is still unclear. We made an attempt to assess the binding affinity of oxidized ASK1-TBD for TRX1 using the catalytically inactive TRX1 C35,73S. However, the covalent adduct formation between these two proteins in the absence of reducing agents prevented the binding affinity measurement (Fig. 3B). Further analysis of this covalent adduct suggested that the catalytic site of TRX1 (residue C32) interacts with the ASK1-TBD region containing residue C200 (Fig. 9) which belongs to cysteines involved in intramolecular disulfide bonds formation (Fig. 6). Out of the residues forming disulfide bonds, only C250 is essential for the high-affinity binding of TRX1 to ASK1-TBD (Table 5). In addition, time-resolved fluorescence measurements with the tryptophan residue inserted at position 242 revealed that the oxidation of ASK1-TBD induces a significant conformational change in this region likely as a result of disulfide bonds formation (Table 4 and Fig. 8).

Thus, we can conclude that the disulfide bonds formation affects ASK1-TBD regions involved in and/or important for the TRX1 binding.

These findings allowed us to update the theoretical model of the ASK1-TBD:TRX1 complex [15]. The model was prepared using a rigid-body docking search with the theoretical model of ASK1-TBD alone [15] and the crystal structure of reduced TRX1 [17] used as a receptor and a ligand, respectively. The best scoring complex in which the TRX1 residue C32 was located close to the residue C200 of ASK1-TBD was further refined using the ALLOSMOD-FOXS program [26,27] to generate model consistent with the previously reported small angle X-ray scattering (SAXS) data of the ASK1-TBD:TRX1 complex [15]. The best scoring AllosMod model (Fig. 11A) is consistent with the SAXS data ($\chi = 0.78$, Fig. 11B) and predicts that the TRX1-binding site is located within the C-terminal half of ASK1-TBD containing cysteines C200, C206, C225, C226, and C250. The predicted ASK1-TBD-binding surface of TRX1 includes the active site with residues W31 and C32, the N-terminal part of helix α_2 , the loop between helix α_3 and strand β_3 , and the C-terminal strand β_4 and helix α_4 . The predicted TRX1-binding surface of ASK1-TBD also includes residue F242 which was replaced by tryptophan in mutant used for time-resolved fluorescence measurements, (Table 4 and Fig. 8) thus indicating that the observed oxidation-induced conformational change affects the TRX1-binding surface of ASK1-TBD.

Taken together, our results show that the residue C32 of reduced TRX1 is responsible for its high-affinity binding to ASK1-TBD. The disulfide bond formation between C32 and C35 is the main factor responsible for the complex dissociation upon the oxidation of TRX1. Cysteine residues of ASK1-TBD differ in solvent accessibility with C250 being the only cysteine which is both solvent exposed and essential for TRX1 binding in reducing conditions. Furthermore, our data show that the catalytic site of TRX1 interacts with ASK1-TBD region containing cysteine C200 and that the oxidative stress could induce intramolecular disulfide bonds formation within ASK1-TBD and affect its structure in regions directly involved and/or important for the TRX1 binding.

Materials and Methods

Preparation of ASK1-TBD and TRX1

Human ASK1-TBD (sequence 88–302) and human TRX1 were expressed and purified as described previously [15]. All mutants of ASK1-TBD and TRX1 were generated by

using the QuikChange site-directed mutagenesis kit (Stratagene, La Jolla, CA, USA) and mutations were confirmed by sequencing.

Oxidation of ASK1-TBD and TRX1

Fully reduced ASK1-TBD, TRX1 WT, and TRX1 C73S (the complete reduction was confirmed by measuring the number of free thiol groups) were desalted on a Zeba™ Spin Desalting Column (Thermo Scientific, Prague, Czech Republic) equilibrated with 20 mM Tris-HCl (pH 7.5) and 200 mM NaCl. Proteins (15–20 μ M) were oxidized by incubating with either 5-fold (low-ox conditions) or 100-fold (high-ox conditions) excess of H_2O_2 for 15 min at 37 °C [12]. Oxidation reaction was stopped by adding five units of catalase (Sigma Aldrich, Prague, Czech Republic).

Determination of total thiol groups

Protein free thiol quantitation Ellman's reagent (5,5'-Dithio-bis-[2-nitrobenzoic acid];DTNB) assay was used to quantitate free cysteine residues [28]. Reduced or oxidized proteins (15–20 μ M) in 20 mM Tris-HCl (pH 7.5) and 200 mM NaCl were incubated in the dark with 6 M guanidine hydrochloride and 1 mM DTNB (Sigma Aldrich) in a final volume of 350 μ L of 200 mM Tris-HCl (pH 8.0). A molar extinction coefficient of TNB^{2-} anion of 13 600 $M^{-1} cm^{-1}$ at 412 nm was used to calculate the number of free thiol groups.

Native alkylation of ASK1-TBD cysteine residues by iodoacetamide

Reduced ASK1-TBD (15–20 μ M) in buffer containing 20 mM Tris-HCl (pH 7.5), 200 mM NaCl, and 5 mM DTT was mixed with 500 mM iodoacetamide stock solution in 20 mM Tris-HCl (pH 7.5) and 200 mM NaCl to yield a 5:1 molar ratio of iodoacetamide to DTT. The mixture was incubated in the dark for 30–60 min at room temperature and results of the alkylation reaction were analyzed by MS.

Mass spectrometry analysis of ASK1-TBD

Mass spectrometry techniques were used to analyze ASK1-TBD reduced, oxidized, alkylated under native-like conditions (preceding paragraph) or after non-native alkylation. This modification was done in 8 M urea and both reduced and oxidized ASK1-TBD were used for this modification. The proteins for intact mass measurement 15T FT-ICR mass spectrometer (Solarix XR, Bruker Daltonics, Billerica, MA, USA) were desalted using offline protein microtrap (Optimize Technologies, Oregon City, OR, USA) prior to the analysis. For the detailed analysis of disulfide bond linkages two sample preparation methods were used. First one employed LC system primarily designed for H/D

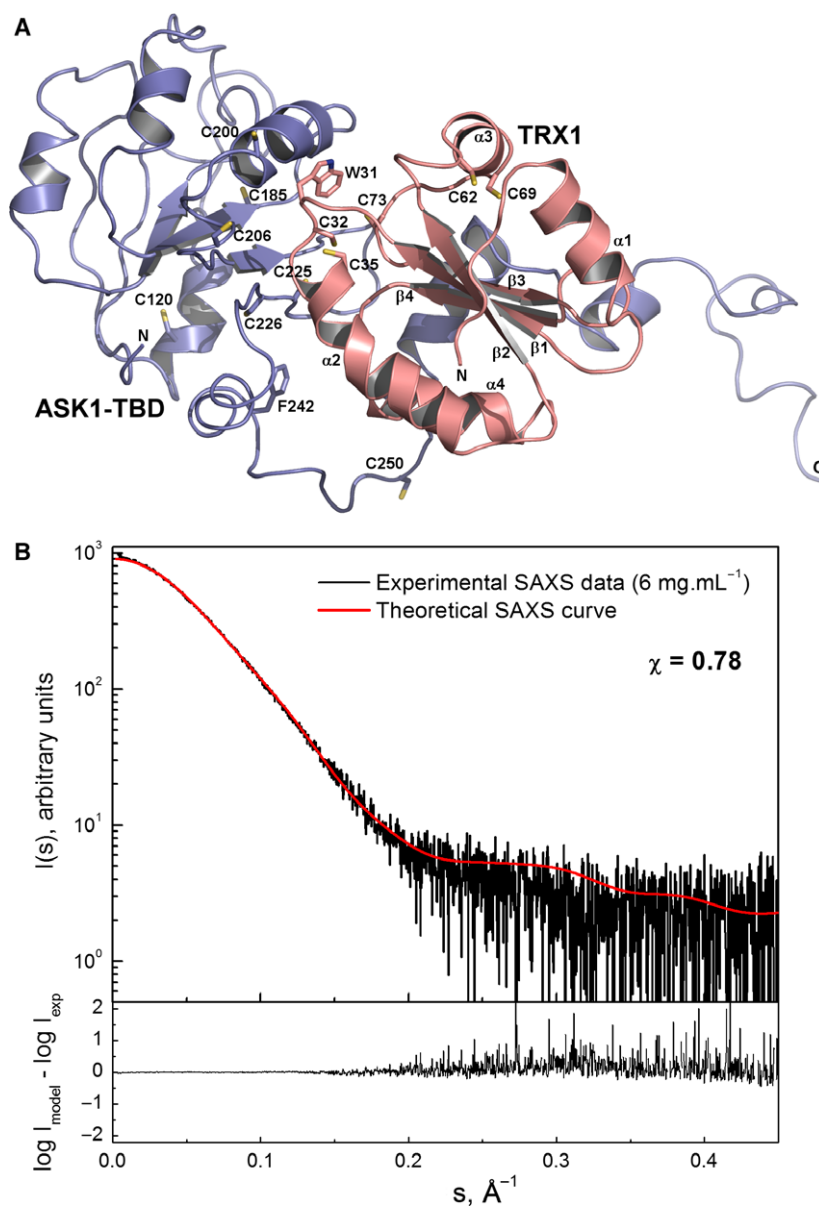


Fig. 11. Structural model of the ASK1-TBD:TRX1 complex. (A) The best scoring AllosMod model of the ASK1-TBD:TRX1 complex. The starting model of the complex for the AllosMod-FoXS simulation was obtained using the FRODOCK program [32]. AllosMod-FoXS [26,27] calculation was used to generate structure consistent with the previously reported SAXS data of the ASK1-TBD:TRX1 complex [15]. (B) Comparison of the calculated scattering curve of the best scoring AllosMod model of the ASK1-TBD:TRX1 complex (red line) with the previously reported scattering data of the complex at protein concentration 6 mg·mL⁻¹ [15]. Theoretical scattering curve of the model was calculated using the FOXS program [33].

exchange [20]. Briefly the protein was acidified, mixed with guanidine hydrochloride (final concentration 3 M) and injected onto an immobilized pepsin column where it was digested. The resulting peptides were trapped on a reversed phase trap column (peptide MicroTrap, Optimize Technologies), desalted and after that separated on an analytical reversed phase column (Zorbax 300SB-C18 5 µm, 0.5 × 35 mm, Agilent Technologies, Santa Clara, CA, USA) by acetonitrile gradient from 10 to 25% in 8 min (0.4% formic acid was used as an ion pairing agent). Outlet of the column was connected to an ESI source of 15T FT-ICR mass spectrometer (Solarix XR, Bruker Daltonics) operating in data-dependent MS/MS mode. The data were searched by MASCOT algorithm against a single-protein

database containing ASK1-TBD sequence. Based on the sample origin, some or all of the following modifications were considered as possible—formation of SS bonds, Cys carbamidomethylation, and methionine oxidation.

Alternatively, the ASK1-TBD was digested with trypsin (37 °C, 6 h). Peptide mixtures were loaded into vials and subjected to LC-MS/MS analysis. After quick online desalting the peptides were separated by an acetonitrile gradient (5–40% acetonitrile in 40 min, 0.2% formic acid was used as the ion pairing agent). The analytical column used for these analyses was Zorbax 300SB-C18 3.5 µm, 0.3 × 150 mm (Agilent Technologies). The data-dependent MS/MS data searching using MASCOT were done as described above. In addition, disulfide-linked peptides were

identified by Links algorithm based on the AUTOMATED SPECTRUM ASSIGNMENT Program [29]. Other data processing was done in DATAANALYSIS 4.4 (Bruker Daltonics).

Mass spectrometry analysis of the ASK1-TBD:TRX1 C35,73S adduct

The band corresponding to the ASK1-TBD:TRX1 C35,73S adduct was excised from the gel, destained, and modified with IAA. Trypsin digestion was carried out overnight at 37 °C. Peptide mixture was loaded into a vial and analyzed as described above for the trypsin digest of ASK1-TBD.

Analytical ultracentrifugation

Sedimentation velocity (SV) experiments were performed using a ProteomeLab™ XL-I analytical ultracentrifuge (Beckman Coulter, Brea, CA, USA). Samples were dialyzed against the buffer containing 20 mM Tris-HCl (pH 7.5), 200 mM NaCl and 5 mM 2-mercaptoethanol before analysis. Samples containing oxidized proteins were analyzed in the same buffer but without reducing agents. The buffer density, viscosity, and partial specific volume of all proteins were estimated using the program SEDNTERP (<http://sednterp.unh.edu/>). SV AUC experiments with ASK1-TBD, TRX WT, and their mutants were conducted at various loading concentrations and molar ratios in charcoal-filled Epon centerpieces with 12-mm optical path length at 20 °C and 185 462 g rotor speed (An-50 Ti rotor, Beckman Coulter). All sedimentation profiles were collected with interference and absorbance optics at 280 nm. The sedimentation coefficients $c(s)$ distributions were calculated from the raw interference data using SEDFIT software package. The procedure was followed by integration of calculated distributions to establish the weight-average s -values (s_w). Calculated s_w values were plotted as a function of TRX1 concentration to construct s_w isotherms. Obtained isotherms were fitted with $A + B \rightleftharpoons AB$ model as implemented in the SEDPHAT software package with previously known s values of each component. Resulting parameters were verified and loading concentrations were corrected using global Lamm equation modeling also implemented in the SEDPHAT software [30,31].

Differential scanning fluorimetry

The thermal shift assay was performed using a real-time PCR LightCycler 480 II (Roche Applied Science, Penzberg, Germany). The proteins at a concentration of $0.5 \text{ mg}\cdot\text{mL}^{-1}$ were incubated with $8\times$ concentrated Sypro Orange (Sigma-Aldrich) in a total reaction volume of 25 μL in the LightCycler 480 Multiwell Plate 96 (Roche Applied Science). The plate was covered with the LightCycler 480 Sealing Foil (Roche Applied Science). Temperature gradient ranged from 20 to 95 °C with a rate of $0.01 \text{ }^\circ\text{C}\cdot\text{s}^{-1}$ and fluorescence excitation and emission wavelength were 465

and 580 nm, respectively. The melting temperature values, T_m , corresponding to the minima of the negative first derivative of melting curves, were determined using the ROCHE LIGHTCYCLER 480 SW 1.5 software.

Time-resolved fluorescence measurements

Time-resolved tryptophan fluorescence intensity and anisotropy decay measurements as well as data analysis were performed as has been described previously [15]. Tryptophan emission was excited at 298 nm by a tripled output of the Ti:Sapphire laser. Tryptophan fluorescence was isolated at 355 nm by a combination of monochromator and a stack of UG1 and BG40 glass filters (Thorlabs, Newton, NJ, USA) placed in front of the input slit. All samples were blank-corrected and intensity decays were measured under the 'magic angle' conditions to remove rotational bias of the protein [22]. ASK1-TBD samples (15 μM) were placed in a thermostatic holder, and all experiments were performed at 23 °C in buffer containing 20 mM Tris-HCl (pH 7.5), 200 mM NaCl, and 1 mM EDTA. Samples measured under reduced conditions also contained 5 mM DTT.

Structural modeling of the ASK1-TBD:TRX1 complex

A rigid-body protein–protein docking search was performed using the FRODOCK program [32]. The theoretical model of ASK1-TBD [15] and the crystal structure of reduced TRX1 [17] were used as a receptor and a ligand, respectively. The AllosMod-FoXS server [26,27] was used to generate structure consistent with the previously reported SAXS data of the ASK1-TBD:TRX1 complex (at a protein concentration of $6 \text{ mg}\cdot\text{mL}^{-1}$) [15]. Theoretical scattering curve of the model was calculated using FoXS [33].

Acknowledgements

This work was supported by the Czech Science Foundation (Project 14-10061S), the Grant Agency of Charles University (Project 161116), and the Czech Academy of Sciences (Research Project RVO: 67985823 of the Institute of Physiology). Access to the MS facility was enabled through the following financial sources—EU project CZ.1.05/1.1.00/02.0109 and by the Czech Infrastructure for Integrative Structural Biology (LM2015043).

Author contributions

SK, DK, OP, and KP conducted most of the experiments and analyzed the results. PM performed LC-MS experiments, data analysis, and interpretation. PH and JV performed time-resolved fluorescence experiments,

data analysis, and interpretation. VO and TO conceived the idea for the project, analyzed the results, and wrote the manuscript.

Conflict of interest

The authors declare that they have no conflicts of interest with the contents of this article.

References

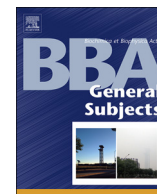
- Ichijo H, Nishida E, Irie K, ten Dijke P, Saitoh M, Moriguchi T, Takagi M, Matsumoto K, Miyazono K & Gotoh Y (1997) Induction of apoptosis by ASK1, a mammalian MAPKKK that activates SAPK/JNK and p38 signaling pathways. *Science* **275**, 90–94.
- Shiizaki S, Naguro I & Ichijo H (2013) Activation mechanisms of ASK1 in response to various stresses and its significance in intracellular signaling. *Advan Biol Regul* **53**, 135–144.
- Kawarazaki Y, Ichijo H & Naguro I (2014) Apoptosis signal-regulating kinase 1 as a therapeutic target. *Expert Opin Ther Targets* **18**, 1–14.
- Tobiume K, Saitoh M & Ichijo H (2002) Activation of apoptosis signal-regulating kinase 1 by the stress-induced activating phosphorylation of pre-formed oligomer. *J Cell Physiol* **191**, 95–104.
- Saitoh M, Nishitoh H, Fujii M, Takeda K, Tobiume K, Sawada Y, Kawabata M, Miyazono K & Ichijo H (1998) Mammalian thioredoxin is a direct inhibitor of apoptosis signal-regulating kinase (ASK) 1. *EMBO J* **17**, 2596–2606.
- Zhang L, Chen J & Fu H (1999) Suppression of apoptosis signal-regulating kinase 1-induced cell death by 14-3-3 proteins. *Proc Natl Acad Sci USA* **96**, 8511–8515.
- Liu Y & Min W (2002) Thioredoxin promotes ASK1 ubiquitination and degradation to inhibit ASK1-mediated apoptosis in a redox activity-independent manner. *Circ Res* **90**, 1259–1266.
- Fujino G, Noguchi T, Matsuzawa A, Yamauchi S, Saitoh M, Takeda K & Ichijo H (2007) Thioredoxin and TRAF family proteins regulate reactive oxygen species-dependent activation of ASK1 through reciprocal modulation of the N-terminal homophilic interaction of ASK1. *Mol Cell Biol* **27**, 8152–8163.
- Liu H, Nishitoh H, Ichijo H & Kyriakis JM (2000) Activation of apoptosis signal-regulating kinase 1 (ASK1) by tumor necrosis factor receptor-associated factor 2 requires prior dissociation of the ASK1 inhibitor thioredoxin. *Mol Cell Biol* **20**, 2198–2208.
- Hanschmann EM, Godoy JR, Berndt C, Hudemann C & Lillig CH (2013) Thioredoxins, glutaredoxins, and peroxiredoxins—molecular mechanisms and health significance: from cofactors to antioxidants to redox signaling. *Antioxid Redox Signal* **19**, 1539–1605.
- Holmgren A, Soderberg BO, Eklund H & Branden CI (1975) Three-dimensional structure of *Escherichia coli* thioredoxin-S2 to 2.8 Å resolution. *Proc Natl Acad Sci USA* **72**, 2305–2309.
- Hashemy SI & Holmgren A (2008) Regulation of the catalytic activity and structure of human thioredoxin 1 via oxidation and S-nitrosylation of cysteine residues. *J Biol Chem* **283**, 21890–21898.
- Watson WH, Pohl J, Montfort WR, Stuchlik O, Reed MS, Powis G & Jones DP (2003) Redox potential of human thioredoxin 1 and identification of a second dithiol/disulfide motif. *J Biol Chem* **278**, 33408–33415.
- Cheng Z, Zhang J, Ballou DP & Williams CH Jr (2011) Reactivity of thioredoxin as a protein thiol-disulfide oxidoreductase. *Chem Rev* **111**, 5768–5783.
- Kosek D, Kylarova S, Psenakova K, Rezabkova L, Herman P, Vecer J, Obsilova V & Obsil T (2014) Biophysical and structural characterization of the thioredoxin-binding domain of protein kinase ASK1 and its interaction with reduced thioredoxin. *J Biol Chem* **289**, 24463–24474.
- Qin J, Clore GM & Gronenborn AM (1994) The high-resolution three-dimensional solution structures of the oxidized and reduced states of human thioredoxin. *Structure* **2**, 503–522.
- Weichsel A, Gasdaska JR, Powis G & Montfort WR (1996) Crystal structures of reduced, oxidized, and mutated human thioredoxins: evidence for a regulatory homodimer. *Structure* **4**, 735–751.
- Zhang R, Al-Lamki R, Bai L, Streb JW, Miano JM, Bradley J & Min W (2004) Thioredoxin-2 inhibits mitochondria-located ASK1-mediated apoptosis in a JNK-independent manner. *Circ Res* **94**, 1483–1491.
- Nadeau PJ, Charette SJ & Landry J (2009) REDOX reaction at ASK1-Cys250 is essential for activation of JNK and induction of apoptosis. *Mol Biol Cell* **20**, 3628–3637.
- Kadek A, Mrazek H, Halada P, Rey M, Schriemer DC & Man P (2014) Aspartic protease nepenthesin-1 as a tool for digestion in hydrogen/deuterium exchange mass spectrometry. *Anal Chem* **86**, 4287–4294.
- Johnson ML (2008) Nonlinear least-squares fitting methods. *Methods Cell Biol* **84**, 781–805.
- Lakowicz JR (1999) Principles of Fluorescence Spectroscopy, 2nd edn. Kluwer Academic/Plenum Publishers, New York.
- Balmer Y, Vensel WH, Tanaka CK, Hurkman WJ, Gelhaye E, Rouhier N, Jacquot JP, Manieri W, Schurmann P, Droux M *et al.* (2004) Thioredoxin links redox to the regulation of fundamental processes of plant mitochondria. *Proc Natl Acad Sci USA* **101**, 2642–2647.

- 24 Kallis GB & Holmgren A (1980) Differential reactivity of the functional sulfhydryl groups of cysteine-32 and cysteine-35 present in the reduced form of thioredoxin from *Escherichia coli*. *J Biol Chem* **255**, 10261–10265.
- 25 Nadeau PJ, Charette SJ, Toledano MB & Landry J (2007) Disulfide Bond-mediated multimerization of Ask1 and its reduction by thioredoxin-1 regulate H(2)O (2)-induced c-Jun NH(2)-terminal kinase activation and apoptosis. *Mol Biol Cell* **18**, 3903–3913.
- 26 Weinkam P, Pons J & Sali A (2012) Structure-based model of allostery predicts coupling between distant sites. *Proc Natl Acad Sci USA* **109**, 4875–4880.
- 27 Schneidman-Duhovny D, Hammel M & Sali A (2010) FoXS: a web server for rapid computation and fitting of SAXS profiles. *Nucleic Acids Res* **38**, W540–W544.
- 28 Ellman GL (1959) Tissue sulfhydryl groups. *Arch Biochem Biophys* **82**, 70–77.
- 29 Young MM, Tang N, Hempel JC, Oshiro CM, Taylor EW, Kuntz ID, Gibson BW & Dollinger G (2000) High throughput protein fold identification by using experimental constraints derived from intramolecular cross-links and mass spectrometry. *Proc Natl Acad Sci USA* **97**, 5802–5806.
- 30 Dam J, Velikovskiy CA, Mariuzza RA, Urbanke C & Schuck P (2005) Sedimentation velocity analysis of heterogeneous protein-protein interactions: Lamm equation modeling and sedimentation coefficient distributions *c(s)*. *Biophys J* **89**, 619–634.
- 31 Schuck P (2000) Size-distribution analysis of macromolecules by sedimentation velocity ultracentrifugation and lamm equation modeling. *Biophys J* **78**, 1606–1619.
- 32 Garzon JJ, Lopez-Blanco JR, Pons C, Kovacs J, Abagyan R, Fernandez-Recio J & Chacon P (2009) FRODOCK: a new approach for fast rotational protein-protein docking. *Bioinformatics* **25**, 2544–2551.
- 33 Schneidman-Duhovny D, Hammel M, Tainer JA & Sali A (2013) Accurate SAXS profile computation and its assessment by contrast variation experiments. *Biophys J* **105**, 962–974.
- 34 Vecer J & Herman P (2011) Maximum entropy analysis of analytically simulated complex fluorescence decays. *J Fluorescen* **21**, 873–881.



Contents lists available at ScienceDirect

BBA - General Subjects

journal homepage: www.elsevier.com/locate/bbagen

14-3-3 protein directly interacts with the kinase domain of calcium/calmodulin-dependent protein kinase kinase (CaMKK2)

Katarina Psenakova^{a,b,1}, Olivia Petrvalska^{a,b,1}, Salome Kylarova^{a,b,1}, Domenico Lentini Santo^a, Dana Kalabova^b, Petr Herman^c, Veronika Obsilova^{b,*}, Tomas Obsil^{a,b,**}

^a Department of Physical and Macromolecular Chemistry, Faculty of Science, Charles University, Prague, Czech Republic

^b BioCeV – Institute of Physiology, The Czech Academy of Sciences, Vestec, Czech Republic

^c Institute of Physics, Faculty of Mathematics and Physics, Charles University, Prague, Czech Republic

ARTICLE INFO

Keywords:

14-3-3 protein

CaMKK

Protein-protein interaction

SAXS

Fluorescence spectroscopy

ABSTRACT

Background: Calcium/calmodulin-dependent protein kinase kinase 2 (CaMKK2) is a member of the Ca^{2+} /calmodulin-dependent kinase (CaMK) family involved in adiposity regulation, glucose homeostasis and cancer. This upstream activator of CaMKI, CaMKIV and AMP-activated protein kinase is inhibited by phosphorylation, which also triggers an association with the scaffolding protein 14-3-3. However, the role of 14-3-3 in the regulation of CaMKK2 remains unknown.

Methods: The interaction between phosphorylated CaMKK2 and the 14-3-3 γ protein, as well as the architecture of their complex, were studied using enzyme activity measurements, small-angle x-ray scattering (SAXS), time-resolved fluorescence spectroscopy and protein crystallography.

Results: Our data suggest that the 14-3-3 protein binding does not inhibit the catalytic activity of phosphorylated CaMKK2 but rather slows down its dephosphorylation. Structural analysis indicated that the complex is flexible and that CaMKK2 is located outside the phosphopeptide-binding central channel of the 14-3-3 γ dimer. Furthermore, 14-3-3 γ appears to interact with and affect the structure of several regions of CaMKK2 outside the 14-3-3 binding motifs. In addition, the structural basis of interactions between 14-3-3 and the 14-3-3 binding motifs of CaMKK2 were elucidated by determining the crystal structures of phosphopeptides containing these motifs bound to 14-3-3.

Conclusions: 14-3-3 γ protein directly interacts with the kinase domain of CaMKK2 and the region containing the inhibitory phosphorylation site Thr¹⁴⁵ within the N-terminal extension.

General significance: Our results suggested that CaMKK isoforms differ in their 14-3-3-mediated regulations and that the interaction between 14-3-3 protein and the N-terminal 14-3-3-binding motif of CaMKK2 might be stabilized by small-molecule compounds.

1. Introduction

Calcium/calmodulin-dependent protein kinase kinase (CaMKK), a member of the Ca^{2+} /calmodulin-dependent kinase (CaMK) family, specifically phosphorylates Thr residues within the activation loop of two downstream kinases, CaMKI and CaMKIV, considerably increasing their catalytic efficiency, resulting in phosphorylation of multiple downstream targets [1]. Two CaMKK isoforms (CaMKK1 and CaMKK2) have been identified in mammals, which are both highly expressed in the brain. CaMKK2 is also an upstream activator of the AMP-activated

protein kinase (AMPK) [2], and studies have shown that the AMPK:CaMKK2 complex regulates energy balance by acting in the hypothalamus [3]. In fact, CaMKK2 is one of the most versatile CaMKs, which is involved in adiposity regulation, glucose homeostasis, hematopoiesis, inflammation, and cancer, and is considered a potential target for therapeutic intervention (reviewed in [4]).

The members of the CaMK family share a common domain organization consisting of the catalytic domain followed by an auto-inhibitory region, which overlaps with the CaM-binding region (Fig. 1A and C) [5]. Although CaMKK1 and CaMKK2 share high similarity and

Abbreviations: AMPK, AMP-activated protein kinase; AUC, Analytical ultracentrifugation; CaM, Calmodulin; CaMKK2, Calcium/calmodulin-dependent protein kinase kinase 2; SAXS, Small-angle x-ray scattering; SV, Sedimentation velocity

* Correspondence to: V. Obsilova, BioCeV – Institute of Physiology, The Czech Academy of Sciences, Prague, Czech Republic.

** Correspondence to: T. Obsil, Department of Physical and Macromolecular Chemistry, Faculty of Science, Charles University, Prague, Czech Republic.

E-mail addresses: veronika.obsilova@fgu.cas.cz (V. Obsilova), obsil@natur.cuni.cz (T. Obsil).

¹ The first three authors KP, OP and SK contributed equally to this work.

<https://doi.org/10.1016/j.bbagen.2018.04.006>

Received 16 January 2018; Received in revised form 5 April 2018; Accepted 6 April 2018
0304-4165/ © 2018 Elsevier B.V. All rights reserved.

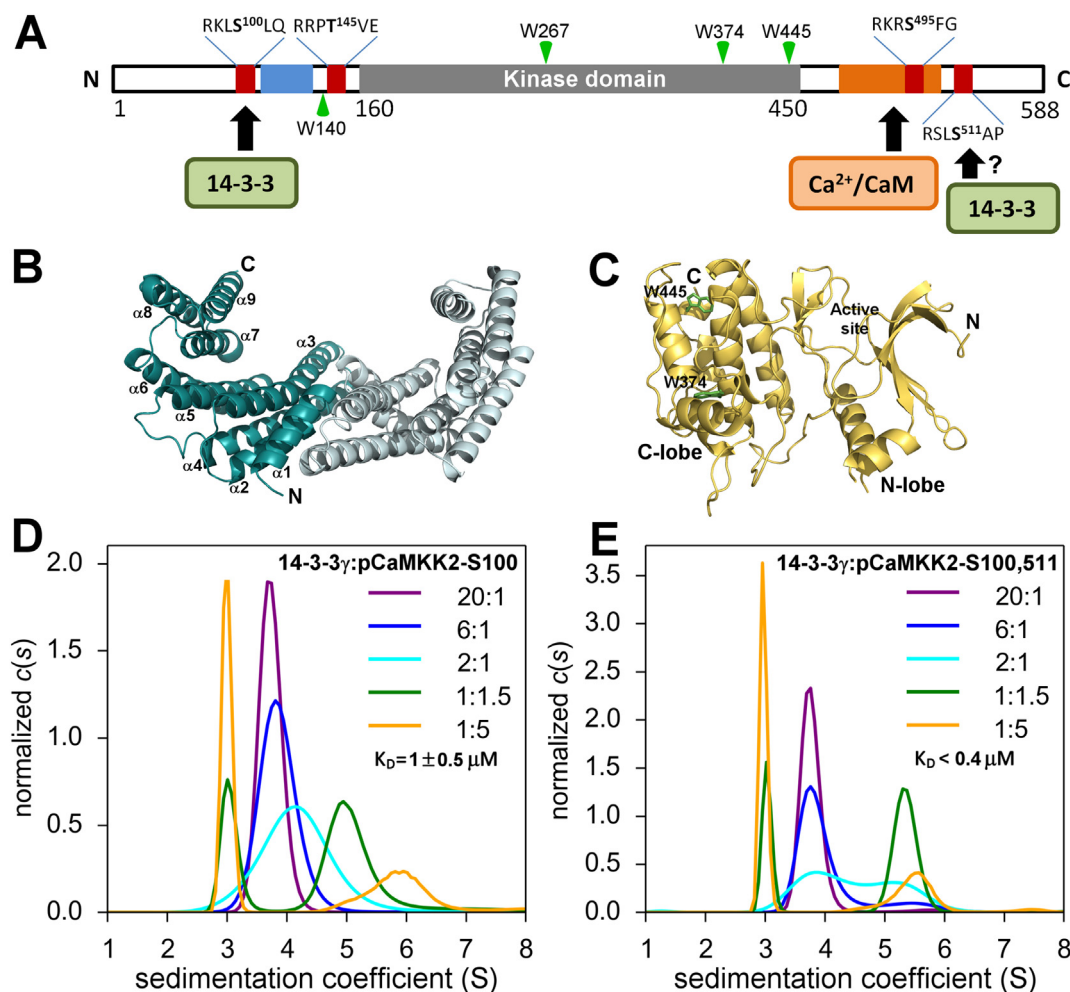


Fig. 1. Phosphorylated CaMKK2 Forms a Stable Complex with 14-3-3γ. (A) Domain structure of CaMKK2. The positions of PKA phosphorylation sites, the N-terminal regulatory site and the CaM binding region are indicated by red, blue and orange rectangles, respectively. The positions of tryptophan residues used in the time-resolved fluorescence experiments are indicated by green triangles. (B) Crystal structure of the 14-3-3γ protein dimer (PDB ID: 2B05). Each protomer is shown in different color. (C) Crystal structure of the kinase domain of CaMKK2 [35]. Tryptophan residues located in the C-lobe are shown as sticks. (D, E) Series of area-normalized *c(s)* distributions of mixtures of pCaMKK2 and 14-3-3γ at various molar ratios, using 6 μM 14-3-3γ and 0.3–30 μM pCaMKK2.

identity in their amino acid sequences (Fig. S1), they differ in their biochemical properties. CaMKK1 activity is strictly regulated by an autoinhibitory mechanism, and Ca²⁺/CaM binding relieves this autoinhibition [6]. However, in contrast to CaMKK1, CaMKK2 is significantly active in the absence of Ca²⁺/CaM [7]. This autonomous activity is regulated by a stretch of 23 amino acids (residues 129–151 in rat CaMKK2), which is located N-terminally to the catalytic domain and apparently participates in the release of the autoinhibitory region from the catalytic domain [8]. Moreover, this regulatory region contains three phosphorylation sites targeted by cyclin-dependent kinase 5 and glycogen synthase kinase 3 and one site recognized by cAMP-dependent protein kinase (PKA) [9,10].

Both CaMKKs are partly inhibited upon phosphorylation by PKA [10–12]. CaMKK1 contains five PKA phosphorylation sites, Ser⁵², Ser⁷⁴, Thr¹⁰⁸, Ser⁴⁵⁸, and Ser⁴⁷⁵, four of which are also present in CaMKK2 (Ser¹⁰⁰, Thr¹⁴⁵, Ser⁴⁹⁵, and Ser⁵¹¹) (Figs. 1A and S1). Ser⁴⁵⁸ phosphorylation has been shown to block Ca²⁺/CaM-binding, whereas Thr¹⁰⁸ phosphorylation plays a role in the regulation of CaMKK1 activity toward CaMKI and CaMKIV [10,13].

In addition to direct, PKA-mediated inhibition, CaMKK1 activity is further regulated through a PKA-dependent mechanism based on interaction with 14-3-3 proteins [14,15]. 14-3-3 proteins, a family of highly conserved dimeric proteins ubiquitously expressed in all eukaryotic cells (Fig. 1B), function as scaffold and chaperone molecules

that interact with and regulate the function of several hundred partner proteins by recognizing phosphoserine- (pS) or phosphothreonine (pT)-containing motifs [16]. Mechanistically, 14-3-3 proteins constrain the conformation, occlude sequence-specific and structural features, promote protein-protein interactions, or prevent the aggregation of their binding partners (reviewed in [17,18]). GST pull-down and co-immunoprecipitation assays, together with site-directed mutagenesis, have shown that both CaMKK isoforms bind to various 14-3-3 protein isoforms (mainly γ isoform) and that the conserved motif containing phosphorylated Ser⁷⁴ in CaMKK1 (corresponding to Ser¹⁰⁰ in CaMKK2, Figs. 1A and S1) functions as the primary 14-3-3 binding site [14,15]. Furthermore, a second 14-3-3 binding motif containing phosphorylated Ser⁴⁷⁵ in CaMKK1 (Ser⁵¹¹ in CaMKK2) has also been suggested [15]. The phosphorylation of this site by PKA, however, is low and mainly occurs in the presence of Ca²⁺/CaM [11,12,14]. The functional role of 14-3-3 binding in CaMKK regulation is apparently twofold. Davare et al. [14] suggested that the 14-3-3 binding inhibits CaMKK1 through two mechanisms, namely inhibition of Thr¹⁰⁸ dephosphorylation, thus maintaining the kinase in the PKA-mediated inhibited state, and direct inhibition of the kinase activity. Accordingly, Ichimura et al. [15] showed that binding to 14-3-3 decreases the maximum velocity (*V_{max}*) of CaMKK1. However, the molecular mechanism of this interaction as well as the role of 14-3-3 in the regulation of CaMKK2 remains unclear.

Thus, in this study, we used enzyme activity measurements, small-

angle x-ray scattering (SAXS) and time-resolved fluorescence spectroscopy to characterize the interaction between phosphorylated CaMKK2 and the 14-3-3 γ protein. In addition, to elucidate the structural basis of interactions between 14-3-3 and the 14-3-3 binding motifs of CaMKK2, we determined the crystal structures of phosphopeptides containing these motifs bound to 14-3-3.

2. Materials and methods

2.1. Expression, purification and phosphorylation of CaMKK2

DNA encoding human CaMKK2 (residues 93–517) was ligated into pRSFDuet-1 (Novagen) using *Bam*HI and *Not*I sites. Modified pRSFDuet-1 containing the sequence of the His₆-tagged GB1 domain of protein G inserted into the first multiple cloning site was a gift from Evzen Boura (Institute of Organic Chemistry and Biochemistry AS CR, Prague, Czech Republic). CaMKK2 (93–517) was expressed as N-terminal His₆-GB1-tagged fusion protein in *Escherichia coli* BL21 (DE3) cells. Protein expression was conducted in autoinduction media for 5 h at 37 °C and then 16 h at 20 °C, and the protein was purified using Chelating Sepharose Fast Flow (GE Healthcare) according to the standard protocol. The eluted protein was dialyzed against buffer containing 50 mM Tris-HCl (pH 8), 0.5 M NaCl, 4 mM 2-mercaptoethanol, 4 mM EDTA and 10% (w/v) glycerol and the His₆-GB1 tag was cleaved by incubation with TEV protease (250 U of TEV/mg of fusion protein) at 30 °C for 1 h. The final purification step was size-exclusion chromatography on a HiLoad 26/600 Superdex 75 column (GE Healthcare) in buffer containing 50 mM Tris-HCl (pH 8), 500 mM NaCl, 5 mM DTT, and 10% (w/v) glycerol. All mutants of CaMKK2 were generated using the QuikChange site-directed mutagenesis kit (Stratagene), and mutations were confirmed by sequencing. The stability of prepared mutants was assessed by measuring the temperature of the unfolding transition (T_m) using differential scanning fluorimetry [19], and no significant differences in T_m were observed. CaMKK2-S¹⁰⁰ and CaMKK2-S^{100,511} were phosphorylated by incubation at 30 °C for 3 h and then overnight at 4 °C with 170 and 340 units of PKA (Promega), respectively, per mg of protein in the presence of 0.75 mM ATP and 20 mM MgCl₂. After phosphorylation, ATP was removed by size-exclusion chromatography. The result of the phosphorylation reaction was assessed by HPLC-MS.

2.2. Expression and purification of 14-3-3 proteins

14-3-3 γ , 14-3-3 γ ΔC, 14-3-3 ζ ΔC and 14-3-3 γ noW were expressed and purified as described previously [20].

2.3. Expression and purification of CaM

Rat CaM was prepared as described previously [21].

2.4. Preparation of kinase-dead CaMK1D and AMPK2

DNA encoding human CAMK1D was a gift from Nicola Burgess-Brown (Addgene plasmid # 38834). DNA encoding human AMPK2 (catalytic α 2 subunit of AMPK) was a gift from Cheryl Arrowsmith (Addgene plasmid # 36194). The kinase-dead CAMK1D D¹⁶⁵A and AMPK2 D¹⁵⁷A mutants were generated using the QuikChange site-directed mutagenesis kit (Stratagene), and the mutation was confirmed by sequencing. Both N-terminally His₆-tagged proteins were expressed by isopropyl 1-thio- β -D-galactopyranoside induction for 16 h at 15 °C and purified from *E. coli* BL21(DE3) using Chelating Sepharose® Fast Flow (GE Healthcare) according to the standard protocol. The next purification step (only in the case of CaMK1D) was size-exclusion chromatography on a HiLoad 26/600 Superdex 75 column (GE Healthcare) in buffer containing 50 mM HEPES (pH 7.5), 200 mM NaCl, 1 mM CaCl₂, 5 mM DTT and 10% glycerol.

2.5. Enzyme activity measurements

The enzymatic activity of CaMKK2_{93–517} was examined using γ -[³²P]-ATP assay with inactive CaMKID and AMPKA as physiological kinase substrates. The reaction volume of 45 μ L consisted of 10 nM CaMKK2_{93–517} (phosphorylated or not phosphorylated), 10 μ M CaMKID (or AMPKA2), 5 μ M calmodulin and 100 μ M 14-3-3 γ (where needed) in buffer containing 50 mM HEPES (pH 7.5), 200 mM NaCl, 20 mM MgCl₂, 1 mM CaCl₂, 1 mM DTT and 10% glycerol. The reaction was tempered up to 30 °C and initiated by an addition of 5 μ L of 1 mM γ -[³²P]-ATP (PerkinElmer Life Sciences) to a final ATP concentration 100 μ M (~2–3 μ Ci per reaction). After a 5 min incubation at 30 °C, the reaction was stopped by spotting 45 μ L of the reaction mixture onto a P81 phosphocellulose paper strip (Millipore) and washing in 3 \times 500 mL of 1% (w/v) phosphoric acid for 5 min each. Strips were dried and inserted into vials containing 5 mL of scintillation fluid (Rotiszint™, Carl Roth). Counts were measured using Quantasart™ liquid analyzer (PerkinElmer Life Sciences). To determine significance for observed changes, a paired two-tail *t*-test was performed. Where indicated in the figures, a single asterisk denotes $p \leq 0.05$ and a double asterisk denotes $p \leq 0.005$.

2.6. HPLC-MS analysis

HPLC-MS analysis was performed as previously described [22,23].

2.7. Analytical ultracentrifugation

Sedimentation velocity (SV) experiments were performed using a ProteomLab™ XL-I analytical ultracentrifuge (Beckman Coulter), as previously described [22]. Samples were dialyzed against buffer containing 50 mM Tris-HCl (pH 7.5), 150 mM NaCl, and 1 mM tris(2-carboxyethyl)phosphine (TCEP) before analysis. SV experiments were conducted in charcoal-filled Epon centerpieces with 12-mm optical path length, at 20 °C, and at 42,000 rpm rotor speed (An-50 Ti rotor, Beckman Coulter), and all sedimentation profiles were recorded with absorption optics. The analysis of mixtures of pCaMKK2 and 14-3-3 γ at various molar ratios was performed with 0.3–30 μ M pCaMKK2 and 6 μ M 14-3-3 γ .

2.8. Small angle X-ray scattering

SAXS data were collected at the European Molecular Biology Laboratory (EMBL) P12 beamline, at the storage ring PETRA III (Deutsches Elektronen Synchrotron (DESY), Hamburg, Germany). The SAXS measurements were conducted in buffer containing 50 mM Tris-HCl (pH 7.5), 150 mM NaCl, 1 mM TCEP, 1 mM CaCl₂, and 3% (w/v) glycerol, using 1–2.8 mg.mL⁻¹ pCaMKK2, 1.5–3 mg.mL⁻¹ 14-3-3 γ ΔC and 9.9–16.9 mg.mL⁻¹ pCaMKK2:14-3-3 γ complex (1:2 M stoichiometry). The forward scattering $I(0)$ and the radius of gyration R_g were calculated using the Guinier approximation for a s ($s = 4\pi\sin(\theta)/\lambda$, where 2θ is the scattering angle and λ is the wavelength) range that satisfies the $sR_g < 1.3$ condition. The distance distribution functions $P(r)$ and the maximum particle dimensions D_{\max} were computed using the program GNOM [24]. The solute apparent molecular mass (MM_{exp}) was estimated by comparing the forward scattering both with that of reference solutions of bovine serum albumin and with that of the excluded volume of the hydrated particle (the Porod volume) V_p [25]. V_p was computed using the program PRIMUS [26]. The two-phase bead modeling of the pCaMKK2:14-3-3 γ complex was performed using the program MONSA [27]. The rigid body modeling of the pCaMKK2:14-3-3 γ complex was performed using the program CORAL [25], which models flexible loops missing in crystal structures as interconnected dummy residue chains attached to the appropriate Ca atoms in rigid domains. Crystal structures of 14-3-3 γ (PDB ID: 2B05) and the kinase domain of CaMKK2 (PDB ID: 5UY6) were used as rigid domains. The

analysis based on the ensemble optimization method was performed using the program EOM [28].

2.9. Fluorescence polarization assay

Various concentrations of 14-3-3 γ were incubated for 1 h with 20 nM of FITC-conjugated synthetic peptide GSLARKL(pS)LQER (FITC-CaMKK2-S100), where pS denotes phosphoserine, with a fluorescein attached to the N-terminus (Pepscan Presto BV, The Netherlands). Fluorescence polarization was measured using a CLARIOstar microplate reader (BMG Labtech) in 10 mM HEPES (pH 7.4), 150 mM NaCl, 0.1% (v/v) Tween 20 and 0.1% (w/v) BSA buffer after incubating for 1 h in a 96-well black plate. Excitation and emission wavelengths were 482 nm and 530 nm, respectively, and K_D was determined using Origin (OriginLab Corp., MA, USA).

2.10. Time-resolved fluorescence measurements

Time-resolved tryptophan fluorescence intensity and anisotropy decay measurements as well as data analysis were performed as previously described [29]. Tryptophan emission was excited at 298 nm by a tripled output of the Ti:Sapphire laser. Tryptophan fluorescence was isolated at 355 nm using a combination of monochromator and a stack of UG1 and BG40 glass filters (Thorlabs) placed in front of the input slit. Dansyl fluorescence was excited at 355 nm and collected at 550 nm. Samples were placed in a thermostatic holder, and all experiments were performed at 23 °C in buffer containing 50 mM Tris-HCl (pH 7.5), 150 mM NaCl, 1 mM TCEP, 1 mM CaCl₂ and 10% (w/v) glycerol. In tryptophan fluorescence experiments, the pCaMKK2 and 14-3-3 γ noW concentrations were 12 and 60 μ M, respectively. In dansyl fluorescence experiments, the DANS-CaM, CaMKK2 and 14-3-3 γ concentrations were 25, 28 and 100 μ M, respectively.

2.11. Crystallization, data collection and structure determination

The 14-3-3 ζ AC or 14-3-3 γ AC proteins and the pepS100 or pepS511 peptides (sequences RKLpSLQER and RSLpSAPGN, respectively) were mixed in a 1:2 M stoichiometry in buffer containing 20 mM HEPES (pH 7), 2 mM MgCl₂ and 1 mM TCEP. Crystallization was performed using the hanging-drop vapor-diffusion method at 291 K. Crystals of the 14-3-3 ζ AC:pepS100 peptide complex were grown from drops consisting of 2.5 μ L of 16.2 mg.mL⁻¹ protein and 2.5 μ L of 100 mM Tris-HCl (pH 7), 20.8% (v/v) PEG 2000 and 50 mM sodium fluoride. Crystals of the 14-3-3 γ AC:pepS511 peptide complex were grown from drops consisting of 1 μ L of 16.5 mg.mL⁻¹ protein and 2 μ L of 100 mM sodium citrate (pH 5.6), 200 mM potassium sodium tartrate, and 1.8 M ammonium sulfate. Crystals were cryoprotected using 30% (v/v) PEG 400 and flash frozen in liquid nitrogen before data collection in oscillation mode at beamline 14.1 of the BESSY synchrotron and the D8 Venture system (Bruker, MA, USA). Diffraction data processing was performed using the packages XDS and XDSAPP [30,31]. Crystal structures of the 14-3-3 ζ AC:pepS100 and 14-3-3 γ AC:pepS511 complexes were solved by molecular replacement in MOLREP [32], using the structures of 14-3-3 ζ (PDB ID: 4FJ3 [33]) and 14-3-3 γ (PDB ID: 2B05) as search models, and refined at resolutions of 2.68 and 2.84 Å, respectively, with PHENIX [34]. The atomic coordinates and structure factors of both complexes have been deposited in the RCSB PDB with accession codes 6EWU and 6FEL. All structural figures were prepared with PyMOL (<https://pymol.org/2/>).

3. Results

3.1. Preparation of phosphorylated CaMKK2

Because the 14-3-3 binding motifs of human CaMKK2 are located around pSer¹⁰⁰ and pSer⁵¹¹, flanking the kinase domain [14,15], we

restricted our analysis to the residues 93–517 containing these two motifs, the kinase domain, and the Ca²⁺/CaM binding region (hereafter referred to as CaMKK2). To prepare well-defined protein, suitable for structural analysis, the other two sites phosphorylated by PKA (Thr¹⁴⁵ and Ser⁴⁹⁵) were mutated to Ala. In addition, the mutation D³³⁰A, of the catalytic aspartate residue, was introduced into the kinase domain to avoid autophosphorylation of the recombinant protein during expression and phosphorylation by PKA. Recombinantly expressed CaMKK2_{93–517}T¹⁴⁵A, D³³⁰A, S⁴⁹⁵A (hereafter referred to as CaMKK2-S^{100,511}) was phosphorylated in vitro by PKA, and the extent of the phosphorylation reaction was determined by mass spectrometry. HPLC-MS analysis confirmed the stoichiometric phosphorylation of Ser¹⁰⁰ but only partial (approximately 50%) phosphorylation of Ser⁵¹¹ (Fig. S2). Neither the presence of Ca²⁺/CaM nor the increased concentration of PKA improved the phosphorylation status of Ser⁵¹¹. The weak phosphorylation of Ser⁵¹¹ by PKA is consistent with previous reports and indicates that, under physiological conditions, the N-terminal 14-3-3 binding motif would be significantly more phosphorylated than the C-terminal 14-3-3 binding motif [11,12,14]. Therefore, we also prepared a construct containing only the N-terminal 14-3-3 binding motif with Ser¹⁰⁰ by inserting an additional mutation, Ser⁵¹¹ to Ala (hereafter referred to as CaMKK2-S¹⁰⁰).

3.2. Phosphorylated CaMKK2 forms a stable complex with 14-3-3 γ

The formation of the complex between 14-3-3 γ and pCaMKK2 (S¹⁰⁰ and S^{100,511}) was studied using sedimentation velocity (SV) analytical ultracentrifugation (AUC) by analyzing their mixtures at various molar ratios (Fig. 1D and E). The normalized continuous sedimentation coefficient distributions $c(s)$ based on the SV AUC experiments showed that 14-3-3 γ and pCaMKK2-S¹⁰⁰ formed a complex with a weight-averaged sedimentation coefficient (corrected to 20.0 °C and to the density of water), $s_{w(20,w)}$, of 6.17 S, with a frictional ratio f/f_0 of 1.3, whereas 14-3-3 γ and pCaMKK2-S^{100,511} alone showed single peaks, with $s_{w(20,w)}$ values of 3.91 and 3.16 S, respectively. The $s_{w(20,w)}$ value of the 14-3-3 γ :pCaMKK2-S¹⁰⁰ complex corresponds to a molecular mass of ~110 kDa, thus suggesting a 2:1 M stoichiometry for the complex (105.0 kDa theoretical molecular mass). The direct modeling of the SV AUC data using the Lamm equation showed best-fit apparent equilibrium dissociation constants (K_D) of $1 \pm 0.5 \mu$ M using a Langmuir binding model with a pCaMKK2-S¹⁰⁰ molecule interacting with a 14-3-3 γ dimer.

SV-AUC analysis of mixtures of 14-3-3 γ and pCaMKK2-S^{100,511} revealed the formation of a complex with an $s_{w(20,w)}$ value of 5.72 S and with a frictional ratio f/f_0 of 1.4. This $s_{w(20,w)}$ value corresponds to a molecular mass of ~111 kDa, thus also suggesting the 2:1 M stoichiometry of the complex. The direct modeling of the SV AUC data showed a best-fit K_D of $< 0.4 \mu$ M, thus suggesting that the C-terminal motif, when phosphorylated, increases the stability of the complex.

3.3. 14-3-3 Protein binding does not inhibit the activity of pCaMKK2 but slows down its Dephosphorylation

Previous studies have shown that the 14-3-3 binding inhibits the catalytic activity of phosphorylated CaMKK1 [14,15]. To test whether the catalytic activity of pCaMKK2 is also affected by interaction with 14-3-3, the kinase activity measurements were performed. Human CaMK1D and AMPKA2 (catalytic $\alpha 2$ subunit of AMPK) were used as specific substrates. As expected, the phosphorylation by PKA significantly suppressed the activity of pCaMKK2 relative to the non-phosphorylated protein by ~50% and ~30% for CaMK1D and AMPKA2 as substrates, respectively (Fig. 2). Interestingly, the addition of 14-3-3 γ did not further suppress the activity of pCaMKK2 but rather resulted in its weak enhancement. When CaMK1D was used as a substrate, the effect was insignificant (the activity increased by 5% on a relative scale compared to the non-phosphorylated enzyme activity), but when

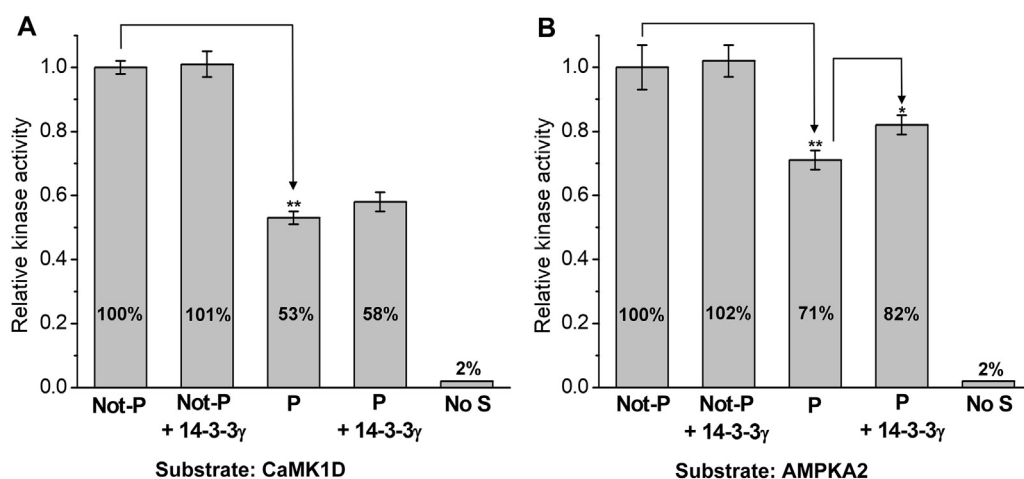


Fig. 2. 14-3-3 Protein Binding Does Not Inhibit the Catalytic Activity of Phosphorylated CaMKK2. The catalytic activity of CaMKK2 and pCaMKK2 both in the absence and the presence of 14-3-3 γ was measured using human CaMK1D (kinase-dead mutant D¹⁶⁵A) and AMPK2 (kinase-dead mutant D¹⁵⁷A) as specific substrates. The activities were normalized compared to the non-phosphorylated enzyme activity in the absence of 14-3-3 γ (specific activities were 940 ± 20 and 740 ± 50 nmol.min⁻¹.mg⁻¹ for CaMK1D and AMPK2 as substrates, respectively). Results are the means \pm S.D., $n = 3$. No S, no substrate; *, $p < 0.05$; **, $p < 0.005$.

AMPK2 was used as a substrate the pCaMKK2 activity increased significantly by 11%. This indicates that the 14-3-3-mediated regulations of pCaMKK1 and pCaMKK2 differ.

Davare et al. [14] suggested that the 14-3-3 binding inhibits CaMKK1 mainly through inhibition of Thr¹⁰⁸ (Thr¹⁴⁵ in CaMKK2) dephosphorylation, thus maintaining the kinase in the PKA-mediated inhibited state. Therefore, we next compared time-dependent overall dephosphorylation of PKA-phosphorylated pCaMKK2 by type 1 protein phosphatase (PP1) in the absence and presence of 14-3-3 γ using phos-tag SDS-PAGE. The kinase-dead mutant of pCaMKK2 D³³⁰A was used to avoid autophosphorylation of additional residues. Dephosphorylation was assessed by downward shift (Fig. S3) on a phos-tag SDS-PAGE gel. CaMKK2 shifted down gradually with incubation time through several discrete bands, which correspond to various partly phosphorylated forms of CaMKK2. As noticed, an incubation with PP1 for 7 and 30 min resulted in a substantial dephosphorylation of pCaMKK2 in the absence of 14-3-3 γ . On the other hand, the presence of 14-3-3 γ suppressed the overall dephosphorylation of pCaMKK2 as indicated by a lower abundance of bands corresponding to dephosphorylated CaMKK2 after 7 and 30 min of incubation time.

To assess dephosphorylation of specific regulatory sites Thr¹⁴⁵ and Ser⁴⁹⁵ (Thr¹⁰⁸ and Ser⁴⁵⁸ in CaMKK1) an HPLC-MS approach was used. Proteins treated by PP1 for 0, 1.5 and 7 min were collected and directly injected onto an immobilized protease column. After rapid online digestion and desalting, HPLC separation coupled with MS detection was done. Abundances of selected peptides containing Thr¹⁴⁵ and Ser⁴⁹⁵ were then estimated from intensities of their extracted ion chromatograms (Table S1). The intensity ratios between non-phosphorylated and phosphorylated forms of selected peptides indicated slower dephosphorylation of both phosphoresidues for pCaMKK2 bound to 14-3-3 γ compared with pCaMKK2 alone, especially pSer⁴⁹⁵ whose non-phosphorylated form could not be detected. This suggests that the 14-3-3 γ binding slows down the dephosphorylation of inhibitory PKA sites of pCaMKK2.

3.4. Structural characterization of the 14-3-3 binding motifs of CaMKK2

Although the putative C-terminal 14-3-3 binding motif (sequence RSLpSer⁵¹¹AP) is a canonical “mode I” 14-3-3 binding site (RXX(pS/pT)XP, wherein pS/pT is phosphoserine or phosphothreonine and X is any residue [36,37]), the N-terminal motif (sequence RKLpS¹⁰⁰LQE) contains a Gln residue at the position +2 relative to the phosphorylated residue pSer¹⁰⁰ (Fig. 1A). Bioinformatics survey of 14-3-3 binding sites revealed that Gln is seldom found at +2 because the Pro residue and, to a lesser extent, Ser, Gly and Asp also, are frequently found at this position [38]. The frequent occurrence of proline at the +2 position is explained by the need to introduce a kink in the peptide chain and to

direct the C-terminal portion out of the ligand binding groove of the 14-3-3 protein [36]. To elucidate the structural basis of interactions between 14-3-3 proteins and the 14-3-3 binding motifs of CaMKK2, we solved the crystal structures of phosphopeptides pepS100 (sequence RKLpSLQER) and pepS511 (sequence RSLpSAPGN) bound to 14-3-3 ζ AC and 14-3-3 γ AC, respectively (Δ C denotes C-terminally truncated versions missing the highly flexible ~15-residues-long C-terminal tail [39]). The 14-3-3 isoforms were selected based on quality of the resulting crystals. The crystal structures were solved by molecular replacement using the structures of 14-3-3 ζ (PDB ID: 4FJ3 [33]) and 14-3-3 γ (PDB ID: 2B05) as search models, and refined at a resolution of 2.68 and 2.84 Å, respectively (Table 1). The final electron densities allowed us to build seven residues (KLpSLQER, Fig. 3A and B) of pepS100 and six residues (RSLpSAP, Fig. 3C and D) of pepS511.

The main-chain conformations of both phosphopeptides in the 14-3-3 binding grooves are similar to those previously observed in other 14-3-3 protein complexes [33,37,40–42]. The 14-3-3 ζ side chains coordinating the pSer¹⁰⁰ moiety of pepS100 include Arg⁵⁶, Arg¹²⁷, and Tyr¹²⁸ (Fig. 3B). Although the side-chain of the Glu residue at the +3 position relative to pSer¹⁰⁰ is salt-bridged to the Lys¹²⁰ of 14-3-3 ζ , the side-chain of the Gln residue at +2 is hydrogen-bonded to the phosphate and to the main-chain carbonyl groups of pSer¹⁰⁰. These interactions apparently force the direction of the polypeptide chain to change, thus mimicking the role of the Pro residue, as previously observed, for example, in the 14-3-3 binding motifs of yeast neutral trehalase, which also lacks a Pro residue at the +2 position relative to the phosphorylated residue (Fig. 3E) [42]. In the case of pepS511, which contains the canonical “mode I” 14-3-3 binding motif, the coordination of the pSer⁵¹¹ moiety and all other contacts are identical to those previously observed in other complexes of peptides with the “mode I” motif.

3.5. The 14-3-3 γ :pCaMKK2 complex is flexible and elongated

Because all our attempts to grow crystals of the 14-3-3 γ :pCaMKK2-S¹⁰⁰ and 14-3-3 γ :pCaMKK2-S^{100,511} complexes failed, we used SAXS analysis to structurally characterize the interaction between 14-3-3 γ and pCaMKK2 in solution. We and other researchers have previously used a similar approach to characterize various 14-3-3 protein complexes [22,41,45]. X-ray scattering data were collected for CaMKK2-S¹⁰⁰, 14-3-3 γ AC and both complexes prepared with 2:1 M stoichiometry (Table 2). The linearity of the Guinier plots (Fig. 4B), the lack of a significant variation in forward scattering intensity $I(0)$ with the concentration, the Porod volume V_p and the radius of gyration R_g (Table 2) confirmed the absence of aggregation and the stability of the complexes within the concentration range tested. The apparent M_w values of ~47 and ~54 kDa for CaMKK2 and 14-3-3 γ AC, respectively, estimated based

Table 1
Crystallographic data collection and refinement statistics.

Complex	14-3-3 ζ AC:pepS100	14-3-3 γ AC:pepS511
Wavelength (Å)	0.9184	1.3418
Space group	P212121	R3
Unit-cell parameters		
<i>a</i> , <i>b</i> , <i>c</i> (Å)	56.95, 60.31, 262.19	115.73, 115.73, 203.96
α , β , γ (°)	90, 90, 90	90, 90, 120
Asymmetric unit contents	Two dimers of 14-3-3 ζ AC with bound phosphopeptides	Two dimers of 14-3-3 γ AC with bound phosphopeptides
Resolution range (Å) ^a	47.71–2.68 (2.84–2.68)	26.82–2.84 (2.94–2.84)
Unique reflections	26,274 (4126)	22,801 (2424)
Data multiplicity	6.42 (6.23)	10.85 (10.81)
Completeness (%)	99.7 (98.9)	94.4 (99.4)
$\langle I/\sigma(I) \rangle$	17.37 (5.21)	11.19 (2.26)
<i>R</i> _{meas} ^b	0.08 (0.3)	0.26 (0.97)
<i>R</i> _{work} ^c	0.208	0.228
<i>R</i> _{free} ^c	0.234	0.280
No. of protein atoms	7118	7402
No. of waters	114	35
Average B factors (Å ²)		
Protein	50.34	40.87
Water	41.77	34.55
R.m.s. ^d deviations from ideal values		
Bond lengths (Å)	0.009	0.004
Bond angles (°)	0.97	0.55
Ramachandran favored (%)	95.51	98.88
Ramachandran allowed (%)	4.49	1.12
Ramachandran outliers (%)	0	0

^a Values in parentheses are for the highest resolution shell.

^b $R_{meas} = \sum_{hkl} \{N(hkl)/[N(hkl) - 1]\}^{1/2} \times \sum_i |I_i(hkl) - \langle I(hkl) \rangle| / \sum_{hkl} I_i(hkl)$,

where $I(hkl)$ is the intensity of reflection hkl , $\langle I(hkl) \rangle = \frac{1}{N(hkl)} \sum_i I_i(hkl)$, and $N(hkl)$ the multiplicity.

^c The free *R* value (*R*_{free}) was calculated using 5% of the reflections, which were omitted from the refinement.

^d R.m.s., root mean square.

on the $I(0)$, correspond well with their expected M_w values of 48.0 and 54.3 kDa, respectively. The apparent M_w of 92–95 and 94–97 kDa of the 14-3-3 γ AC:pCaMKK2-S¹⁰⁰ and 14-3-3 γ AC:pCaMKK2-S^{100,511} complexes, respectively, as well as their V_p (~160 nm³), also indicate a 2:1 M stoichiometry (theoretical M_w 102.3 kDa), thus corroborating the SV AUC results (for globular proteins, $M_w \approx V_p \times 0.625$).

The comparison of the calculated distance distribution functions, $P(r)$, is shown in Fig. 4C. The $P(r)$ functions of CaMKK2 alone and of both complexes show significant asymmetry and longer intra-particle distances and a larger maximum particle distance (D_{max}) than those of the 14-3-3 γ AC dimer alone, thus suggesting that their molecules are more extended. This is also supported by their R_g and D_{max} values (Table 2), which are significantly larger than those of spherical proteins consisting of 430 (CaMKK2) and 944 (the 14-3-3 γ AC:pCaMKK2 complex) residues ($R_g \sim 3N^{1/3}$, where N is the number of residues; $D_{max} \sim 2.6R_g$). Moreover, the analysis of scattering data showed that the 14-3-3 γ AC:pCaMKK2-S^{100,511} complex has lower R_g and D_{max} values than the 14-3-3 γ AC:pCaMKK2-S¹⁰⁰ complex (Table 2), thus indicating that CaMKK2 phosphorylated at both motifs forms a more compact complex with 14-3-3 γ . However, it should be noted that the 14-3-3 γ AC:pCaMKK2-S^{100,511} complex was prepared using pCaMKK2-S^{100,511}, which was not completely phosphorylated at Ser⁵¹¹ (Fig. S2). Therefore, the values of R_g and D_{max} were assessed in a mixture of two complexes where either the N-terminal motif or both motifs are docked within the binding grooves of the 14-3-3 dimer.

14-3-3 binding motifs are frequently located within long

intrinsically disordered segments found in most 14-3-3 binding partners [46]. Apparently, CaMKK2 is not an exception because the analysis of protein disorder using the web servers PrDOS [47] and IUPred [48] suggested that its N- and C-terminal segments (residues 1–155 and 495–588) are significantly disordered (Fig. S4). These segments flank the structured kinase domain and contain both 14-3-3 binding motifs, as well as other regulatory regions (Fig. 1A). Indeed, the analysis of protein disorder using the dimensionless Kratky plot ($(sR_g)^2 I(s)/I(0)$ versus sR_g) suggested that CaMKK2 and both complexes have higher conformational flexibility than 14-3-3 γ AC (Fig. 4D). The scattering data for compact globular proteins in this plot show a maximum value of 1.104 at $sR_g \sim 1.73$ [49]. In addition, only 14-3-3 γ AC showed a bell-shaped curve with an $(sR_g)^2 I(s)/I(0)$ maximum of ~1.1 at an sR_g value of 1.7 (marked by cyan lines in Fig. 4D). Moreover, a more gradual decrease toward zero at higher sR_g and a higher maximum indicated that the 14-3-3 γ AC:pCaMKK2-S¹⁰⁰ complex has a higher conformational flexibility than the pCaMKK2-S^{100,511} complex, most likely resulting from the absence of interaction between 14-3-3 and the C-terminal segment of pCaMKK2-S¹⁰⁰.

3.6. Structural architecture of the 14-3-3 γ :pCaMKK2 complex in solution

SAXS-based structural modeling was performed only for the 14-3-3 γ AC:pCaMKK2-S¹⁰⁰ complex. The 14-3-3 γ AC:pCaMKK2-S^{100,511} complex was excluded from this analysis due to the heterogeneity caused by the incomplete phosphorylation of the C-terminal motif at Ser⁵¹¹ (Fig. S2). Moreover, the 14-3-3 γ AC:pCaMKK2-S¹⁰⁰ complex likely represents a physiologically more relevant form, considering the weak phosphorylation of Ser⁵¹¹ [11,12,14]. To determine the relative positions of 14-3-3 and CaMKK2 within the complex, multiphase modeling was performed to obtain ab initio bead models that include two phases representing individual components within a low-resolution shape [50]. Twenty independent models generated using the program MONSA [27] showed similar shape with a mean normalized spatial discrepancy (NSD) value of 0.61. The final model (Fig. 5A), the most typical model selected from all models calculated based on the lowest NSD value, showed a good approximation to the experimental SAXS data (Fig. S5). The calculated molecular envelope had an asymmetric shape, with most of the CaMKK2 phase located not in the central channel of the 14-3-3 dimer (a deep depression in the center of the 14-3-3 phase) but rather attached to the side of the 14-3-3 dimer and stretching out into the solution.

Subsequently, rigid-body modeling of the 14-3-3 γ AC:pCaMKK2-S¹⁰⁰ complex was performed using the program CORAL [25] and the crystal structures of 14-3-3 γ AC (PDB ID: 2B05) and of the kinase domain of CaMKK2 [35]. The N-terminal 14-3-3 binding motif was restrained in the ligand-binding groove of 14-3-3 γ , as previously observed in the crystal structure of the 14-3-3 γ AC:pepS100 complex (Fig. 3A), and unstructured segments missing in the crystal structure were modeled as dummy residue chains. The final CORAL model fitted the SAXS data, with a χ^2 value of 1.33, and showed an asymmetric overall shape similar to that of the kinase domain of CaMKK2 located outside the central channel of the 14-3-3 γ dimer (Fig. 5B and D). The model suggests that pCaMKK2-S¹⁰⁰ interacts with 14-3-3 γ not only through the phosphorylated N-terminal motif but also via a direct contact between the kinase domain and the 14-3-3 surface, in contrast to an extended state with CaMKK2 tethered to 14-3-3 only via a single phosphosite. Moreover, the presence of additional contacts between 14-3-3 γ and pCaMKK2-S¹⁰⁰, outside the phosphorylated motif and the 14-3-3 binding groove, was corroborated by the binding affinity of pCaMKK2-S¹⁰⁰ (K_D of ~1 μ M, Fig. 1B), which was significantly higher than that of the synthetic phosphopeptide containing only the N-terminal 14-3-3 binding motif that binds 14-3-3 γ with a K_D of 9 μ M (Fig. S6).

Because the 14-3-3 binding motif and the kinase domain of pCaMKK2-S¹⁰⁰ are separated by a 60-residue-long segment, which is predicted to be unstructured (Figs. 1A and S4), in solution, the 14-3-

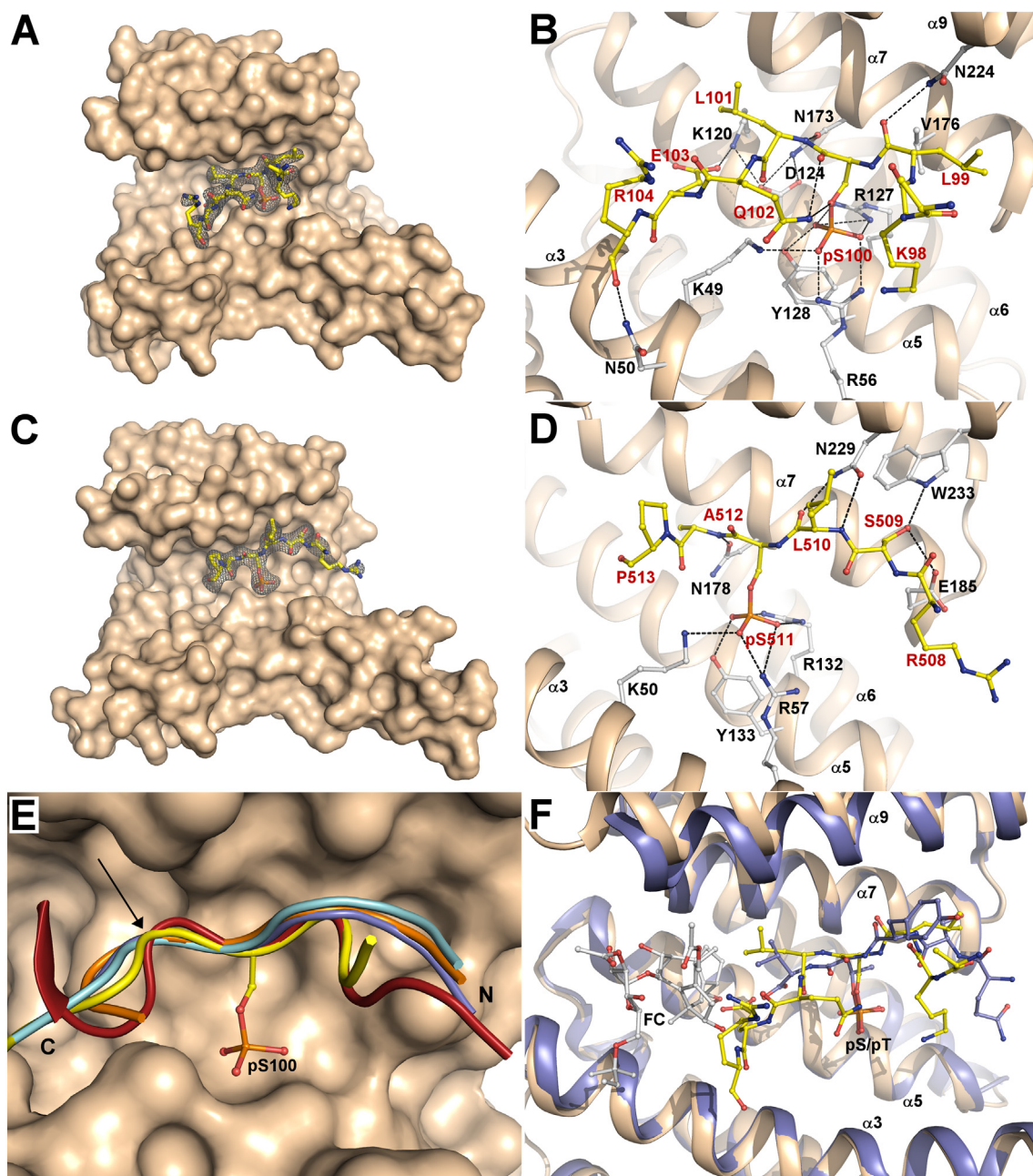


Fig. 3. Contacts between 14-3-3 and the 14-3-3 Binding Motifs of pCaMKK2. (A) Crystal structure of the 14-3-3 ζ :pepS100 complex. The $2F_o - F_c$ electron density map is contoured at 1σ . (B) Detailed view of contacts between 14-3-3 ζ and the pepS100 peptide. The CaMKK2 residues are labeled in red, and the 14-3-3 ζ residues are labeled in black. (C) Crystal structure of the 14-3-3 γ :pepS511 complex. The $2F_o - F_c$ electron density map is contoured at 1σ . (D) Detailed view of contacts between 14-3-3 γ and the pepS511 peptide. The CaMKK2 residues are labeled in red, and the 14-3-3 γ residues are labeled in black. (E) Comparison of the main-chain conformation of pepS100 (yellow) and pepS511 (violet) peptides with a “mode 1” 14-3-3 peptide (sequence RSHpSYPA, PDB ID: 1QJB, orange) [37], the 14-3-3 binding motifs of AANAT (sequence RRHpTLPA, PDB ID: 1IB1, cyan) [43] and neutral trehalase Nth1 (sequence TRRGpSEDDT, PDB ID: 5N6N, red) [42]. The C-terminal portion of the 14-3-3 binding motifs is indicated by a black arrow. (F) Superimposition of the 14-3-3 ζ :pepS100 complex (pepS100 is shown in yellow) with the ternary complex between the “mode 3” phosphopeptide derived from the C-terminus of plant plasma membrane H^+ -ATPase (sequence QSYpTV, shown as violet sticks), plant 14-3-3C (violet) and fusicoccin (FC, PDB ID: 1O9F) [44].

3 γ Δ C:pCaMKK2-S¹⁰⁰ complex may adopt different conformations. Moreover, the presence of conformational flexibility in the complex was indicated by the dimensionless Kratky plot (Fig. 4D). Therefore, we also attempted to model the complex as an ensemble of conformers using the program EOM [28]. The 14-3-3 γ Δ C dimer, the 14-3-3 binding motif and the kinase domain of CaMKK2 were treated as rigid bodies and the flexible N- and C-terminal segments of CaMKK2 as chains of dummy residues. An initial pool of 10,000 conformers was generated and a genetic algorithm was then used to select an ensemble of conformers

that collectively fit the experimental SAXS data. The selected ensemble of conformers fits the experimental scattering data with a χ^2 value of 1.22 (Fig. 5D). The R_g and D_{max} distributions calculated from the optimized ensemble are shown in Fig. 5C. The R_g distribution of the EOM-selected ensemble is biased toward more compact structures with lower R_g values than those of the pool. The average R_g and D_{max} values of the ensemble (42.4 and 149 Å, respectively) are consistent with values calculated from the scattering curves (Table 2). In addition, the R_g and D_{max} distributions of the 14-3-3 γ Δ C:pCaMKK2-S¹⁰⁰ complex have

Table 2

Structural parameters determined from SAXS data.

	c (mg.mL ⁻¹)	R_g (Å) ^b	R_g (Å) ^c	D_{max} (Å)	V_p ^d (nm ³)	M_w ^{e,g} (kDa)	M_w ^{f,g} (kDa)
14-3-3γΔC ^a	3.0	28.7 ± 0.4	28.6 ± 0.4	89	77.8	54 ± 1	49
	1.5	29.0 ± 0.4	29.0 ± 0.4	89	82.8	55 ± 1	52
CaMKK2	2.8	32.6 ± 0.3	32.7 ± 0.3	126	95.6	48 ± 1	60
	2.1	32.1 ± 0.3	32.2 ± 0.3	125	94.0	46 ± 1	59
Complex pSer ¹⁰⁰	16.9	42.3 ± 0.6	42.4 ± 0.6	146	160.4	92 ± 1	100
	12.6	42.5 ± 0.6	42.6 ± 0.6	144	163.4	95 ± 1	102
	9.9	42.4 ± 0.6	42.5 ± 0.6	146	161.1	94 ± 1	101
Complex pSer ^{100,511}	11.9	39.9 ± 0.7	40.0 ± 0.7	141	164.8	97 ± 1	103
	6.5	39.1 ± 0.6	39.2 ± 0.6	141	159.6	94 ± 1	100

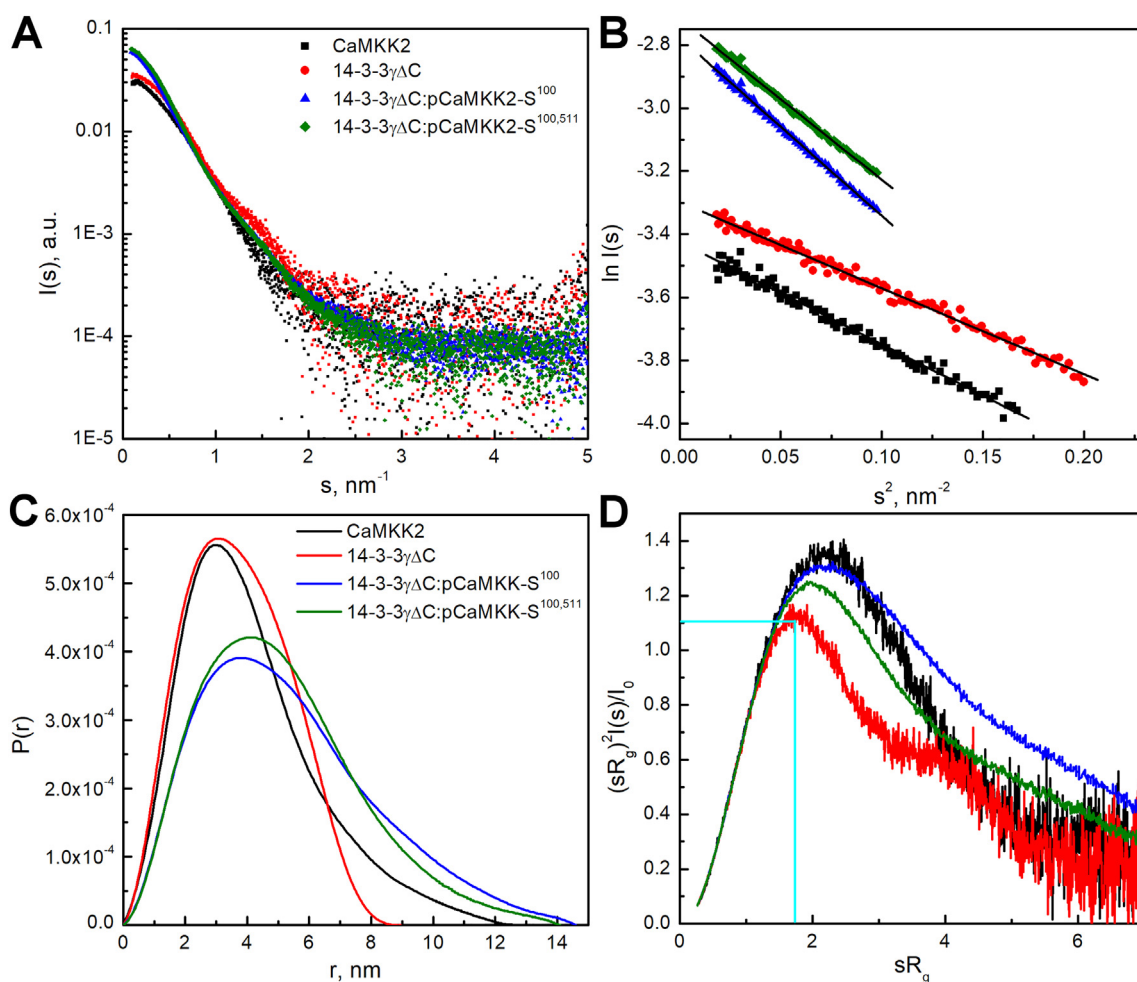
^a 14-3-3γ missing its C-terminal 13 residues.^b Calculated using Guinier approximation.^c Calculated using the program GNOM.^d The excluded volume of the hydrated particle (the Porod volume).^e Molecular weight estimated by comparing the forward scattering intensity $I(0)$ with that of the reference solution of bovine serum albumin.^f Molecular weight estimated from the Porod volume ($M_w \approx V_p \times 0.625$) [25].^g Theoretical molecular weights of the 14-3-3γΔC dimer, pCaMKK2 and the pCaMKK2:14-3-3γΔC complex (with 2:1 stoichiometry) are 54.3, 48.0 and 102.3 kDa, respectively.

Fig. 4. SAXS Analysis of the 14-3-3γ:pCaMKK2 Complexes. (A) Scattering intensity as a function of the scattering vector s ($s = 4\pi\sin(\theta/\lambda)$, where 2θ is the scattering angle, and λ is the wavelength) of 14-3-3γΔC, CaMKK2-S¹⁰⁰, and the 14-3-3γΔC:pCaMKK2-S¹⁰⁰ and 14-3-3γΔC:pCaMKK2-S^{100,511} complexes were mixed at 2:1 M stoichiometry. (B) Guinier plots for scattering curves shown in panel A. (C) Distance distribution functions $P(r)$ calculated from scattering data using the program GNOM [24]. (D) Dimensionless Kratky plots. Cyan lines mark the maximum at a value of 1.104 for $sR_g = 1.73$, which is characteristic for the scattering data of compact globular proteins [49].

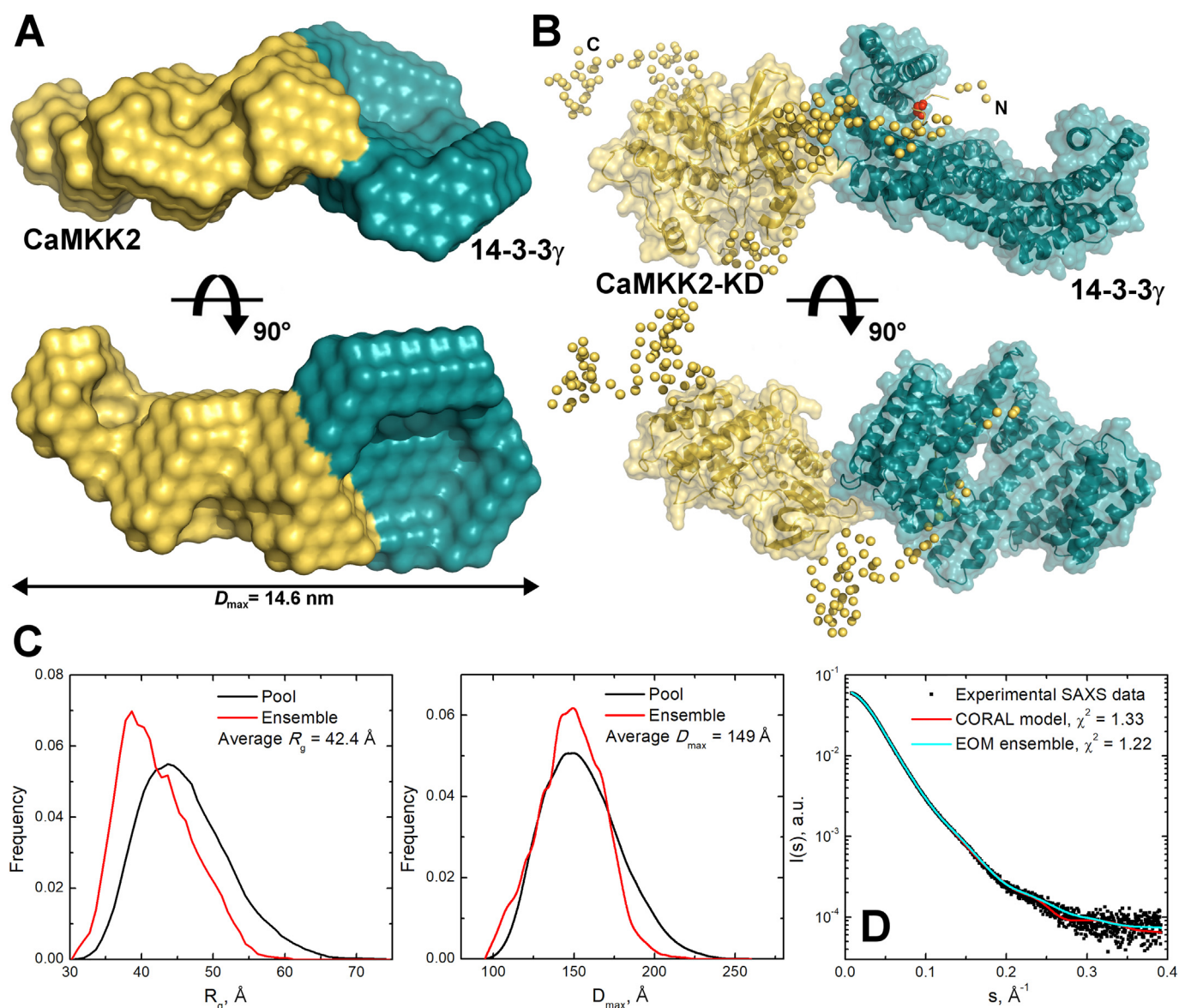


Fig. 5. SAXS-Based Structural Modeling of the 14-3-3 γ :pCaMKK2 Complex. (A) Most typical multiphase reconstruction for the 14-3-3 γ :pCaMKK2-S¹⁰⁰ complex with the 14-3-3 phase colored in cyan and the CaMKK2 phase colored in yellow. (B) Typical conformation of the 14-3-3 γ :pCaMKK2-S¹⁰⁰ complex obtained in the program CORAL using the crystal structures of 14-3-3 γ ΔC (PDB ID: 2B05) and the kinase domain of CaMKK2 (CaMKK-KD, PDB ID: 2ZV2 [35]). The unstructured segments missing in the crystal structure were modeled as dummy residue chains. The residue Ser¹⁰⁰ is shown in red. (C) Distributions of R_g and D_{max} values of the 14-3-3 γ :pCaMKK2-S¹⁰⁰ complex conformations from ensemble selected by the program EOM [28]. (D) Experimental scattering curve of the complex superimposed with the calculated curves of the CORAL model shown in panel B (red) and the ensemble selected by the program EOM (cyan).

smaller extents than those of the pools, indicating that its accessible conformations are not fully randomly distributed and that the complex is unable to be fully extended in solution, thereby suggesting that 14-3-3 γ ΔC interacts with the kinase domain and with pCaMKK2 linkers in solution. Thus, these results are consistent with the MONSA and the CORAL models.

3.7. 14-3-3 γ binding does not affect Ca²⁺/CaM binding to pCaMKK2

A common mechanism of action of the 14-3-3 protein is the interference with protein-protein interactions of its ligand. In the case of CaMKK, 14-3-3 could affect Ca²⁺/CaM binding to the C-terminus of CaMKK. To test this hypothesis, Ca²⁺/CaM binding to pCaMKK2-S¹⁰⁰ and to pCaMKK2-S^{100,511} was investigated in the absence and presence of 14-3-3 γ . For such purpose, dansyl-labeled CaM [51] was prepared, and its interaction with pCaMKK2 was monitored using time-resolved

fluorescence intensity and anisotropy decay measurements (Table 3 and Fig. 6). The analysis of these measurements showed that Ca²⁺/CaM binding to pCaMKK2 significantly increased the mean excited-state lifetime (τ_{mean}) and the longest correlation time ϕ_4 of the dansyl moiety, thus reflecting a decrease in the overall rotational diffusion coefficient upon complex formation, which indicates Ca²⁺/CaM binding to both pCaMKK2 variants. The mutual interaction is clearly visible by the naked eye because the complexes have slower anisotropy decays than free Ca²⁺/CaM, as shown in Fig. 6A, B. Although 14-3-3 γ addition to the pCaMKK2-S¹⁰⁰:Ca²⁺/CaM complex failed to induce any significant change in the dansyl anisotropy decay (open triangles in Fig. 6A), in the case of the pCaMKK2-S^{100,511}:Ca²⁺/CaM complex, the presence of 14-3-3 γ resulted in an additional increase of the rotational correlation time ϕ_4 , as clearly seen in the raw data from the elevation of the anisotropy decay tail (open triangles in Fig. 6B). This indicates a significant change in the hydrodynamic properties of the complex,

Table 3

Summary of time-resolved Dans-CaM fluorescence measurements.

Sample	$\tau_{mean}^{a,b}$ (ns)	K_{SV}^c (M ⁻¹)	$k_t (\times 10^{-5})^f$ (M ⁻¹ s ⁻¹)	ϕ_1^d (ns)	β_1^c	ϕ_2 (ns)	β_2	ϕ_3 (ns)	β_3	ϕ_4 (ns)	β_4
Dansyl-CaM	15.2	0.18	120	< 0.1	0.03	0.6	0.02	2.5	0.10	9.3	0.12
+ 14-3-3 γ	15.9	0.19	120	< 0.1	0.03	0.5	0.02	1.9	0.08	8.4	0.15
+ S ¹⁰⁰	20.5	0.01	4			2.5	0.01	12	0.11	49	0.15
+ S ¹⁰⁰ + 14-3-3 γ	20.5	0.00	0			3.0	0.01	11	0.10	49	0.16
+ S ^{100,511}	20.6	0.01	3			4.7	0.03	16	0.10	52	0.15
+ S ^{100,511} + 14-3-3 γ	20.2	0.11	53			2.8	0.02	12	0.08	88	0.16

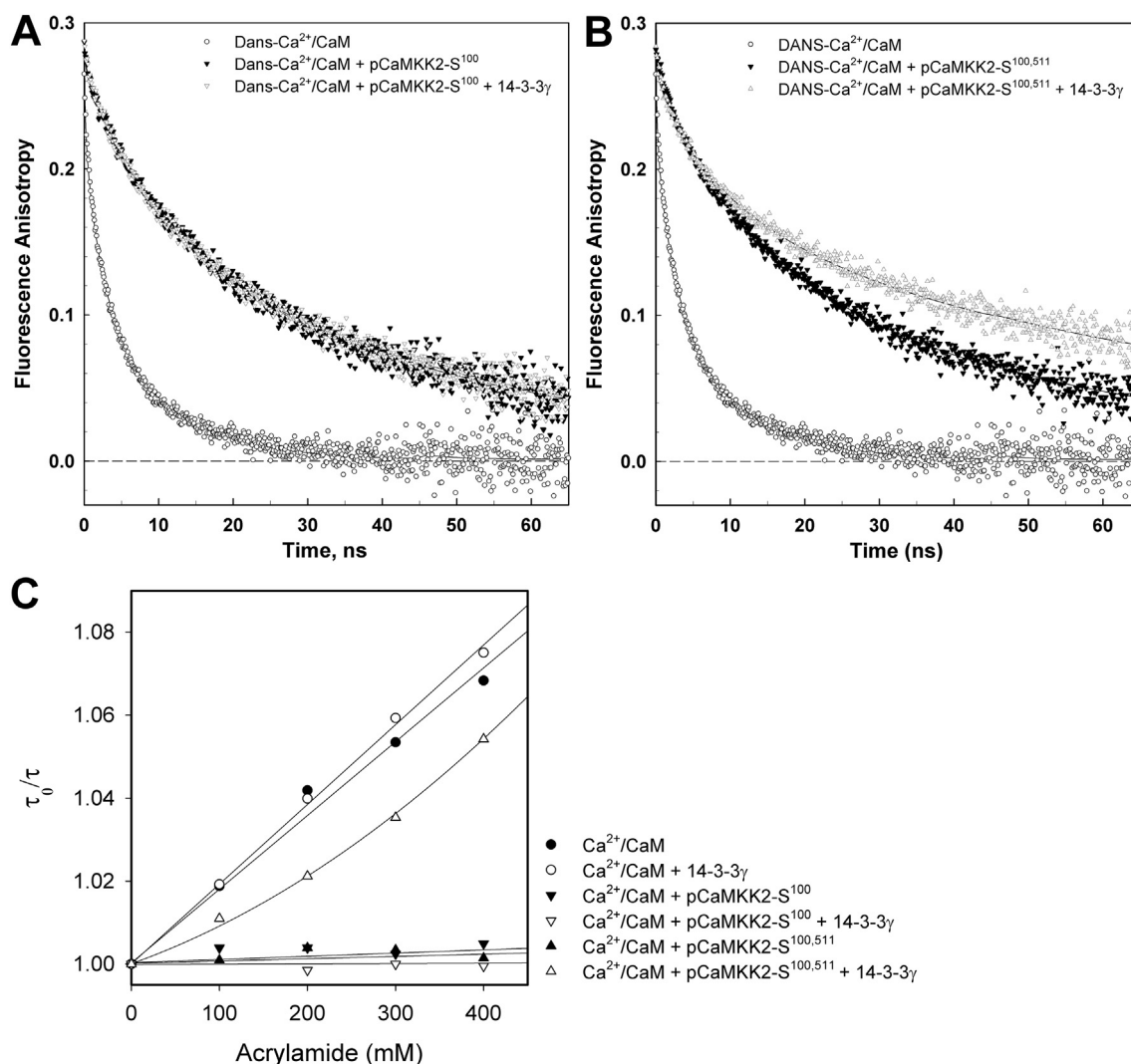
^a Mean lifetimes were calculated as $\tau_{mean} = \sum f_i \tau_i$, where f_i is an intensity fraction of the i -th lifetime component τ_i .^b S.D. value is ± 0.1 ns.^c The anisotropies $r(t)$ were analyzed for a series of exponentials by a model-independent maximum entropy method.^d Fast unresolved component.^e Stern-Volmer constant of acrylamide quenching.^f Bimolecular quenching constant for acrylamide collisional quenching.

Fig. 6. Time-Resolved Dansyl Fluorescence Measurements. (A) Fluorescence anisotropy decays of free dansyl-Ca²⁺/CaM (open circles) and dansyl-Ca²⁺/CaM in the presence of pCaMKK2-S¹⁰⁰ (closed triangles), and pCaMKK2-S¹⁰⁰ and 14-3-3 γ (open triangles). (B) Fluorescence anisotropy decays of free dansyl-Ca²⁺/CaM (open circles) and dansyl-Ca²⁺/CaM in the presence of pCaMKK2-S^{100,511} (closed triangles) and pCaMKK2-S^{100,511} and 14-3-3 γ (open triangles). (C) Acrylamide quenching of dansyl-Ca²⁺/CaM fluorescence. Quenching of free dansyl-Ca²⁺/CaM (●) is dramatically reduced in the presence of pCaMKK2-S¹⁰⁰ (▼) and pCaMKK2-S^{100,511} (▲). Although 14-3-3 γ addition to the dansyl-Ca²⁺/CaM/pCaMKK2-S¹⁰⁰ mixture only slightly increases the shielding of the dansyl fluorophore from the quencher (▽), its addition to the dansyl-Ca²⁺/CaM/pCaMKK2-S^{100,511} mixture significantly increases dansyl accessibility to acrylamide (Δ), indicating a conformational change of the complex. 14-3-3 γ addition to dansyl-Ca²⁺/CaM causes virtually no effect in the control sample (○).

likely reflecting the binding of the phosphorylated C-terminal motif of pCaMKK2-S^{100,511} to the binding groove of the second 14-3-3 γ protomer that results in a formation of apparently larger rotor. Negligible changes in the τ_{mean} of the dansyl moiety, observed in the presence of 14-3-3 γ , suggested that 14-3-3 γ binding has no effect on the stability of the pCaMKK2:Ca²⁺/CaM complex. This result was further corroborated by acrylamide quenching of dansyl-CaM fluorescence (Fig. 6C). More specifically, quenching of free dansyl-Ca²⁺/CaM markedly decreased in the presence of both pCaMKK2 variants. Although 14-3-3 γ addition to the pCaMKK2-S¹⁰⁰:Ca²⁺/CaM complex caused only a slight increase in the shielding of the dansyl fluorophore from the quencher, 14-3-3 γ addition to the pCaMKK2-S^{100,511}:Ca²⁺/CaM complex resulted in a significant increase of dansyl accessibility to acrylamide, thus indicating a conformational change in the vicinity of bound Ca²⁺/CaM, most likely due to the interaction between the C-terminal motif and 14-3-3 γ .

3.8. Conformational behavior of CaMKK2 and its changes upon 14-3-3 γ binding

Time-resolved tryptophan fluorescence measurements were then performed to investigate the conformational behavior of pCaMKK2-S¹⁰⁰ upon 14-3-3 γ binding. Four CaMKK2-S¹⁰⁰ mutants containing a single tryptophan residue (Trp¹⁴⁰, Trp²⁶⁷, Trp³⁷⁴ and Trp⁴⁴⁵) were prepared (Fig. 1A). The sequence of CaMKK2_{93–517} contains two tryptophan residues, Trp³⁷⁴ and Trp⁴⁴⁵, both located within the C-lobe of the kinase domain (Fig. 1C). Therefore, mutants containing single Trp³⁷⁴ or Trp⁴⁴⁵ were created by mutating the other residue to Phe. Mutants containing Trp¹⁴⁰ and Trp²⁶⁷ located within the N-terminal linker, close to the regulatory phosphorylation site Thr¹⁴⁵, and the N-lobe of the kinase domain, respectively, were generated by mutating both Trp³⁷⁴ and Trp⁴⁴⁵ to Phe and by introducing a single Trp residue at the desired position. The fluorescently silent 14-3-3 γ noW missing all Trp residues was used in all tryptophan fluorescence measurements [52].

Fluorescence intensity decay measurements showed that the 14-3-3 γ noW binding causes a small, albeit significant, increase in the τ_{mean} of Trp¹⁴⁰ and Trp⁴⁴⁵, whereas nonsignificant effects were assessed on mutants containing Trp²⁶⁷ and Trp³⁷⁴ (Table 4). The τ_{mean} prolongation of both mutants is clearly visible in the raw data shown in Fig. 7A and B, wherein the difference between fluorescence decays in the presence and absence of 14-3-3 is undoubtedly higher than the data noise level. The analysis of the lifetime distribution, shown in Fig. 7C and D,

Table 4
Summary of time-resolved tryptophan fluorescence measurements.

pCaMKK-S ¹⁰⁰ mutant	$\tau_{\text{mean}}^{\text{a,b}}$ (ns)	ϕ_1 (ns)	β_1	ϕ_2 (ns)	β_2	ϕ_3^{c} (ns)	β_3
W140	4.19	1.4	0.037			72	0.170
W140 + 14-3-3 γ noW	4.34	0.8	0.021	3.5	0.029	100	0.161
W267	4.88	0.9	0.014			53	0.200
W267 + 14-3-3 γ noW	4.97	0.9	0.004	5.3	0.006	79	0.197
W445	2.47	2.3	0.026			84	0.184
W445 + 14-3-3 γ noW	2.59	2.8	0.041			> 100 ^d	0.171
W374	4.39	0.9	0.004			44	0.205
W374 + 14-3-3 γ noW	4.37	0.5	0.005			61	0.206

^a Mean lifetimes were calculated as $\tau_{\text{mean}} = \sum f_i \tau_i$, where f_i is an intensity fraction of the i -th lifetime component τ_i .

^b S.D. value is ± 0.05 ns.

^c S.D. value is about ± 10 ns.

^d Poorly resolved correlation time of the overall protein rotation; SD is highly asymmetric to longer values. The resolution is primarily limited by a short lifetime value.

indicates an increase in the τ_{mean} of Trp¹⁴⁰ upon 14-3-3 binding, mainly caused by the appearance of a new lifetime component centered around 8 ns, and a decrease in the intensity fractions associated with the shorter lifetime components. Similarly, 14-3-3 binding induced an increase in the τ_{mean} of Trp⁴⁴⁵, mainly caused by the extension of the longest lifetime component around 5 ns and by the significant increase in its intensity fraction. The statistical significance of the observed difference is supported by the Monte Carlo confidence-interval analysis [53] shown in Fig. S7. The increase in τ_{mean} indicates a small 14-3-3 γ binding-induced change of quenching interactions and/or polarity near these two Trp residues.

Subsequently, the segmental motions of inserted tryptophans were studied using the polarized time-resolved emission measurements. The fluorescence anisotropy decays of all four tryptophans revealed two classes of correlation times (Table 4). Short correlation times, with values up to few nanoseconds (ϕ_1), likely reflect fast segmental motion of the protein near the tryptophan residue, whereas significantly longer correlation times ($\phi_3 > 44$ ns) likely reflect the overall rotational motion of pCaMKK2-S¹⁰⁰. In the case of the pCaMKK2-S¹⁰⁰ W140 and W267 mutants, 14-3-3 γ noW binding resulted in the appearance of a new correlation time component located around 3.5–5.3 ns (ϕ_2), which could reflect slightly modified internal dynamics of the pCaMKK2-S¹⁰⁰ complex, induced by 14-3-3 γ binding. Changes in the extent of segmental motion were assessed based on the change in the sum of amplitudes of fast anisotropy decay components ($\beta_{\text{fast}} = \beta_1 + \beta_2$) [54]. Similarly to the fluorescence lifetime measurements, small but significant changes in β_{fast} were observed only in mutants containing Trp¹⁴⁰ and Trp⁴⁴⁵, thus suggesting that complex formation increases protein flexibility in regions surrounding these two tryptophan residues.

Therefore, fluorescence lifetime and anisotropy results indicate that 14-3-3 γ binding affects the conformation of CaMKK2 in several regions outside the N-terminal phosphorylated motif, including regions surrounding the Trp¹⁴⁰ within the N-terminal extension and the Trp⁴⁴⁵ within the C-lobe of the kinase domain.

4. Discussion

The main aim of this study was to characterize the interaction between the 14-3-3 protein and CaMKK2. 14-3-3 proteins regulate the function of many enzymes through various mechanisms. For example, serotonin N-acetyltransferase and neutral trehalase Nth1 are activated through 14-3-3 protein-mediated structural modulation of their active sites [42,43]. In the case of phosphorylated tryptophan hydroxylase, 14-3-3 binding slows-down the dephosphorylation of key regulatory phosphosites [55]. Other mechanisms are based on the regulation of sub-cellular localization [56] and on the stabilization of the tertiary and/or quaternary structure of the bound enzyme [57]. Enzymes regulated in a 14-3-3-dependent manner also include many protein kinases [58], although the underlying mechanisms are not fully understood, primarily due to the lack of structural data.

Previous studies on phosphorylated CaMKK1 have shown that the 14-3-3 binding suppresses its catalytic activity [14,15]. Interestingly, enzyme activity measurements revealed that the activity of phosphorylated CaMKK2 is not suppressed but rather weakly enhanced upon complexation with 14-3-3 γ (Fig. 2). This indicates that CaMKK isoforms differ in their 14-3-3-mediated regulations, maybe due to differences in their biochemical properties [6,7].

The SAXS results indicated that the complex formed between 14-3-3 γ and pCaMKK2-S¹⁰⁰ had an elongated and flexible conformation in which the kinase domain of CaMKK appears to directly interact with the 14-3-3 γ dimer surfaces outside its central channel (Figs. 4C,D and 5A,B). The interaction between the kinase domain of pCaMKK2-S¹⁰⁰ and 14-3-3 γ was also indicated by the analysis, in terms of ensemble of conformations (Fig. 5C), which suggested that the 14-3-3 γ :pCaMKK2-S¹⁰⁰ complex is not as extended as the flexible linkers allow. Moreover,

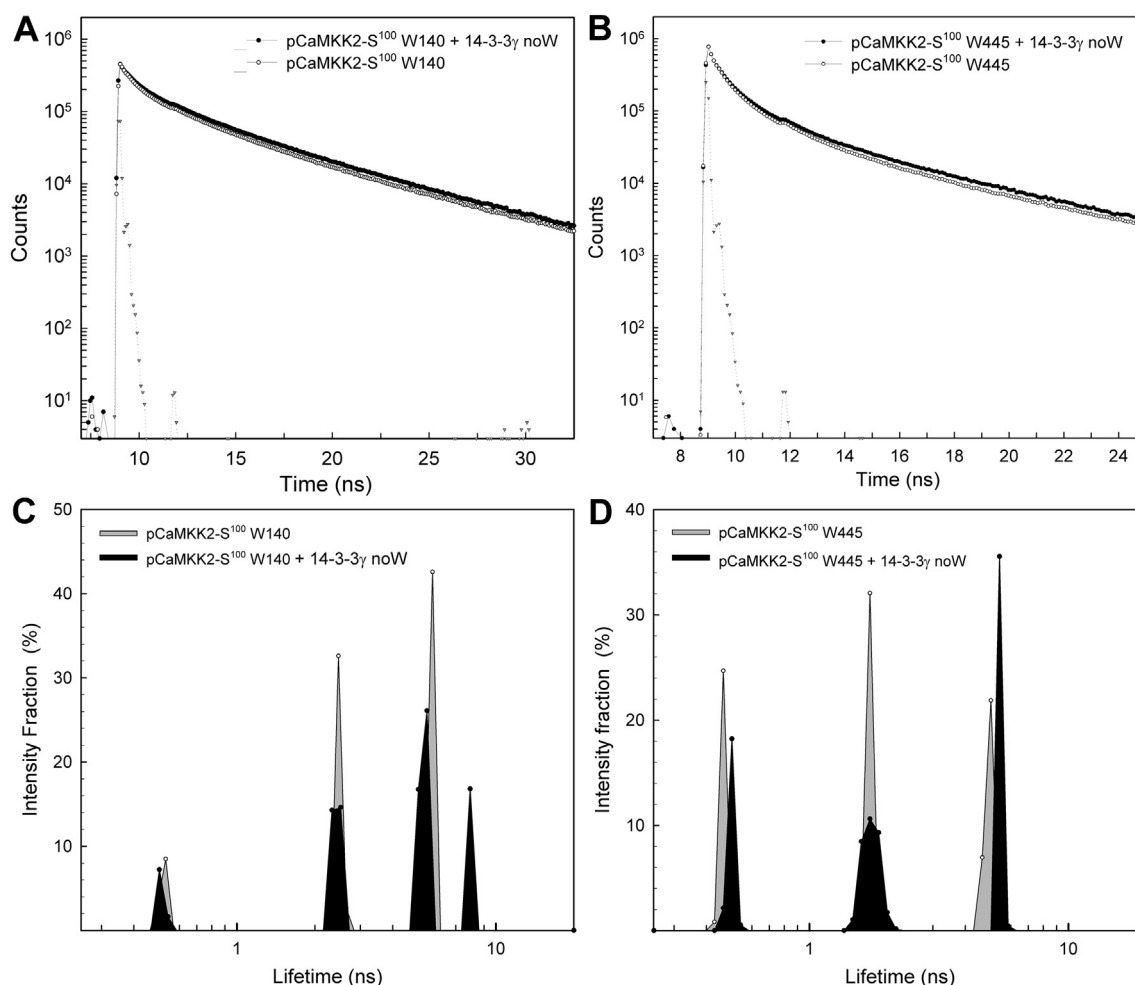


Fig. 7. Time-Resolved Tryptophan Fluorescence Measurements. (A) Normalized fluorescence intensity decays of pCaMKK2-S¹⁰⁰ W140 mutant, in the absence (open circles) and presence (closed circles) of 14-3-3 γ noW. Triangles denote instrument response function. (B) Same as (A) for pCaMKK2-S¹⁰⁰ W445 mutant. (C) Excited state lifetime distribution of pCaMKK2-S¹⁰⁰ W140 in the absence (gray-filled distribution) and presence of 14-3-3 γ noW (black-filled distribution). (D) Same as (C) for pCaMKK2-S¹⁰⁰ W445 mutant.

time-resolved fluorescence measurements of the pCaMKK2-S¹⁰⁰ W445 mutant (Table 4 and Fig. 7) and the binding affinity of pCaMKK2-S¹⁰⁰, which was significantly higher than that of pepS100 phosphopeptide (Figs. 1D and S6), further corroborated the existence of contacts between 14-3-3 γ and the kinase domain of CaMKK2. Although the second 14-3-3 binding motif at the C-terminus of CaMKK2 may not be significantly phosphorylated in vivo [11,12,14], the presence of this motif increased the overall stability of the complex and reduced its conformational flexibility (Figs. 1E and 4D, 6B). This most likely results from the immobilization of the C-terminal extension when the C-terminal motif is anchored to the second ligand binding groove of the 14-3-3 γ dimer. The interaction between 14-3-3 and the kinase domain may be responsible for observed changes in the catalytic activity of CaMKK2 (Fig. 2). We may speculate that the 14-3-3 γ binding affects the conformation of the CaMKK2 active site and/or changes its accessibility. Yet another possibility might be that the 14-3-3 γ binding affects the interaction between the kinase domain and regulatory regions within the N- and C-terminal segments flanking the kinase domain.

CaMKK1 activity is inhibited by Thr¹⁰⁸ phosphorylation (Thr¹⁴⁵ in CaMKK2) [10,13]. In addition, a recent report indicated that the phosphorylation of this residue by AMPK suppresses the autonomous activity of rat CaMKK2 without significant effect on Ca²⁺/CaM-dependent activity [59]. This threonine residue is located in the linker between the N-terminal 14-3-3 binding motif and the kinase domain (Fig. 1A) [10,13]. CaMKK2 also contains, in this region, serine residues

Ser¹²⁹, Ser¹³³, Ser¹³⁷ phosphorylated by cyclin-dependent kinase 5 and by glycogen synthase kinase 3, which are involved in the regulation of CaMKK2 autonomous activity and stability [9]. Time-resolved fluorescence measurements of the pCaMKK2-S¹⁰⁰ W140 mutant showed that 14-3-3 γ binding affects the structure of this region (Table 4 and Fig. 7). Therefore, structural changes in this region and/or its closeness to 14-3-3 may account for the previously reported protection of CaMKK1 Thr¹⁴⁵ against dephosphorylation, which keeps CaMKK1 in the PKA-mediated inhibited state [14]. A similar mechanism may also be involved in the regulation of CaMKK2 as suggested by our observation that the 14-3-3 γ binding slows down the dephosphorylation of pCaMKK2 by PP1 in vitro (Table S1 and Fig. S3). Alternatively, the 14-3-3 binding may inhibit CaMKK activity by affecting CaM binding to the C-terminus of CaMKK. However, fluorescence measurements with dansyl-CaM showed that this interaction is unaffected by 14-3-3 binding to the pCaMKK2:Ca²⁺/CaM complex (Table 3 and Fig. 6).

The crystal structures of complexes between 14-3-3 and the 14-3-3 binding motifs of CaMKK showed that both phosphopeptides interact with the amphipathic groove of 14-3-3 similarly to other 14-3-3 complexes [33,37,40–42]. Nevertheless, in the case of the N-terminal motif, the interaction between the side-chain of Gln at the position +2 relative to pSer¹⁰⁰ and the phosphate group appears to change the direction of the polypeptide chain (Fig. 3B). Interestingly, the superimposition of this structure with that of the ternary complex between the phosphopeptide derived from the C-terminus of plant plasma

membrane H⁺-ATPase, plant 14-3-3C, and fusicoccin (Fig. 3F) [44] showed that the fusicoccin binding cavity stays empty due to the abrupt change in the direction of the C-terminal part of pepS100. Therefore, this protein-protein interaction might be stabilized by small-molecule compounds, as previously reported for other 14-3-3 complexes (reviewed in [60]), which is a potential strategy to inhibit the CaMKK activity.

Transparency document

The <http://dx.doi.org/10.1016/j.bbagen.2018.04.006> associated this article can be found, in online version.

Acknowledgement

We thank Prof. Jaroslav Vecer for dansyl fluorescence data analysis, Dr. Petr Pompach and Dr. Petr Man for mass spectrometry analyses and Dr. Carlos V. Melo for proofreading the article.

Funding sources

This work was supported by the Czech Science Foundation (grant number 16-02739S), the Czech Academy of Sciences (Research Projects RVO: 67985823 of the Institute of Physiology), EU supported projects BIOCEV (CZ.1.05/1.1.00.02.0109) and Operational Programme “Research and Development for Innovation” (no. CZ.1.05/4.1.00/16.0340), Czech Infrastructure for Integrative Structural Biology (CIISB) project LM2015043, funded by MEYS CR, and by the H2020 Marie Curie Actions of the European Commission through the TASPPI project, Grant Agreement 675179.

Data deposition

The atomic coordinates and structure factors have been deposited in the Protein Data Bank, www.wwpdb.org (PDB ID codes 6EWW and 6FEL).

Author contributions

V.O. and T.O. designed research; K.P., O.P., S.K., D.K., D.L.S., P.H., and T.O. performed research; K.P., S.K., O.P., P.H., V.O., and T.O. analyzed data; and V.O. and T.O. wrote the paper.

Conflict of interest

The authors declare no conflict of interest.

Appendix A. Supplementary data

Supplementary data to this article can be found online at <https://doi.org/10.1016/j.bbagen.2018.04.006>.

References

- [1] B. Haribabu, S.S. Hook, M.A. Selbert, E.G. Goldstein, E.D. Tomhave, A.M. Edelman, R. Snyderman, A.R. Means, Human calcium-calmodulin dependent protein kinase I: cDNA cloning, domain structure and activation by phosphorylation at threonine-177 by calcium-calmodulin dependent protein kinase I kinase, *EMBO J.* 14 (1995) 3679–3686.
- [2] R.L. Hurley, K.A. Anderson, J.M. Franzone, B.E. Kemp, A.R. Means, L.A. Witters, The Ca²⁺/calmodulin-dependent protein kinase kinases are AMP-activated protein kinase kinases, *J. Biol. Chem.* 280 (2005) 29060–29066.
- [3] K.A. Anderson, T.J. Ribar, F. Lin, P.K. Noeldner, M.F. Green, M.J. Muehlbauer, L.A. Witters, B.E. Kemp, A.R. Means, Hypothalamic CaMKK2 contributes to the regulation of energy balance, *Cell Metab.* 7 (2008) 377–388.
- [4] L. Racioppi, A.R. Means, Calcium/calmodulin-dependent protein kinase kinase 2: roles in signaling and pathophysiology, *J. Biol. Chem.* 287 (2012) 31658–31665.
- [5] H. Tokumitsu, T.R. Soderling, Requirements for calcium and calmodulin in the calmodulin kinase activation cascade, *J. Biol. Chem.* 271 (1996) 5617–5622.
- [6] H. Tokumitsu, M. Muramatsu, M. Ikura, R. Kobayashi, Regulatory mechanism of Ca²⁺/calmodulin-dependent protein kinase kinase, *J. Biol. Chem.* 275 (2000) 20090–20095.
- [7] K.A. Anderson, R.L. Means, Q.H. Huang, B.E. Kemp, E.G. Goldstein, M.A. Selbert, A.M. Edelman, R.T. Freneau, A.R. Means, Components of a calmodulin-dependent protein kinase cascade. Molecular cloning, functional characterization and cellular localization of Ca²⁺/calmodulin-dependent protein kinase kinase beta, *J. Biol. Chem.* 273 (1998) 31880–31889.
- [8] H. Tokumitsu, M. Iwabu, Y. Ishikawa, R. Kobayashi, Differential regulatory mechanism of Ca²⁺/calmodulin-dependent protein kinase kinase isoforms, *Biochemistry* 40 (2001) 13925–13932.
- [9] M.F. Green, J.W. Scott, R. Steel, J.S. Oakhill, B.E. Kemp, A.R. Means, Ca²⁺/calmodulin-dependent protein kinase kinase beta is regulated by multisite phosphorylation, *J. Biol. Chem.* 286 (2011) 28066–28079.
- [10] G.A. Wayman, H. Tokumitsu, T.R. Soderling, Inhibitory cross-talk by cAMP kinase on the calmodulin-dependent protein kinase cascade, *J. Biol. Chem.* 272 (1997) 16073–16076.
- [11] M. Matsushita, A.C. Nairn, Inhibition of the Ca²⁺/calmodulin-dependent protein kinase I cascade by cAMP-dependent protein kinase, *J. Biol. Chem.* 274 (1999) 10086–10093.
- [12] S. Okuno, T. Kitani, H. Fujisawa, Regulation of Ca(2+)/calmodulin-dependent protein kinase kinase alpha by cAMP-dependent protein kinase: I. Biochemical analysis, *J. Biochem.* 130 (2001) 503–513.
- [13] T. Kitani, S. Okuno, H. Fujisawa, Regulation of ca(2+)/calmodulin-dependent protein kinase kinase alpha by cAMP-dependent protein kinase: II. Mutational analysis, *J. Biochem.* 130 (2001) 515–525.
- [14] M.A. Davare, T. Saneyoshi, E.S. Guire, S.C. Nygaard, T.R. Soderling, Inhibition of calcium/calmodulin-dependent protein kinase kinase by protein 14-3-3, *J. Biol. Chem.* 279 (2004) 52191–52199.
- [15] T. Ichimura, M. Taoka, Y. Hozumi, K. Goto, H. Tokumitsu, 14-3-3 proteins directly regulate Ca(2+)/calmodulin-dependent protein kinase kinase alpha through phosphorylation-dependent multisite binding, *FEBS Lett.* 582 (2008) 661–665.
- [16] A.J. Muslin, J.W. Tanner, P.M. Allen, A.S. Shaw, Interaction of 14-3-3 with signaling proteins is mediated by the recognition of phosphoserine, *Cell* 84 (1996) 889–897.
- [17] N.N. Sluchanko, N.B. Gusev, Moonlighting chaperone-like activity of the universal regulatory 14-3-3 proteins, *FEBS J.* 284 (2017) 1279–1295.
- [18] T. Obsil, V. Obsilova, Structural basis of 14-3-3 protein functions, *Semin. Cell Dev. Biol.* 22 (2011) 663–672.
- [19] F.H. Niesen, H. Berglund, M. Vedadi, The use of differential scanning fluorimetry to detect ligand interactions that promote protein stability, *Nat. Protoc.* 2 (2007) 2212–2221.
- [20] V. Obsilova, P. Herman, J. Vecer, M. Sulc, J. Teisinger, T. Obsil, 14-3-3zeta C-terminal stretch changes its conformation upon ligand binding and phosphorylation at Thr232, *J. Biol. Chem.* 279 (2004) 4531–4540.
- [21] B. Holakovska, L. Grycova, J. Bily, J. Teisinger, Characterization of calmodulin binding domains in TRPV2 and TRPV5 C-tails, *Amino Acids* 40 (2011) 741–748.
- [22] O. Petrvalska, D. Kosek, Z. Kukacka, Z. Tosner, P. Man, J. Vecer, P. Herman, V. Obsilova, T. Obsil, Structural insight into the 14-3-3 protein-dependent inhibition of protein kinase ASK1 (apoptosis signal-regulating kinase 1), *J. Biol. Chem.* 291 (2016) 20753–20765.
- [23] L. Rezabkova, P. Man, P. Novak, P. Herman, J. Vecer, V. Obsilova, T. Obsil, Structural basis for the 14-3-3 protein-dependent inhibition of the regulator of G protein signaling 3 (RGS3) function, *J. Biol. Chem.* 286 (2011) 43527–43536.
- [24] D.I. Svergun, Determination of the regularization parameter in indirect-transform methods using perceptual criteria, *J. Appl. Crystallogr.* 25 (1992) 495–503.
- [25] M.V. Petoukhov, D. Franke, A.V. Shkumatov, G. Tria, A.G. Kikhney, M. Gajda, C. Gorba, H.D. Mertens, P.V. Konarev, D.I. Svergun, New developments in the program package for small-angle scattering data analysis, *J. Appl. Crystallogr.* 45 (2012) 342–350.
- [26] P.V. Konarev, V.V. Volkov, A.V. Sokolova, M.H.J. Koch, D.I. Svergun, PRIMUS: a windows PC-based system for small-angle scattering data analysis, *J. Appl. Crystallogr.* 36 (2003) 1277–1282.
- [27] D.I. Svergun, Restoring low resolution structure of biological macromolecules from solution scattering using simulated annealing, *Biophys. J.* 76 (1999) 2879–2886.
- [28] G. Tria, H.D. Mertens, M. Kachala, D.I. Svergun, Advanced ensemble modelling of flexible macromolecules using X-ray solution scattering, *IUCr J.* 2 (2015) 207–217.
- [29] D. Kosek, S. Kylarova, K. Psenakova, L. Rezabkova, P. Herman, J. Vecer, V. Obsilova, T. Obsil, Biophysical and structural characterization of the thioredoxin-binding domain of protein kinase ASK1 and its interaction with reduced thioredoxin, *J. Biol. Chem.* 289 (2014) 24463–24474.
- [30] W. Kabsch, Xds, *Acta Crystallogr D Biol Crystallogr.* 66 (2010), pp. 125–132.
- [31] K.M. Sparta, M. Krug, U. Heinemann, U. Mueller, M.S. Weiss, Xdsapp2.0, *J. Appl. Crystallogr.* 49 (2016) 1085–1092.
- [32] A. Vagin, A. Teplyakov, MOLREP: an automated program for molecular replacement, *J. Appl. Crystallogr.* 30 (1997) 1022–1025.
- [33] M. Molzan, C. Ottmann, Synergistic binding of the phosphorylated S233- and S259-binding sites of C-Raf to one 14-3-3zeta dimer, *J. Mol. Biol.* 423 (2012) 486–495.
- [34] P.D. Adams, P.V. Afonine, G. Bunkoczi, V.B. Chen, I.W. Davis, N. Echols, J.J. Headd, L.W. Hung, G.J. Kapral, R.W. Grosse-Kunstleve, A.J. McCoy, N.W. Moriarty, R. Oeffner, R.J. Read, D.C. Richardson, J.S. Richardson, T.C. Terwilliger, P.H. Zwart, PHENIX: a comprehensive python-based system for macromolecular structure solution, *Acta Crystallogr. D Biol. Crystallogr.* 66 (2010) 213–221.
- [35] M. Kukimoto-Niino, S. Yoshikawa, T. Takagi, N. Ohsawa, Y. Tomabechi, T. Terada, M. Shirouzu, A. Suzuki, S. Lee, T. Yamauchi, M. Okada-Iwabu, M. Iwabu, T. Kadowaki, Y. Minokoshi, S. Yokoyama, Crystal structure of the ca(2)

- (+)/calmodulin-dependent protein kinase kinase in complex with the inhibitor STO-609, *J. Biol. Chem.* 286 (2011) 22570–22579.
- [36] M.B. Yaffe, K. Rittinger, S. Volinia, P.R. Caron, A. Aitken, H. Leffers, S.J. Gamblin, S.J. Smerdon, L.C. Cantley, The structural basis for 14-3-3: phosphopeptide binding specificity, *Cell* 91 (1997) 961–971.
- [37] K. Rittinger, J. Budman, J. Xu, S. Volinia, L.C. Cantley, S.J. Smerdon, S.J. Gamblin, M.B. Yaffe, Structural analysis of 14-3-3 phosphopeptide complexes identifies a dual role for the nuclear export signal of 14-3-3 in ligand binding, *Mol. Cell* 4 (1999) 153–166.
- [38] C. Johnson, S. Crowther, M.J. Stafford, D.G. Campbell, R. Toth, C. MacKintosh, Bioinformatic and experimental survey of 14-3-3-binding sites, *Biochem. J.* 427 (2010) 69–78.
- [39] J. Silhan, V. Obsilova, J. Vecer, P. Herman, M. Sulc, J. Teisinger, T. Obsil, 14-3-3 protein C-terminal stretch occupies ligand binding groove and is displaced by phosphopeptide binding, *J. Biol. Chem.* 279 (2004) 49113–49119.
- [40] R. Rose, M. Rose, C. Ottmann, Identification and structural characterization of two 14-3-3 binding sites in the human peptidylarginine deiminase type VI, *J. Struct. Biol.* 180 (2012) 65–72.
- [41] N.N. Sluchanko, S. Beelen, A.A. Kulikova, S.D. Weeks, A.A. Antson, N.B. Gusev, S.V. Strelkov, Structural basis for the interaction of a human small heat shock protein with the 14-3-3 universal signaling regulator, *Structure* 25 (2017) 305–316.
- [42] M. Alblova, A. Smidova, V. Docekal, J. Vesely, P. Herman, V. Obsilova, T. Obsil, Molecular basis of the 14-3-3 protein-dependent activation of yeast neutral trehalase Nth1, *Proc. Natl. Acad. Sci. U. S. A.* 114 (2017) E9811–E9820.
- [43] T. Obsil, R. Ghirlando, D.C. Klein, S. Ganguly, F. Dyda, Crystal structure of the 14-3-3 zeta: serotonin N-acetyltransferase complex. A role for scaffolding in enzyme regulation, *Cell* 105 (2001) 257–267.
- [44] M. Wurttele, C. Jelic-Ottmann, A. Wittinghofer, C. Oecking, Structural view of a fungal toxin acting on a 14-3-3 regulatory complex, *EMBO J.* 22 (2003) 987–994.
- [45] M. Kacirova, J. Novacek, P. Man, V. Obsilova, T. Obsil, Structural basis for the 14-3-3 protein-dependent inhibition of Phosducin function, *Biophys. J.* 112 (2017) 1339–1349.
- [46] D.M. Bustos, The role of protein disorder in the 14-3-3 interaction network, *Mol. Biosyst.* 8 (2012) 178–184.
- [47] T. Ishida, K. Kinoshita, PrDOS: prediction of disordered protein regions from amino acid sequence, *Nucleic Acids Res.* 35 (2007) W460–464.
- [48] Z. Dosztanyi, V. Csizmok, P. Tompa, I. Simon, IUPred: web server for the prediction of intrinsically unstructured regions of proteins based on estimated energy content, *Bioinformatics* 21 (2005) 3433–3434.
- [49] V. Receveur-Brechot, D. Durand, How random are intrinsically disordered proteins? A small angle scattering perspective, *Curr. Protein Pept. Sci.* 13 (2012) 55–75.
- [50] R.P. Rambo, Resolving individual components in protein-RNA complexes using small-angle X-ray scattering experiments, *Methods Enzymol.* 558 (2015) 363–390.
- [51] R.L. Kincaid, M. Vaughan, J.C. Osborne Jr., V.A. Tkachuk, Ca²⁺ – dependent interaction of 5-dimethylaminonaphthalene-1-sulfonyl-calmodulin with cyclic nucleotide phosphodiesterase, calcineurin, and troponin I, *J. Biol. Chem.* 257 (1982) 10638–10643.
- [52] L. Rezabkova, E. Boura, P. Herman, J. Vecer, L. Bourova, M. Sulc, P. Svoboda, V. Obsilova, T. Obsil, 14-3-3 protein interacts with and affects the structure of RGS domain of regulator of G protein signaling 3 (RGS3), *J. Struct. Biol.* 170 (2010) 451–461.
- [53] P. Herman, J.C. Lee, The advantage of global fitting of data involving complex linked reactions, in: A.W.W. Fenton (Ed.), *Allostery: Methods and Protocols*, vol. 796, Humana Press Inc., New York, 2012, pp. 399–421.
- [54] L. Rezabkova, M. Kacirova, M. Sulc, P. Herman, J. Vecer, M. Stepanek, V. Obsilova, T. Obsil, Structural modulation of phosducin by phosphorylation and 14-3-3 protein binding, *Biophys. J.* 103 (2012) 1960–1969.
- [55] U. Banik, G.A. Wang, P.D. Wagner, S. Kaufman, Interaction of phosphorylated tryptophan hydroxylase with 14-3-3 proteins, *J. Biol. Chem.* 272 (1997) 26219–26225.
- [56] A. Kumagai, W.G. Dunphy, Binding of 14-3-3 proteins and nuclear export control the intracellular localization of the mitotic inducer Cdc25, *Genes Dev.* 13 (1999) 1067–1072.
- [57] C. Ottmann, S. Marco, N. Jaspert, C. Marcon, N. Schauer, M. Weyand, C. Vandermeeren, G. Duby, M. Boutry, A. Wittinghofer, J.L. Rigaud, C. Oecking, Structure of a 14-3-3 coordinated hexamer of the plant plasma membrane H⁺ -ATPase by combining X-ray crystallography and electron cryomicroscopy, *Mol. Cell* 25 (2007) 427–440.
- [58] M. Tinti, F. Madeira, G. Murugesan, G. Hoxhaj, R. Toth, C. Mackintosh, ANIA: ANnotation and integrated analysis of the 14-3-3 interactome, *Database (Oxford)* 2014 (2014) bat085, <http://dx.doi.org/10.1093/database/bat085>.
- [59] A. Nakanishi, N. Hatano, Y. Fujiwara, A. Sha'ri, S. Takabatake, H. Akano, N. Kanayama, M. Magari, N. Nozaki, H. Tokumitsu, AMP-activated protein kinase-mediated feedback phosphorylation controls the Ca(2+)/calmodulin (CaM) dependence of Ca(2+)/CaM-dependent protein kinase kinase beta, *J. Biol. Chem.* 292 (1980) 19804–19813.
- [60] L.M. Stevers, E. Sijbesma, M. Botta, C. MacKintosh, T. Obsil, I. Landrieu, Y. Cau, A.J. Wilson, A. Karawajczyk, J. Eickhoff, J. Davis, M. Hann, R.G. Mahony, L. Doveston, C. Ottmann Brunsvel, Modulators of 14-3-3 protein-protein interactions, *J. Med. Chem.* (2017 Oct. 19), <http://dx.doi.org/10.1021/acs.jmedchem.7b00574> (Epub ahead of print).

Table S1

Dephosphorylation of CaMKK2 at pThr¹⁴⁵ and pSer⁴⁹⁵ by PP1 in the presence and absence of 14-3-3 γ .

Site	peptide form	m/z (charge)	Dephosphorylation time (min)					
			pCaMKK2			pCaMKK2 + 14-3-3 γ		
			0	1.5	7	0	1.5	7
Thr145^a	P	695,9556 (5+)	2.5E+07	2.8E+07	2.2E+07	2.0E+07	4.0E+07	1.6E+07
	not-P	679,9625 (5+)	1.3E+07	3.3E+07	3.7E+07	1.3E+07	1.3E+07	3.2E+07
	ratio non-P/P^c		0.52	1.2	1.7	0.65	0.33	2.0
Ser495^b	P	570,2900 (5+)	2.3E+07	2.5E+07	5.4E+06	1.8E+06	4.0E+06	4.2E+06
	not-P	554,2970 (5+)	0.0E+00	2.9E+06	6.2E+06	0.0E+00	0.0E+00	0.0E+00
	ratio non-P/P		0	0.12	1.1	0	0	0

^aPeptide sequence PSLPYSPVSSPQSSPRLPRRPT¹⁴⁵VESHHSIT

^bPeptide sequence VKTMIRKRS⁴⁹⁵FGNPFEGSRREERS

^cPhosphorylated CaMKK2₉₃₋₅₁₇ D³³⁰A (kinase dead mutant) in the presence and absence of 14-3-3 γ was dephosphorylated by protein phosphatase 1 (PP1, catalytic subunit α -isoform from rabbit). Dephosphorylation by PP1 (Sigma-Aldrich, USA) with a specific activity 5,000 units/mg) was performed at 30 °C in buffer containing 50 mM HEPES (pH 7.5), 100 mM NaCl, 2 mM DTT, 1 mM MnCl₂, and 0.01% NP-40. The reaction mixture contained 11 μ M CaMKK2 D³³⁰A, 34 μ M 14-3-3 γ (where needed) and PP1 in an optimized molar ratio of 1:250 (enzyme/substrate). Reactions were stopped after 0, 1.5 and 7 min by adding 100 mM β -glycerolphosphate (Sigma-Aldrich, USA) and immediate freezing in liquid nitrogen. Analysis was started by an online digestion of sample solution containing 64 pmol of CaMKK2 on a pepsin column (66 μ L bed volume, flow rate 100 μ L.min⁻¹, 3 min). Generated peptides were trapped and desalted online on a Peptide microtrap column (Optimize Technologies, Oregon City, OR) and separated on a C18 reversed phase column (ZORBAX 300SB-C18 3.5 μ m, 0.5 \times 35 mm, Agilent, Santa Clara, CA) using a linear gradient 10–45% B in 40 min, where solvent A was 2% acetonitrile/0.4% formic acid in water, solvent B 95% acetonitrile/5% water/0.4% formic acid. The column was interfaced with the ESI source of a 15T FT-ICR mass spectrometer (Solarix XR, Bruker Daltonics, Bremen, Germany) operating in MS/MS mode. Peptides were identified by a MASCOT search against a database containing the sequence of human CaMKK2. Intensities of extracted ion chromatograms of first monoisotopes of phosphorylated (P) and non-phosphorylated (not-P) peptides were used to calculate ratios between non-phosphorylated and phosphorylated forms.

```

CAMKK1      1  ---MEGGA VCCQDPRAELVERVA AIDVTHLEADGGPEETRNGVDPPPRARAASVIP 55
CAMKK2      1  MSSCVSSQPSSNRRAAPQDELGGRGSSSSSESQKPCEALRGLSSLSIHLMESFIVVTECEP 60
          :.. *: *: ** * : : : ** * .. : . :.. *

CAMKK1     56  GSTSRLLPAR-----PSSLRKLSLQERPA-----SY 83
CAMKK2     61  GCAVDLGLADRPLEADGQEVPLDTSGSQARPHLSRKLSLQERSQGGLAAGGSIDMNGR 120
          *: * ** : ** :*****: *

CAMKK1     84  LEAQAGPYATGEASHISPRAWRRPTIESHHVAISDAEDCVQLNQYKQSEIGKGAYGVVR 143
CAMKK2    121  CTCPSPYPSEVSSPQSSPRLPRPTVESHHVSI TGMQDCVQLNQYTLKDEIGKGSYGVK 180
          . : **: . : : : *** *****:***:*. :*****:***:

CAMKK1    144  LAYNESEDRHYAMKVLSSKKLLKQYGFRRPPPRGSQAQGGPAKQLLEPLERVYQEIAIL 203
CAMKK2    181  LAYNENDNTYYAMKVLSSKKLLRQAGFRRPPPRGTRAPGGCIQPRGPIEQVYQEIAIL 240
          *****: : :*****:***:*****:*. * * : * :*****:

CAMKK1    204  KKLDHVN VVKLIEVLDDPAEDNLYLVFDLLRKGPVMEVPCKPFSEEQARLYLRDVILGL 263
CAMKK2    241  KKLDHNPV VVKLIEVLDDPNEDHLYMVFELV NQGPVMEVPTLKLPLSEDAQRFYQDLIKGI 300
          ***** *****:***** *:***:***:*. :***** * :*:***:***:***:

CAMKK1    264  EYLHCQKIVHRDIKPSNLLLGDDGHVKIADFGVSNQFEGNDAQLSSTAGTPAFMAPEAIS 323
CAMKK2    301  EYLHYQKI IHRDIKPSNLLVGEDGHKIADFGVSNFKGSDALLSNVTGTPAFMAPESLS 360
          ***** *:*****:*.***:*****:*.*** * * :*****:*.

CAMKK1    324  DSGQSFSGKALDVWATGVTLYCFVYGKCPFIDDFILALHRKIKNEVVFPEEPEISEELK 383
CAMKK2    361  ETRKIFSGKALDVWAMGVTLYCFVFGQCPFMDERIMCLHSKIKSQALEFPDQPDIAEDLK 420
          : : :***** *****:***:***: * :* * * : : * :*:***:

CAMKK1    384  DLILKMLDKNPETRIGVPDIKLHPWVTKNGEELPSEEEHCSVVEVTEEEVKNSVRLIPS 443
CAMKK2    421  DLITRMLDKNPESRIVVPEIKLHPVTRHGAELPSEDENCTLVEVTEEEVENSVKHIPS 480
          *** :*****:*** *:*****:*. *****:*. :*****:***: ***

CAMKK1    444  WTVILVKSMLRKRSFGNPFEPQARREERSMSAFGNLLVKEGFGEGGKSPPELPGVQEDFA 503
CAMKK2    481  LATVILVKTMIKRKRSFGNPFEGSRREERSLSAFGNLLVKKPTRECELSSELKEARQRQ 539
          :*****:*.*****: *****:*****: * . * * : : .

CAMKK1    504  AS----- 505
CAMKK2    540  PFGHRPAPRGGGSALVRGSPCVESCWAPAGSPARMHPLRPEEAMEPE 588
          ..

```

Figure S1. Related to Figure 1A.

Sequence alignment of human CaMKK1 (Q8N5S9) and CaMKK2 (Q96RR4). PKA phosphorylation sites are indicated by red circles. The 14-3-3 binding motifs are indicated by red squares. See also Figure 1A.

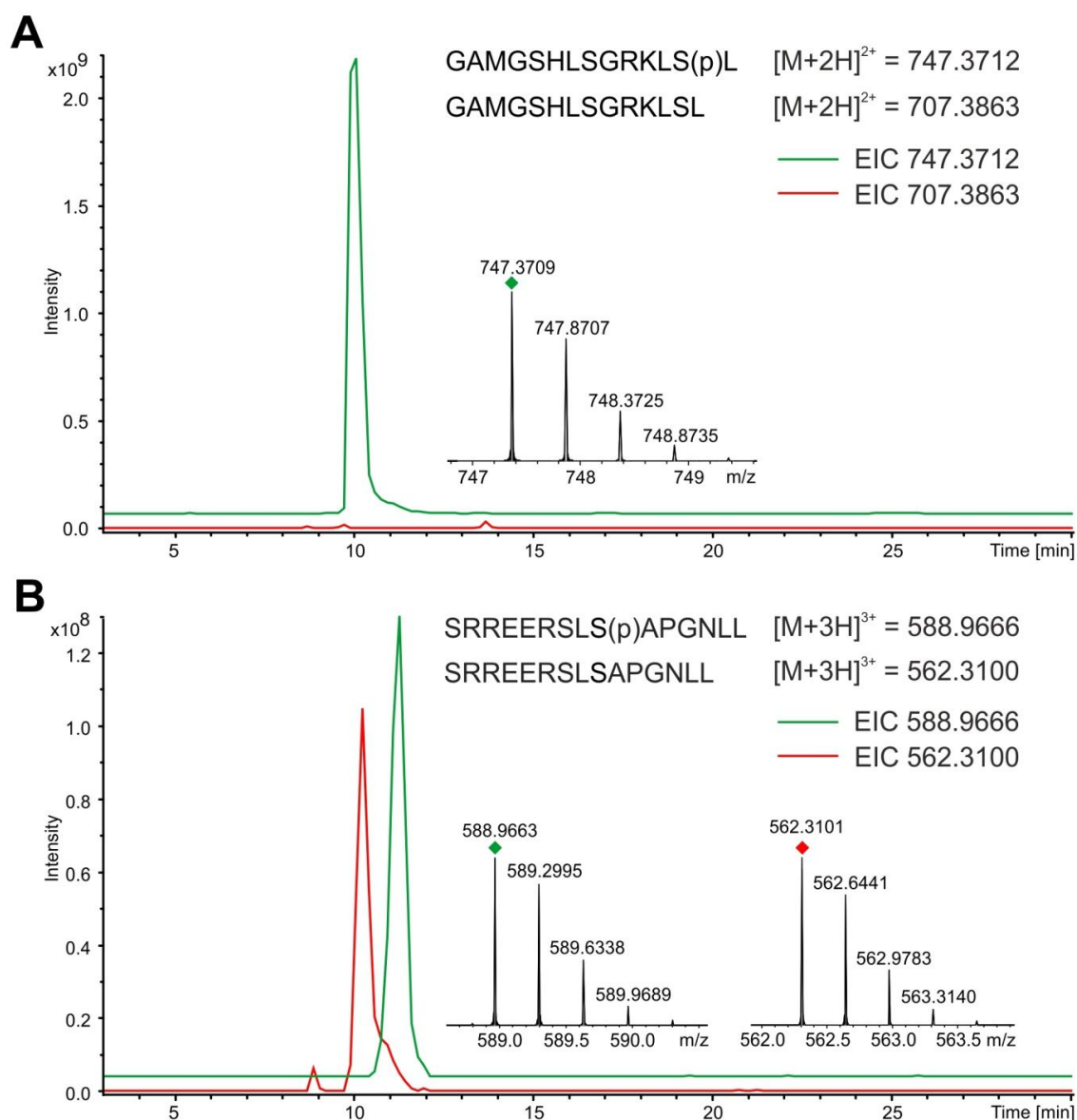


Figure S2. Related to Figure 1.

Detection of CaMKK-S^{100,511} phosphorylated peptides by FT-ICR mass spectrometry. (A) Extract ion chromatogram (EIC) of phosphorylated GAMGSHLSGRKLS¹⁰⁰L peptide shown in green, observed at m/z 747.3709 (2+). The red line represents the EIC of the non-phosphorylated form of the same peptide observed at m/z 707.3863 (2+). The inset shows the zoomed, high-resolution MS spectrum of phosphorylated GAMGSHLSGRKLS¹⁰⁰L. (B) Extract ion chromatograms of the phosphorylated SRREERSLS⁵¹¹APGNLL peptide shown in green, observed at m/z 588.9663 (3+), and of non-phosphorylated form, observed at m/z 562.3101 (3+), which is shown in red. The inset shows the zoomed, high-resolution MS spectra of phosphorylated and non-phosphorylated SRREERSLS⁵¹¹APGNLL peptides. The phosphorylation sites in both peptides were determined based on the collision-induced dissociation spectra. See also Figure S1A.

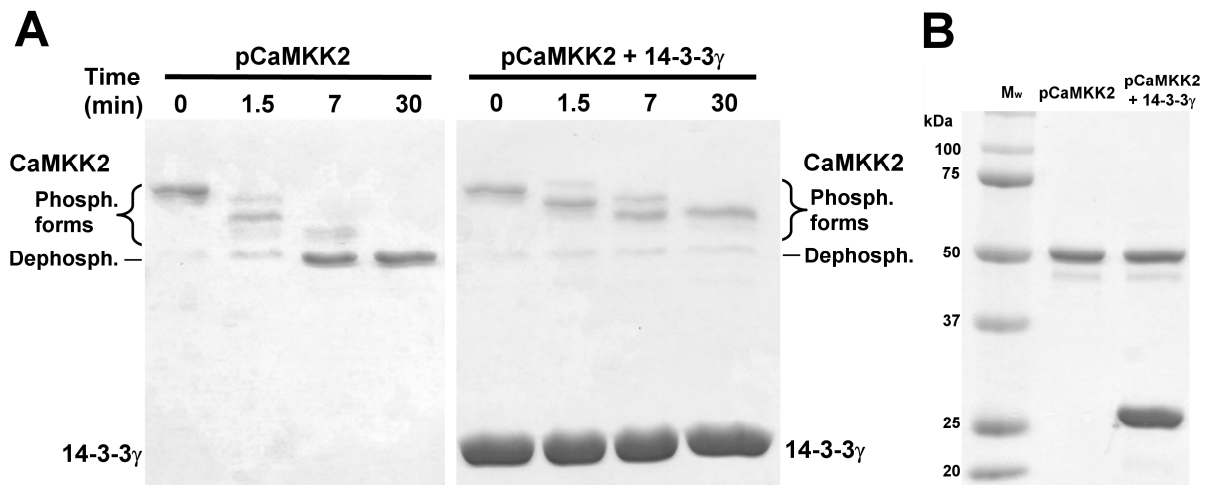


Figure S3. Related to Figure 2.

14-3-3 γ Binding Slows Down Dephosphorylation of CaMKK2. (A) Phosphorylated CaMKK2₉₃₋₅₁₇ D³³⁰A (kinase dead mutant) in the presence and absence of 14-3-3 γ was dephosphorylated by type 1 protein phosphatase (PP1, catalytic subunit α -isoform from rabbit). Dephosphorylation by PP1 (Sigma-Aldrich, USA) with a specific activity 5,000 units/mg) was performed at 30 °C in buffer containing 50 mM HEPES (pH 7.5), 100 mM NaCl, 2 mM DTT, 1 mM MnCl₂, and 0.01% NP-40. The reaction mixture contained 11 μ M CaMKK2 D³³⁰A, 34 μ M 14-3-3 γ (where needed) and PP1 in an optimized molar ratio of 1:250 (enzyme/substrate). Reactions were stopped after 0, 1.5 and 7 min by adding 100 mM β -glycerolphosphate (Sigma-Aldrich, USA), mixing with SDS reducing sample buffer and boiling for 5 min. Sample analysis was performed using 12% Phos-tag SDS-PAGE with 50 μ M Phos-tag (FUJIFILM Wako Pure Chemical Corp., Japan). (B) Samples used in (A) resolved on 12% SDS-PAGE. See also Figure 2.

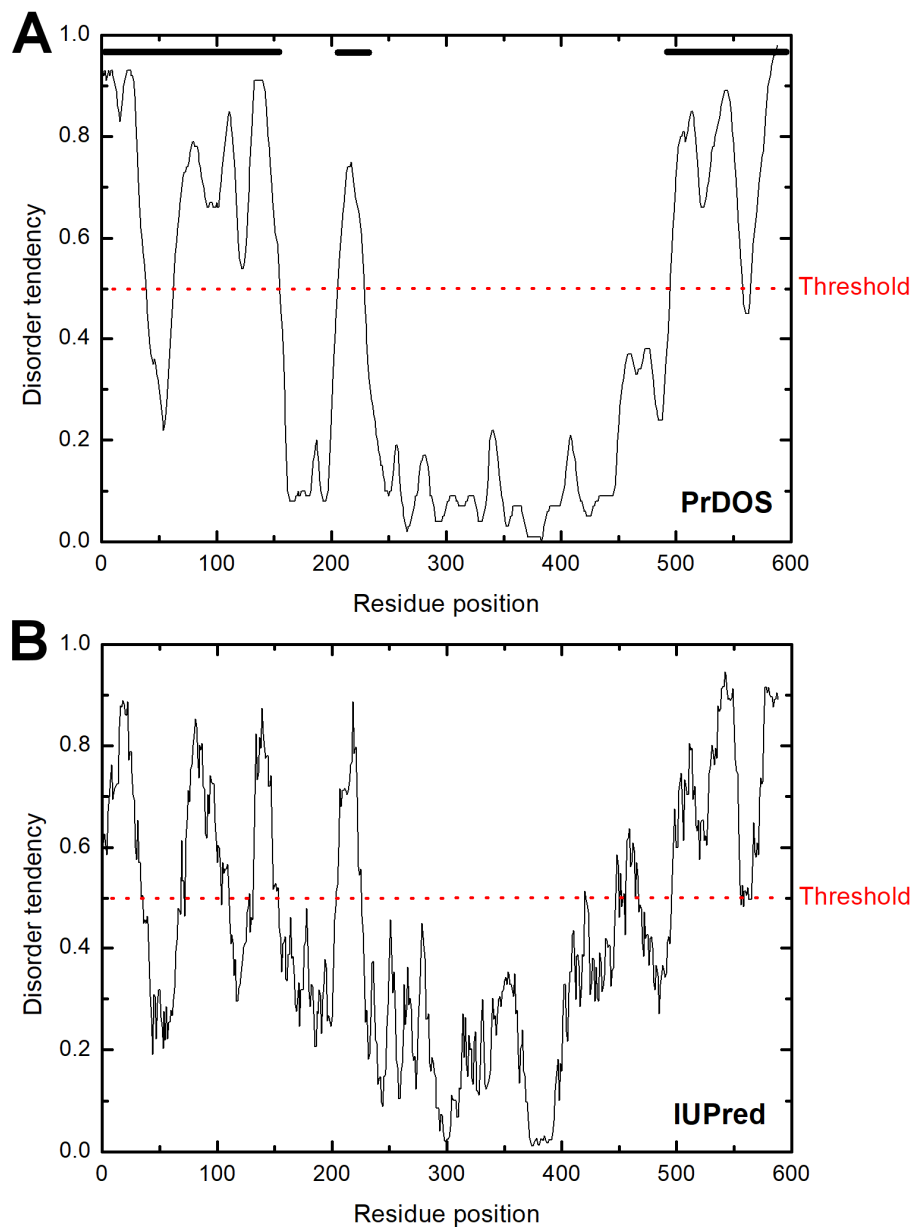


Figure S4. Related to Figure 4D.

Bioinformatics analysis of CaMKK2. Disorder prediction using PrDOS (A) (Ishida and Kinoshita, 2007) and IUPred (B) (Dosztanyi et al., 2005) predictors suggests that both the N-terminal (residues 1-125) and the C-terminal (residues 500-588) tails of CaMKK2 are unstructured. See also Figure 4D.

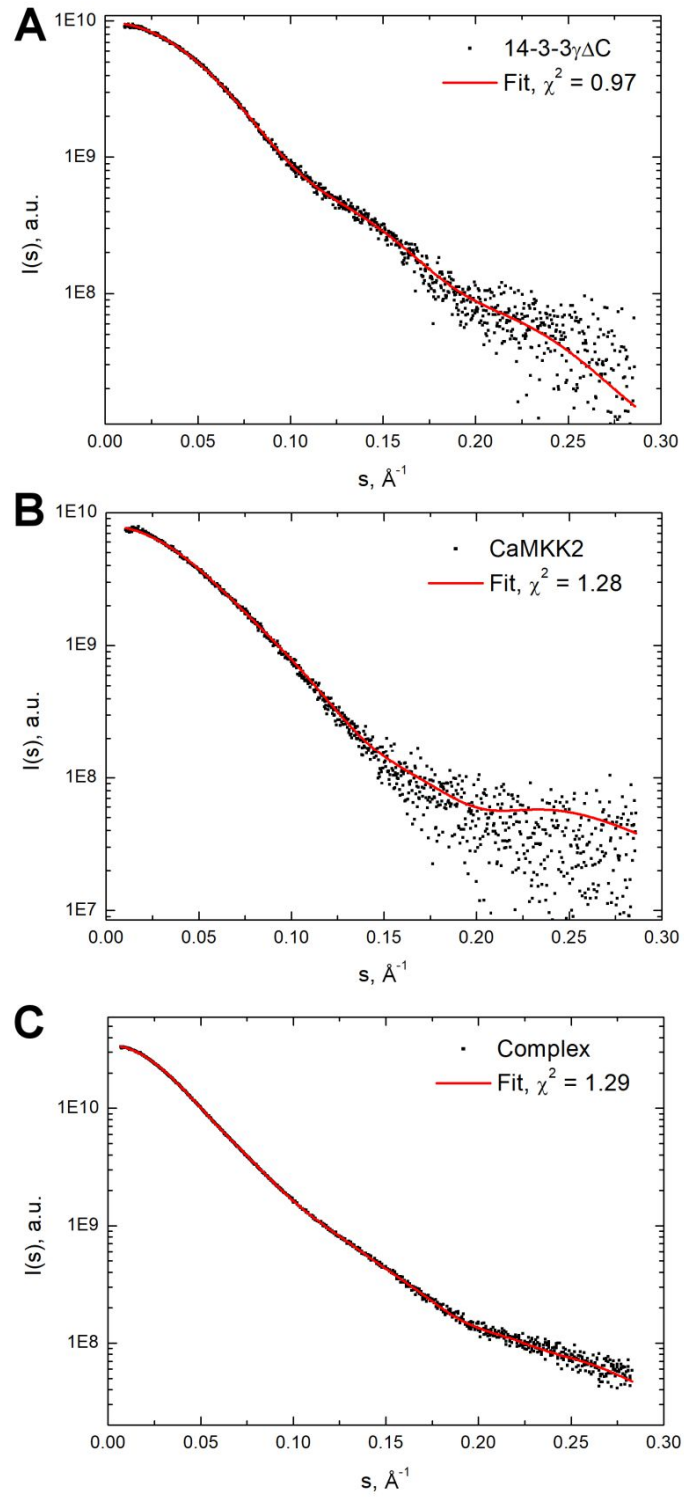


Figure S5. Related to Figure 5A.

Ab initio shape reconstruction of the pCaMKK2-S¹⁰⁰:14-3-3 γ complex using MONSA. Fits of the simulated scattering curves versus the experimental SAXS data of 14-3-3 $\gamma\Delta$ C (A), CaMKK2-S¹⁰⁰ (B) and the 14-3-3 $\gamma\Delta$ C:pCaMKK2-S¹⁰⁰ (2:1) complex (C). See also Figure 5A.

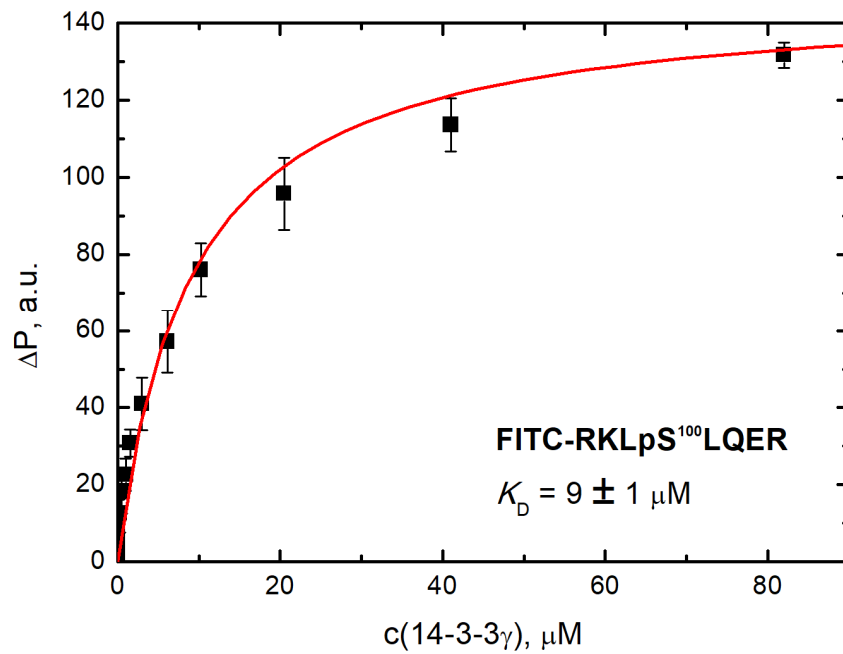


Figure S6. Related to Figures 1D and 5.

Binding isotherm of the synthetic peptide containing the N-terminal 14-3-3 binding motif of CaMKK2. Results are expressed as the mean \pm SD of three experiments. See also Figures 1D and 5.

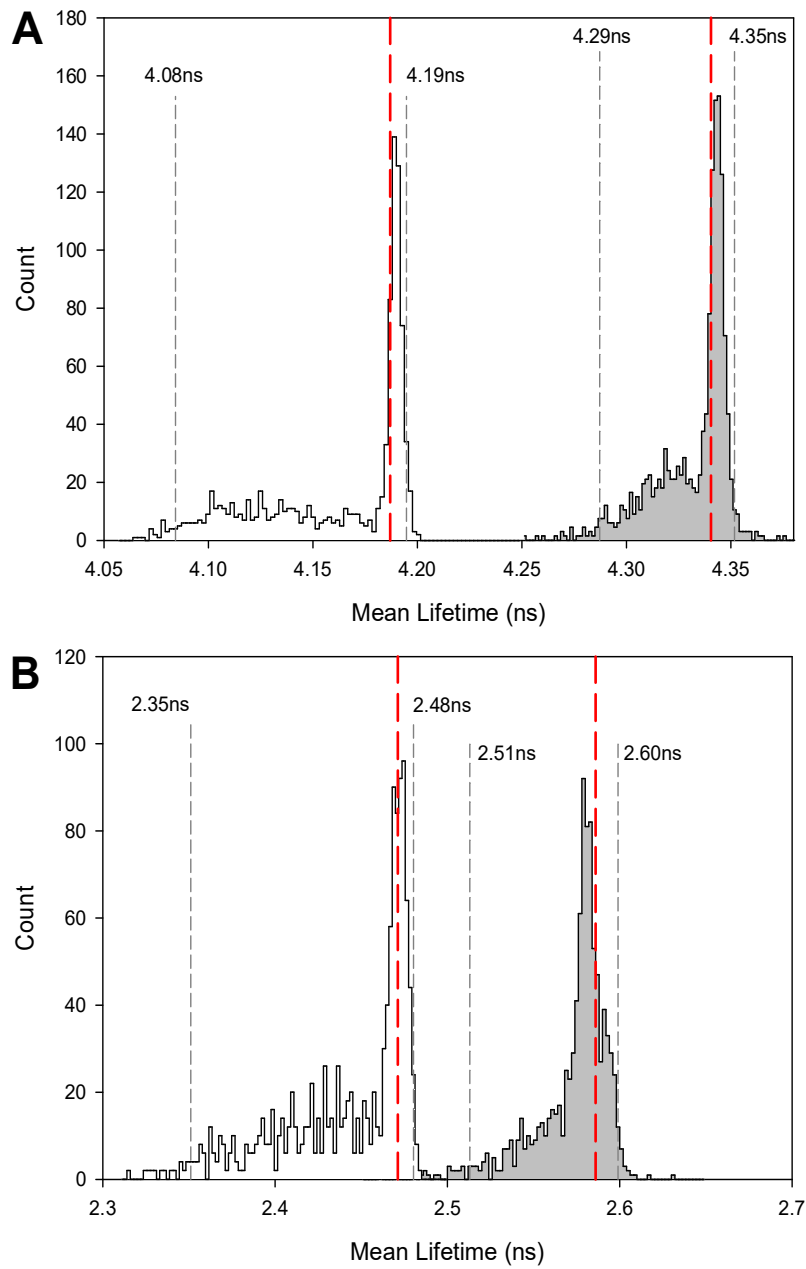


Figure S7. Related to Table 4 and Figure 7.

Statistical significance of observed differences in mean fluorescence lifetimes. Rigorous confidence-interval analysis of the mean fluorescence lifetime of the pCaMKK2-S¹⁰⁰ W140 (A) and W445 (B) mutants in the absence (white-filled histogram) and presence (gray-filled histogram) of 14-3-3γ noW. Histograms constructed from 1000 Monte-Carlo MEM-fitting cycles (Herman and Lee, 2012) represent the probability of recovering a particular mean fluorescence lifetime from the data shown in Fig. 6 A,B. Dashed lines border 95% confidence intervals (2 standard deviations), the red line indicates the best-fitted value of Table 4. The histograms show that the mean fluorescence lifetime of the complex significantly increases in the presence of 14-3-3γ noW. See also Table 4 and Figure 7.

References

- Dosztanyi, Z., Csizmok, V., Tompa, P., and Simon, I. (2005). IUPred: web server for the prediction of intrinsically unstructured regions of proteins based on estimated energy content. *Bioinformatics* 21, 3433-3434.
- Herman, P., and Lee, J.C. (2012). The advantage of global fitting of data involving complex linked reactions. In *Allostery: Methods and Protocols*, A.W.W. Fenton, ed. (New York: Humana Press Inc.), pp. 399-421.
- Ishida, T., and Kinoshita, K. (2007). PrDOS: prediction of disordered protein regions from amino acid sequence. *Nucleic Acids Res* 35, W460-464.

CaMKK2 kinase domain interacts with the autoinhibitory region through the N-terminal lobe including the RP insert

Salome Kylarova^{1,2}, Katarina Psenakova^{1,2}, Petr Herman³, Veronika Obsilova^{2,*}, Tomas Obsil^{1,2,*}

¹Department of Physical and Macromolecular Chemistry, Faculty of Science, Charles University, Prague, Czech Republic

²BioCeV – Institute of Physiology, The Czech Academy of Sciences, Vestec, Czech Republic

³Institute of Physics, Faculty of Mathematics and Physics, Charles University, Prague, Czech Republic

Correspondence

T. Obsil, Department of Physical and Macromolecular Chemistry, Faculty of Science, Charles University, Prague, Czech Republic

Tel: +420 221951303

E-mail: obsil@natur.cuni.cz

V. Obsilova, BioCeV – Institute of Physiology, The Czech Academy of Sciences, Prague, Czech

Republic

Tel: +420 325873513

E-mail: veronika.obsilova@fgu.cas.cz

Abstract

Calcium/calmodulin-dependent protein kinase kinase 2 (CaMKK2), a member of the Ca^{2+} /calmodulin-dependent kinase (CaMK) family, functions as an upstream activator of CaMKI, CaMKIV and AMP-activated protein kinase. Thus, CaMKK2 is involved in the regulation of several key physiological and pathophysiological processes. Previous studies have suggested that Ca^{2+} /CaM binding may cause unique conformational changes in the CaMKs compared with other CaMKs. However, the underlying mechanistic details remain unclear. In this study, hydrogen-deuterium exchange coupled to mass spectrometry, time-resolved fluorescence spectroscopy, small-angle x-ray scattering and chemical cross-linking were used to characterize Ca^{2+} /CaM binding-induced structural changes in CaMKK2. Our data suggest that: (i) the CaMKK2 kinase domain interacts with the autoinhibitory region (AID) through the N-terminal lobe of the kinase domain including the RP insert, a segment important for targeting downstream substrate kinases; (ii) Ca^{2+} /CaM binding affects the structure of several regions surrounding the ATP-binding pocket, including the activation segment; (iii) although the CaMKK2: Ca^{2+} /CaM complex shows high conformational flexibility, most of its molecules are rather compact; and (iv) AID-bound Ca^{2+} /CaM transiently interacts with the CaMKK2 kinase domain. Thus, our results indicate that interactions between the CaMKK2 kinase domain and the AID differ from those of other CaMKs and that AID may inhibit CaMKK2 by both blocking access to the RP insert and by affecting the structure of the ATP-binding pocket.

Introduction

The calcium cation (Ca^{2+}) is a ubiquitous second messenger in cellular signaling with many effects mediated through a highly conserved, 17-kDa, Ca^{2+} -sensing protein: calmodulin (CaM). Binding of four Ca^{2+} ions to CaM induces a conformational change, which allows the protein to interact with and activate several target proteins, including a family of Ser/Thr protein kinases known as Ca^{2+} /CaM-dependent protein kinases (CaMKs) (reviewed by (Soderling and Stull, 2001; Swulius and Waxham, 2008)). CaMKs are responsible for regulating various cellular functions, such as gene transcription, apoptosis, cytoskeletal reorganization and learning and memory. Studies have suggested that all CaMKs share a similar domain organization with the kinase domain (KD) followed by the C-terminal autoinhibitory region (AID), which slightly overlaps with the CaM-binding domain (CBD) (Tokumitsu et al., 1997). At low intracellular Ca^{2+} concentrations, CaMKs are inhibited through the AID, which blocks the binding of substrates to the kinase domain and/or affects the structure of the catalytic site. The increase in Ca^{2+} concentrations induces Ca^{2+} /CaM binding to the CBD of CaMKs, thus relieving autoinhibition by disrupting the interaction between the AID and the kinase domain. The CaM molecule consists of two globular N- and C-terminal domains, each containing two EF-hand type Ca^{2+} -binding sites, which are connected by a linker that allows the globular domains to wrap around the helix of CBD within the target protein, thereby affecting the interaction between the AID and the kinase domain of CaMKs (reviewed by (Tidow and Nissen, 2013)). In addition to interactions with the CBD, CaM can also simultaneously interact with the kinase domain of CaMK, as shown by the crystal structure of the death-associated protein kinase (DAPK) bound to CaM (de Diego et al., 2010). In this structure, the CaM molecule adopted an extended conformation, which differed from that of CaM:CaMK peptide complexes, with both globular domains involved in interactions with the kinase domain of DAPK and reducing the accessibility of its active site.

Calcium/calmodulin-dependent protein kinase kinase (CaMKK), an upstream element of the CaMK signaling cascade, specifically phosphorylates Thr residues within the activation loop of two downstream kinases, CaMKI and CaMKIV, considerably increasing their catalytic efficiency and phosphorylation of multiple downstream targets (Haribabu et al., 1995). Two CaMKK isoforms (CaMKK1 and CaMKK2) have been identified in mammals in which CaMKK2 also participates in the regulation of energy balance through AMP-activated protein kinase (AMPK) activation (Anderson et al., 2008; Hurley et al., 2005). In fact, CaMKK2 is one of the most versatile CaMKs involved in adiposity regulation, glucose

homeostasis, hematopoiesis, inflammation, and cancer, and is considered a potential target for therapeutic intervention (reviewed in (Racioppi and Means, 2012)). Although both CaMKK isoforms share high similarity and identity in their amino acid sequences, they differ in their regulation. CaMKK1 is strictly activated by Ca^{2+} /CaM binding, whereas CaMKK2 is significantly active in the absence of Ca^{2+} /CaM (Anderson et al., 1998; Tokumitsu et al., 2000). This autonomous activity is regulated by a stretch of 23 amino acid residues located N-terminally to the catalytic domain, which may participate in the release of AID from the catalytic domain (Fig. 1) (Tokumitsu et al., 2001).

The kinase domain of CaMKK shows distinct differences from catalytic domains of other CaMKs. Sequence comparison showed the presence of a unique Arg-Pro-rich insert (RP insert) within the N-terminal lobe, which enables an efficient targeting and subsequent activation of CaMKI and CaMKIV (Tokumitsu et al., 1999). In addition, the crystal structure of the CaMKK2 kinase domain revealed that its C-lobe lacks the α D helix involved in hydrophobic interactions with the AID in CaMKI and CaMKII (Kukimoto-Niino et al., 2011; Rosenberg et al., 2005). Furthermore, the solution structure of the complex between Ca^{2+} /CaM and a peptide derived from the CaMKK1 CBD (Osawa et al., 1999) revealed that the binding orientation of this peptide in relation to the CaM globular domains is opposite to that observed in CBD peptides derived from myosin light chain kinase and CaMKII (Ikura et al., 1992; Meador et al., 1992, 1993; Rellos et al., 2010). In addition to these structural differences, the sequence and length of the CaMKK AID differ from those of CaMKI and CaMKII, thus suggesting that interactions between the CaMKK kinase domain and the AID substantially differ from those of other CaMKs. However, the underlying mechanistic details remain unclear.

Thus, in this study, we used hydrogen-deuterium exchange coupled to mass spectrometry (HDX-MS), time-resolved fluorescence spectroscopy, small-angle x-ray scattering (SAXS) and chemical cross-linking to characterize structural changes in CaMKK2 induced by Ca^{2+} /CaM binding.

Results

Ca²⁺/CaM binding affects the ATP-binding pocket of CaMKK2

To assess Ca²⁺/CaM-induced conformational changes in CaMKK2, HDX-MS was used to compare structural differences and changes in solvent accessibility in the absence and presence of Ca²⁺/CaM. To this end, a CaMKK2 construct encompassing residues 93–517 (hereafter referred to as CaMKK2) containing the catalytic domain (residues 160–450), the N-terminal regulatory segment and the C-terminal AID, which partly overlaps with the CBD (Fig. 1), was prepared. In addition, the catalytic aspartate residue of the kinase domain was mutated (D³³⁰A) to avoid autophosphorylation of the recombinant protein during expression.

In HDX, destabilization of the secondary structure, greater dynamics and higher solvent exposure increase the exchange rates. Conversely, stabilization of secondary structure elements and decreased access to the solvent manifest as decreased exchange rates. Ca²⁺/CaM binding-induced changes in the exchange rate of CaMKK2 were followed on 198 peptides from pepsin digest, together covering 100% of the sequence (supplemental Fig. S1). Twenty-two selected peptides covering the entire CaMKK2 93-517 sequence were then used to construct the deuterium uptake profiles after 60 s and 5 hours of deuteration (these two deuteration times were selected to examine changes on both short and long timescales). The comparison of the deuteration levels of CaMKK2 in the absence and in the presence of Ca²⁺/CaM revealed that several regions of the kinase domain and the C-terminal AID showed significant differences in exchange rate upon Ca²⁺/CaM binding (Figs. 2 and S2). A significant increase in exchange rate (deprotection) was observed in the strands β 4 and β 5, in the helix α C and in the RP insert within the N-lobe of the CaMKK2 KD, close to the ATP-binding pocket (Fig. 3A). Because faster deuterium incorporation can be interpreted as increased access to the solvent and/or as structural destabilization, the regions with faster deuteration upon Ca²⁺/CaM binding are likely involved in interactions with the AID in the absence of CaM.

Conversely, a significant decrease in exchange rate (protection) was observed in the CBD (residues 470-517, peptides P7 and P8 in Fig. S2) and in several regions of the catalytic domain, including the β 1 and β 2 strands and the loop between the β 2 and β 3 strands within the N-lobe, as well as two regions within the C-lobe (Figs. 3 and S2). One of these regions within the C-lobe contains the helix α E and the strands β 6- β 8 that form one side of the ATP binding pocket, whereas the other region is formed by the helix α EF, the β 11 strand and the N-terminal part of helix α F. The slower exchange rates observed in these regions likely reflect

either structural stabilization and/or decreased access to the solvent caused by the release of the AID from the kinase domain and/or by the interaction with the AID-Ca²⁺/CaM module. The profound decrease in exchange rate in the CBD region likely reflects its burial within the Ca²⁺/CaM structure as previously shown by solution structure of the complex between Ca²⁺/CaM and the CBD peptide derived from CaMKK1 (Osawa et al., 1999). Accordingly, most of the CaMKK2 KD regions, which were affected by the Ca²⁺/CaM binding, surround the ATP binding pocket and likely represent conformational changes that participate in the activation of CaMKK2 kinase activity.

CaMKK2 kinase domain conformational behavior and its changes upon Ca²⁺/CaM binding

Time-resolved tryptophan fluorescence intensity and anisotropy decay measurements of CaMKK2 were used to investigate the conformational behavior of CaMKK2 and its changes upon Ca²⁺/CaM binding. Based on the results from the HDX-MS measurements, six CaMKK2 mutants containing a single tryptophan residue in different regions (Trp128, Trp267, Trp337, Trp366, Trp374 and Trp390) were prepared (Fig. 4A). The sequence of CaMKK2 contains two tryptophan residues, Trp374 and Trp445, both located within the C-lobe of the kinase domain. Therefore, the mutant containing single Trp374 was created by mutating Trp445 to Phe. Mutants containing other tryptophans were generated by mutating both Trp374 and Trp445 to Phe and by introducing a single Trp residue at the desired position. The CaM is fluorescently silent because no tryptophan residue is present in its sequence.

Fluorescence intensity decay measurements showed that all tryptophan mutants of CaMKK2 exhibited complex emission decays with multimodal lifetime distributions. Ca²⁺/CaM binding significantly affected the microenvironment around the indole moiety of Trp267, Trp337 and Trp366, whereas nonsignificant effects were assessed on mutants containing Trp128, Trp374, and Trp390 (Table 1). The Trp267 residue is located within the strand β 5 of the N-lobe facing the ATP-binding pocket, the Trp337 is located within the activation segment, between strands β 9 and β 10, and the Trp366 is part of the strand β 11 within the loop connecting helices α EF and α F. Although the mean excited-state lifetime (τ_{mean}) of mutants containing Trp267 and Trp337 decreased upon Ca²⁺/CaM binding, the mutant containing Trp366 showed an increase in τ_{mean} . The τ_{mean} change of all three mutants is clearly visible in the raw data shown in Fig. S3, wherein the difference between fluorescence decays in the presence and absence of

$\text{Ca}^{2+}/\text{CaM}$ is higher than the data noise level. The analysis of the lifetime distribution, shown in Fig. 4B, indicates that the decrease in the τ_{mean} of Trp267 in the presence of $\text{Ca}^{2+}/\text{CaM}$ is mainly caused by the decrease in the intensity fraction associated with the dominant lifetime component centered around 5.6 ns and by the corresponding increase in fractions of the shorter components. Conversely, the decrease in the τ_{mean} of Trp337 is mainly caused by the shortening of the four lifetime components present in the distribution without dramatic changes in their individual contributions to the decay (Fig. 4C). In the case of Trp366, the increase in its τ_{mean} value results from the increase in the intensity fraction associated with the dominant lifetime component centered around 4.3 ns and from the shift of the shorter components to larger values (Fig. 4D).

Subsequently, the segmental motions of inserted tryptophans were studied using polarized time-resolved emission measurements. The fluorescence anisotropy decays revealed two classes of correlation times (Table 1). Short correlation times, with values up to few nanoseconds (ϕ_2 and ϕ_3 and a very fast unresolved component with $\phi_1 < 100$ ps), likely reflect the fast segmental motion of the protein near the tryptophan residue and Trp wobbling, whereas significantly longer correlation times ($\phi_4 > 40$ ns) likely reflect the overall rotational motion of CaMKK2. In several cases, an additional, very long correlation time, unresolvable with a Trp lifetime of few ns, was also detected ($\phi_{agg} > 200$ ns), likely reflecting minor protein aggregation. In this case, ϕ_3 shifted somewhat to lower values, which is consistent with the change in shape factors of possible aggregates (Lakowicz, 2006). Changes in the extent of segmental motion were assessed based on the change in the sum of amplitudes of fast anisotropy decay components ($\beta_{fast} = \beta_1 + \beta_2 + \beta_3$) (Rezabkova et al., 2012). Overall, lower values of β_{fast} indicate a more rigid environment. With some simplification, values of β_{fast} close to zero indicate a stiff protein that behave like a rigid rotor, whereas β_{fast} values close to the initial anisotropy r_0 ($r_0 = 0.22$ in our case) indicate a loose structure, wherein fluorescence is rapidly depolarized by fast movements. Hence, all tryptophans, except Trp128 and Trp366, are located in rather rigid regions of the kinase domain, and $\text{Ca}^{2+}/\text{CaM}$ binding caused no significant changes in the flexibility of the study regions. The only exception is the most mobile CaMKK2 Trp366 mutant, which showed a significant decrease in β_{fast} and a decrease in correlation times ϕ_1 and ϕ_2 . This suggested reduced amplitudes and different character of the internal motion in the region surrounding this tryptophan residue upon $\text{Ca}^{2+}/\text{CaM}$ binding. Signs of microenvironment rigidization were also detected in the Trp128 mutant.

Therefore, fluorescence lifetime and anisotropy results indicate that $\text{Ca}^{2+}/\text{CaM}$ binding affects the CaMKK2 KD conformation in several regions, such as the $\beta 5$ strand close to the ATP-binding pocket and two regions within the C-lobe, including the activation segment.

Molecules of the CaMKK2: $\text{Ca}^{2+}/\text{CaM}$ complex are compact

The recently reported crystal structure of the DAPK-CaM complex suggested that, in addition to the AID, the $\text{Ca}^{2+}/\text{CaM}$ can also directly interact with the kinase domain of some CaMKs (de Diego et al., 2010). To assess whether this direct interaction would also occur in CaMKK2, small angle x-ray scattering, chemical cross-linking and molecular docking were used to study the architecture of the CaMKK2₉₃₋₅₁₇: $\text{Ca}^{2+}/\text{CaM}$ complex. X-ray scattering data were collected for the CaMKK2₉₃₋₅₁₇, $\text{Ca}^{2+}/\text{CaM}$ and the CaMKK2₉₃₋₅₁₇: $\text{Ca}^{2+}/\text{CaM}$ complex prepared at 1:1 molar stoichiometry (Table 2 and Fig. 5). The complex samples were prepared at protein concentrations ranging from 2.4 to 10.7 mg.mL⁻¹. However, only samples with low protein concentration (2.4 and 5.8 mg.mL⁻¹) were monodisperse, as indicated by the linearity of Guinier plots at s values lower than $1.3/R_g$ (inset in Fig. 5A). Due to the presence of attractive inter-particle interactions, as indicated by the concentration dependence on the radius of gyration (R_g) and by the forward scattering intensity $I(0)$, the scattering curve of the complex at the lowest protein concentration 2.4 mg.mL⁻¹ was selected for further analysis. The apparent M_w values of ~46, ~20 and ~64 kDa estimated for CaMKK2, for $\text{Ca}^{2+}/\text{CaM}$ and for the complex, respectively, based on the forward scattering intensity $I(0)$, match their expected M_w values of 48, 17 and 65 kDa, respectively. The pair-distance distribution function $P(r)$ of CaMKK2 alone and of its complex with $\text{Ca}^{2+}/\text{CaM}$ showed similar maximum particle distance (D_{max}); however, the $P(r)$ -distribution function of the complex showed a higher proportion of inter-atomic distances between 6 and 10 nm (Fig. 5B).

The dimensionless Kratky plot ($(sR_g)2I(s)/I(0)$ versus sR_g) was used to characterize the protein flexibility of the CaMKK2: $\text{Ca}^{2+}/\text{CaM}$ complex (Fig. 5C). The scattering data of compact globular proteins in this plot show a maximum value of 1.104 at $sR_g \sim 1.73$ (marked by red lines in Fig. 5C) (Receveur-Brechot and Durand, 2012). As shown, both CaMKK2 and the CaMKK2: $\text{Ca}^{2+}/\text{CaM}$ complex had higher maxima, indicating that both molecules show substantial conformational flexibility. Therefore, an ensemble optimization method (EOM) (Tria et al., 2015) was then used to model the CaMKK2: $\text{Ca}^{2+}/\text{CaM}$ complex structure as an ensemble of conformers. The CaMKK2 KD and the $\text{Ca}^{2+}/\text{CaM}$ bound to the CBD were treated as rigid bodies and the flexible N- and C-terminal segments of CaMKK2 as chains of

dummy residues. An initial pool of 10,000 conformers was initially generated, and a genetic algorithm was then used to select an ensemble of conformers that collectively fitted the experimental SAXS data with a χ^2 value of 1.12 (Fig. 5D). In addition, its R_g and D_{\max} distributions are clearly biased toward more compact structures with lower R_g and D_{\max} values than those of the pool (Figs. 5E and 5F). The average R_g and D_{\max} values of the ensemble (36.6 and 121 Å, respectively) are consistent with values calculated using scattering data (Table 2). Moreover, the R_g and D_{\max} distributions of the CaMKK2:Ca²⁺/CaM complex have smaller extents than those of the pools, indicating that its accessible conformations are not fully randomly distributed and that the complex is unable to be fully extended in solution, thereby suggesting that a substantial portion of molecules is rather compact, with a R_g of < 35 Å and a D_{\max} of < 120 Å. Furthermore, the presence of compact complexes also suggests that the kinase domain and Ca²⁺/CaM may directly, but transiently, interact with each other.

CaMKK2 KD directly interacts with the AID-Ca²⁺/CaM module

Chemical cross-linking combined with mass spectrometry was used to further investigate the direct contacts between the CaMKK2 KD and Ca²⁺/CaM and to collect structural data on their relative positions. Two amine-reactive cross-linking agents, disuccinimidyl glutarate (DSG) and disuccinimidyl suberate (DSS), which differ in spacer arm length (~7.7 and ~11.4 Å, respectively), were used. The identified intermolecular cross-links connecting three different regions of CaMKK2 KD to three different regions of CaM are listed in Table 3. In two cases, we were unable to identify the exact cross-linked residue because the corresponding peptide contained two closely located lysine residues. Cross-links #1 and #3 connect CaMKK2 AID-CBD Lys493 to the C-terminus of CaM containing Lys149. Cross-links #2 and #5 were identified between the helix α I at the C-terminus of CaMKK2 KD containing Lys441 and the linker that connects the N- and C-terminal domains of CaM containing Lys76 and Lys78. The cross-link #4 connects CaMKK2 AID-CBD Lys493 to CaM Lys78. Finally, the cross-link #6 connects the strand β 4 in the N-lobe of CaMKK2 KD containing Lys250 to the first N-terminal helix of CaM containing Lys14. Because the C α -C α distances of lysine residues cross-linked by DSG and DSS are ~20 and ~24 Å, respectively, the presence of several cross-links between the CaMKK2-KD and CaM (cross-links #2, 5, and 6) indicates that Ca²⁺/CaM, when bound to the CBD, directly interacts with the kinase domain of CaMKK2.

To visualize the transient interaction between the CaMKK2 KD and $\text{Ca}^{2+}/\text{CaM}$, docking simulation was performed using the program HADDOCK (Dominguez et al., 2003) with the crystal structure of the CaMKK2 KD (PDB ID: 5UY6), the solution structure of $\text{Ca}^{2+}/\text{CaM}$ bound to the CBD of CaMKK1 (PDB ID: 1CKK) (Osawa et al., 1999) and intermolecular distance constraints assessed in chemical cross-linking experiments. The final model, the structure with the lowest intermolecular energy, is consistent with most distance constraints assessed in chemical cross-linking experiments (Fig. 6) and suggests that the CaMKK2 KD interacts with $\text{Ca}^{2+}/\text{CaM}$ preferentially through surfaces surrounding the C-terminal part of the helix αE . However, because substantial protection after 5 hours of deuteration in the presence of $\text{Ca}^{2+}/\text{CaM}$ was also observed in the $\beta 2\text{--}\beta 3$ and $\alpha\text{EF--}\beta 11$ loops, $\text{Ca}^{2+}/\text{CaM}$ may also interact with these regions.

Discussion

Previous structural studies on several CaMKs, including CaMKI, CaMKII and CaMKIV, have shown that the AID emerges from the base of the kinase domain and runs through the groove between helices α D and α E where it affects the position of the helix α D and subsequently the conformation of residues within the ATP binding site (Fig. 3B) (Goldberg et al., 1996; Chao et al., 2011; Rosenberg et al., 2005). In addition, the C-terminal part of AID of several CaMKs was also shown to occupy the ATP-binding pocket (Goldberg et al., 1996; Hu et al., 1994). However, the C-lobe of the CaMKK2 KD lacks the α D helix, and the sequence and length of the CaMKK AID differ from those of CaMKI and CaMKII (Kukimoto-Niino et al., 2011), thus suggesting that the CaMKK AID may interact with different regions of the kinase domain, in contrast to other CaMKs. The HDX-MS results reported in this study indicate that the CaMKK2 AID interacts with surfaces formed by strands β 4 and β 5 and by the helix α C because peptides from these segments showed higher solvent exposure (increased exchange rate) upon Ca^{2+} /CaM binding. These surfaces are located on the opposite side of the kinase domain in relation to regions involved in interactions with the AID in other CaMKs (Fig. 3), thus corroborating the hypothesis that interactions between the CaMKK KD and the AID differ from those of other CaMKs (Kukimoto-Niino et al., 2011; Osawa et al., 1999; Tokumitsu et al., 1999).

In addition to regions with increased exchange rate, several parts of the CaMKK2 KD, including the helix α E and segments containing strands β 1- β 2 and β 6- β 8, showed a decreased exchange rate upon complex formation. All these regions surround the ATP binding pocket and likely translate Ca^{2+} /CaM binding-induced conformational changes. This was further corroborated by the results of time-resolved tryptophan fluorescence measurements of Trp267, located within the strand β 5 close to the ATP-binding pocket, and of Trp337, which is located within the activation segment (Fig. 4 and Table 1). Therefore, these data suggest that Ca^{2+} /CaM binding induces structural changes in regions surrounding the ATP-binding pocket, which likely contribute to the activation of CaMKK2. In addition, the regions with increased solvent exposure upon Ca^{2+} /CaM binding included the RP insert, a unique Arg-Pro-rich segment, which allows efficient targeting and subsequent activation of the downstream kinases CaMKI and CaMKIV (Tokumitsu et al., 1999). This suggests that the CaMKK2 AID blocks the access to this region and that this interaction is relieved by Ca^{2+} /CaM binding to the CBD.

A structural study of DAPK, a CaMK involved in several apoptotic and autophagic cell death pathways (Gozuacik and Kimchi, 2006), revealed that $\text{Ca}^{2+}/\text{CaM}$ can, in addition to interacting with the CBD, simultaneously interact with the kinase domain (de Diego et al., 2010). Several regions of the CaMKK2 KD showed protection in the presence of $\text{Ca}^{2+}/\text{CaM}$, even after 5 hours of deuteration (Fig. 2B). Such protection can be interpreted as either stabilization of secondary structure elements and/or decreased access to the solvent due to, for example, interaction with the AID- $\text{Ca}^{2+}/\text{CaM}$ module. EOM analysis of SAXS data and the results of chemical cross-linking experiments suggested that a substantial portion of the CaMKK2: $\text{Ca}^{2+}/\text{CaM}$ complex molecules is rather compact and that $\text{Ca}^{2+}/\text{CaM}$ is located close to the kinase domain of CaMKK2 (Fig. 5 D-F and Table 3). Therefore, these results further supported the hypothesis that the kinase domain of CaMKK2 and the AID- $\text{Ca}^{2+}/\text{CaM}$ module may directly interact with each other. This interaction, however, would be rather transient, as suggested by the dimensionless Kratky plot (Fig. 5C), which indicated that the CaMKK2: $\text{Ca}^{2+}/\text{CaM}$ complex shows substantial conformational flexibility.

The model of the CaMKK2: $\text{Ca}^{2+}/\text{CaM}$ complex, which was build using the distance constraints assessed in chemical cross-linking experiments, suggested that the AID- $\text{Ca}^{2+}/\text{CaM}$ module interacts with the region centered around the C-terminal part of helix αE (Fig. 6). In this position, the $\text{Ca}^{2+}/\text{CaM}$ should not restrict the access to the active site, which is located on the opposite side of the kinase domain. The model of the CaMKK2: $\text{Ca}^{2+}/\text{CaM}$ complex is consistent with all cross-linking data except for cross-link #4, which connects CaMKK2 AID-CBD Lys493 to CaM Lys78. The presence of this cross-link suggests that some portion of $\text{Ca}^{2+}/\text{CaM}$ molecules binds in an opposite orientation to that observed in the complex between $\text{Ca}^{2+}/\text{CaM}$ and the CBD peptide from CaMKKI (Osawa et al., 1999) because this orientation would bring CaMKK2 Lys493 and CaM Lys78 close to each other.

In conclusion, our data contribute to understanding how $\text{Ca}^{2+}/\text{CaM}$ interacts with and affects the structure of CaMKK2. Interactions between the CaMKK2 KD and the AID differ from those of other CaMKs and apparently involve surfaces of the N-terminal lobe of the kinase domain, including the RP insert. $\text{Ca}^{2+}/\text{CaM}$ binding affects the structure of regions surrounding the ATP-binding pocket as well as the activation segment. Moreover, our data also suggest that a substantial portion of the CaMKK2: $\text{Ca}^{2+}/\text{CaM}$ molecules are rather compact, and the AID-bound $\text{Ca}^{2+}/\text{CaM}$ transiently interacts with the kinase domain of CaMKK2. Thus, our results indicate that interactions between the CaMKK2 kinase domain and the AID differ from those of other CaMKs and that the AID inhibits CaMKK2 by blocking the RP insert and by affecting the structure of the ATP-binding pocket

Materials and Methods

Expression, purification and phosphorylation of CaMKK2

DNA encoding human CaMKK2 (residues 93–517) was ligated into pRSFDuet-1 (Novagen) using BamHI and NotI sites. Modified pRSFDuet-1 containing the sequence of the His₆-tagged GB1 domain of protein G inserted into the first multiple cloning site was a gift from Evzen Boura (Institute of Organic Chemistry and Biochemistry AS CR, Prague, Czech Republic). CaMKK2 (93-517) was expressed as N-terminal His₆-GB1-tagged fusion protein in *Escherichia coli* BL21 (DE3) cells. Protein expression was conducted in autoinduction media for 5 h at 37°C and then 16 h at 20°C, and the protein was purified using Chelating Sepharose Fast Flow (GE Healthcare), according to the standard protocol. The eluted protein was dialyzed against the buffer containing 50 mM Tris-HCl (pH 8), 0.5 M NaCl, 4 mM 2-mercaptoethanol, 4 mM EDTA and 10% (w/v) glycerol and the His₆-GB1 tag was cleaved by incubation with TEV protease (250 U of TEV/mg of fusion protein) at 30°C for 1 h. The final purification step was size-exclusion chromatography on a HiLoad 26/600 Superdex 75 column (GE Healthcare) in buffer containing 50 mM Tris-HCl (pH 8), 500 mM NaCl, 5 mM DTT, and 10% (w/v) glycerol. All mutants of CaMKK2 were generated using the QuikChange site-directed mutagenesis kit (Stratagene), and the mutations were confirmed by sequencing. The stability of mutants prepared was assessed by measuring the temperature of the unfolding transition (T_m) by differential scanning fluorimetry (Niesen et al., 2007), and no significant differences in T_m were observed.

Expression and purification of CaM

Rat CaM was prepared as described previously (Holakovska et al., 2011).

Hydrogen/deuterium exchange coupled to mass spectrometry

HDX of CaMKK2_{93–517} and the CaMKK2_{93–517}:Ca²⁺/CaM complex was initiated by 10-fold dilution in a deuterated buffer containing 50 mM Tris-HCl (pH/pD 7.5), 150 mM NaCl, 1 mM TCEP and 1 mM CaCl₂. The final protein concentration was 3 μM. Aliquots (25 μL) were taken after 20 s, 1 min, 3 min, 10 min, 1 h, 3 h and 5 h of exchange. The exchange was quenched by adding 25 μL of 1M glycine (pH 2.3) and fast freezing in liquid nitrogen. The deuterated samples (HPLC-MS) were analyzed on a HPLC column (1200 Agilent technologies, Waldbronn, Germany) connected to the ESI-FT-ICR MS (15T solarix, Bruker Daltonics, Billerica, MA). The analysis started with quick thawing of the sample followed by digestion on a pepsin column (66 μL bed volume, flow rate 100 μL.min⁻¹). The resulting

peptides were online desalted on a Peptide microtrap column (Optimize Technologies, Oregon City, OR) and separated on a C18 reversed phase column (ZORBAX 300SB-C18 3.5 μ m, 0.5 x 35 mm, Agilent, Santa Clara, CA) using a linear gradient 10–45% B in 20 min, where solvent A was 2% acetonitrile/0.4% formic acid in water, solvent B 95% acetonitrile/5% water/0.4% formic acid. The injection and switching valve, the pepsin column, the peptide trap and the analytical column were placed in an icebox to minimize back exchange. Peptide identification (mapping, HPLC-MS/MS) was performed using the system described above, and the MS/MS spectra were searched by MASCOT against a database containing sequences of CaMKK2 and CaM. Spectra of partly deuterated peptides were processed using the software Data Analysis 4.2 (Bruker Daltonics, Billerica, MA) and an in-house software program termed DeutEx.

Chemical cross-linking combined with mass spectrometry

The CaMKK2_{93–517} and the CaMKK2_{93–517}:Ca²⁺/CaM complex were cross-linked with homobifunctional cross-linkers disuccinimidyl suberate (DSS) and disuccinimidyl glutarate (DSG). Cross-linkers DSS and DSG were used as 1:1 (mol/mol) mixtures of non-deuterated and four-times deuterated compounds (d0/d4). For the cross-linking reaction, the proteins were transferred to buffer containing 10 mM HEPES (pH 7.5) with 150 mM NaCl, 0.1 mM TCEP and 1 mM CaCl₂ and the protein concentration in all samples was 1 mg.mL⁻¹. Freshly prepared stock solutions of cross-linkers (10 mg.mL⁻¹ in DMSO) were added to proteins in 20 \times or 50 \times molar excess in a total reaction volume of 20 μ L. Reaction mixtures were incubated for 1 h at room temperature. Cross-linked samples were separated on NuPAGE 4–12% Bis–Tris gel using MES running buffer, and the bands corresponding to a monomeric cross-linked protein were excised. Cysteines were reduced with 50 mM DTT for 45 min at 60°C, and free cysteines were alkylated with 100 mM iodoacetamide for 30 min at room temperature, in the dark. Trypsin digestion proceeded overnight at 37°C with an enzyme/protein ratio of 1:20 (w/w). The resulting peptide mixtures were desalted on a Peptide microtrap column (Optimize Technologies, Oregon City, OR). Peptides extracted from the gel were loaded on a trap column (ZORBAX 300SB-C18, 5 μ m, 5 \times 0.3 mm, Agilent, Santa Clara, CA) and desalted for 5 min at flow rate 20 μ L/min. Peptides were then separated by reversed phase C18 column (ZORBAX SB C18 RR 3.5 μ 150 \times 0.3 mm, Agilent, Santa Clara, CA) at a flow rate 10 μ L/min using capillary HPLC system (Agilent Technologies) under the following gradient conditions: 1–10% B in 1 min, 10–45% B in 19 min, 45–95% B in 5 min,

where solvent A was 0.1% formic acid, 2.0% acetonitrile in water and solvent B was 0.1% formic acid in 98% acetonitrile. The column was heated at 50°C and connected directly to an 15T solariX FT-ICR mass spectrometer (Bruker Daltonics) using an electrospray ion source. The instrument was on line calibrated resulting in mass accuracy below 2 ppm. Data acquisition and data processing were performed by fimsControl 2.1.0 and DataAnalysis 4.2 (Bruker Daltonics). The cross-links were identified using Links software (Young et al., 2000). The Links algorithm was set to consider the carbamidomethylation of cysteine and the possible single oxidation of methionine. The mass error threshold was kept below 2 ppm and all assigned fragments were verified manually.

Small angle x-ray scattering

SAXS data were collected at the European Molecular Biology Laboratory (EMBL) P12 beamline, at the storage ring PETRA III (Deutsches Elektronen Synchrotron (DESY), Hamburg, Germany). The SAXS measurements were conducted in buffer containing 50 mM Tris-HCl (pH 7.5), 150 mM NaCl, 1mM TCEP, 1 mM CaCl₂, and 3% (w/v) glycerol, using 2.3–5 mg.mL⁻¹ CaMKK2_{93–517}, 0.8–3.9 mg.mL⁻¹ CaM and 2.4–10.7 mg.mL⁻¹ CaMKK2_{93–517}:Ca²⁺/CaM complex (1:1 molar stoichiometry). The forward scattering $I(0)$ and the radius of gyration R_g were calculated using the Guinier approximation for a s ($s = 4\pi\sin(\theta)/\lambda$, where 2θ is the scattering angle and λ is the wavelength) range that satisfies the $sR_g < 1.3$ condition. The distance distribution functions $P(r)$ and the maximum particle dimensions D_{\max} were computed using the program GNOM (Svergun, 1992). The solute apparent molecular mass (MM_{exp}) was estimated by comparing the forward scattering both with that of reference solutions of bovine serum albumin and with that of the excluded volume of the hydrated particle (the Porod volume) V_p (Petoukhov et al., 2012). V_p was computed using the program PRIMUS (Konarev et al., 2003). The analysis based on the ensemble optimization method was performed using the program EOM (Tria et al., 2015).

Time-resolved fluorescence measurements

Time-resolved fluorescence intensity and anisotropy decay measurements, as well as data analysis, were performed as previously described (Kosek et al., 2014; Rezabkova et al., 2010). Tryptophan emission was excited at 298 nm by a tripled output of the Ti:Sapphire laser. Tryptophan fluorescence was isolated at 355 nm using a combination of monochromator and a stack of UG1 and BG40 glass filters (Thorlabs) placed in front of the input slit. Samples were placed in a thermostatic holder, and all experiments were performed at 23°C in buffer

containing 20 mM Tris-HCl (pH 7.5), 150 mM NaCl, 1 mM TCEP, 1 mM CaCl₂ and 10% (w/v) glycerol. The CaMKK2_{93–517} and CaM concentrations were 15 and 30 μM, respectively.

Docking calculations

The docking simulation was performed using the program HADDOCK (Dominguez et al., 2003) with the crystal structure of the CaMKK2 KD (PDB ID: 5UY6), the solution structure of Ca²⁺/CaM bound to the CBD of CaMKK1 (PDB ID: 1CKK) (Osawa et al., 1999), and intermolecular distance constraints assessed in chemical cross-linking experiments. The residues in CaMKK2 KD that showed substantially lower deuterium incorporation (protection) after 5 hours of deuteration in the presence of Ca²⁺/CaM (regions 182-190, 292-341, and 354-373) were defined as the binding interface in HADDOCK calculation. The binding interface on the CaM molecule was defined based on the results from chemical cross-linking experiments. Ambiguous Interaction Restraints (AIRs) in both CaMKK2 KD and CaM molecules were defined according to the general HADDOCK rules (Dominguez et al., 2003).

Acknowledgement

This study was supported by the Czech Science Foundation (Projects 16-02739S), the Grant Agency of the Charles University (Project 368216), the Czech Academy of Sciences (Research Projects RVO: 67985823 of the Institute of Physiology), EU supported projects BIOCEV (CZ.1.05/1.1.00.02.0109) and Operational Programme “Research and Development for Innovation” (no. CZ.1.05/4.1.00/16.0340), and Czech Infrastructure for Integrative Structural Biology (CIISB) project LM2015043, funded by MEYS CR. We thank Dr. Petr Pompach for the mass spectrometry analyses and Dr. Carlos V. Melo for proofreading the article.

Author contributions

V.O. and T.O. designed research; S.K., K.P., P.H., and T.O. performed research; S.K., K.P., P.H., V.O., and T.O. analyzed data; and V.O. and T.O. wrote the paper.

Conflict of interest: The authors declare no conflict of interest

References

- Anderson, K.A., Means, R.L., Huang, Q.H., Kemp, B.E., Goldstein, E.G., Selbert, M.A., Edelman, A.M., Freneau, R.T., and Means, A.R. (1998). Components of a calmodulin-dependent protein kinase cascade. Molecular cloning, functional characterization and cellular localization of Ca²⁺/calmodulin-dependent protein kinase kinase beta. *J Biol Chem* 273, 31880-31889.
- Anderson, K.A., Ribar, T.J., Lin, F., Noeldner, P.K., Green, M.F., Muehlbauer, M.J., Witters, L.A., Kemp, B.E., and Means, A.R. (2008). Hypothalamic CaMKK2 contributes to the regulation of energy balance. *Cell Metab* 7, 377-388.
- de Diego, I., Kuper, J., Bakalova, N., Kursula, P., and Wilmanns, M. (2010). Molecular basis of the death-associated protein kinase-calcium/calmodulin regulator complex. *Science signaling* 3, ra6.
- Dominguez, C., Boelens, R., and Bonvin, A.M. (2003). HADDOCK: a protein-protein docking approach based on biochemical or biophysical information. *J Am Chem Soc* 125, 1731-1737.
- Goldberg, J., Nairn, A.C., and Kuriyan, J. (1996). Structural basis for the autoinhibition of calcium/calmodulin-dependent protein kinase I. *Cell* 84, 875-887.
- Gozuacik, D., and Kimchi, A. (2006). DAPK protein family and cancer. *Autophagy* 2, 74-79.
- Haribabu, B., Hook, S.S., Selbert, M.A., Goldstein, E.G., Tomhave, E.D., Edelman, A.M., Snyderman, R., and Means, A.R. (1995). Human calcium-calmodulin dependent protein kinase I: cDNA cloning, domain structure and activation by phosphorylation at threonine-177 by calcium-calmodulin dependent protein kinase I kinase. *EMBO J* 14, 3679-3686.
- Holakovska, B., Grycova, L., Bily, J., and Teisinger, J. (2011). Characterization of calmodulin binding domains in TRPV2 and TRPV5 C-tails. *Amino Acids* 40, 741-748.
- Hu, S.H., Parker, M.W., Lei, J.Y., Wilce, M.C., Benian, G.M., and Kemp, B.E. (1994). Insights into autoregulation from the crystal structure of twitchin kinase. *Nature* 369, 581-584.
- Hurley, R.L., Anderson, K.A., Franzone, J.M., Kemp, B.E., Means, A.R., and Witters, L.A. (2005). The Ca²⁺/calmodulin-dependent protein kinase kinases are AMP-activated protein kinase kinases. *J Biol Chem* 280, 29060-29066.
- Chao, L.H., Stratton, M.M., Lee, I.H., Rosenberg, O.S., Levitz, J., Mandell, D.J., Kortemme, T., Groves, J.T., Schulman, H., and Kuriyan, J. (2011). A mechanism for tunable autoinhibition in the structure of a human Ca²⁺/calmodulin-dependent kinase II holoenzyme. *Cell* 146, 732-745.
- Ikura, M., Clore, G.M., Gronenborn, A.M., Zhu, G., Klee, C.B., and Bax, A. (1992). Solution structure of a calmodulin-target peptide complex by multidimensional NMR. *Science* 256, 632-638.
- Konarev, P.V., Volkov, V.V., Sokolova, A.V., Koch, M.H.J., and Svergun, D.I. (2003). PRIMUS: a Windows PC-based system for small-angle scattering data analysis. *Journal of Applied Crystallography* 36, 1277-1282.
- Kosek, D., Kylarova, S., Psenakova, K., Rezabkova, L., Herman, P., Vecer, J., Obsilova, V., and Obsil, T. (2014). Biophysical and structural characterization of the thioredoxin-binding domain of protein kinase ASK1 and its interaction with reduced thioredoxin. *J Biol Chem* 289, 24463-24474.
- Kukimoto-Niino, M., Yoshikawa, S., Takagi, T., Ohsawa, N., Tomabechei, Y., Terada, T., Shirouzu, M., Suzuki, A., Lee, S., Yamauchi, T., *et al.* (2011). Crystal structure of the Ca²⁺/calmodulin-dependent protein kinase kinase in complex with the inhibitor STO-609. *J Biol Chem* 286, 22570-22579.
- Lakowicz, J.R. (2006). Principles of fluorescence spectroscopy, Third edition (New York: Springer).
- Meador, W.E., Means, A.R., and Quirocho, F.A. (1992). Target enzyme recognition by calmodulin: 2.4 A structure of a calmodulin-peptide complex. *Science* 257, 1251-1255.
- Meador, W.E., Means, A.R., and Quirocho, F.A. (1993). Modulation of calmodulin plasticity in molecular recognition on the basis of x-ray structures. *Science* 262, 1718-1721.

- Niesen, F.H., Berglund, H., and Vedadi, M. (2007). The use of differential scanning fluorimetry to detect ligand interactions that promote protein stability. *Nature protocols* 2, 2212-2221.
- Osawa, M., Tokumitsu, H., Swindells, M.B., Kurihara, H., Orita, M., Shibamura, T., Furuya, T., and Ikura, M. (1999). A novel target recognition revealed by calmodulin in complex with Ca²⁺-calmodulin-dependent kinase kinase. *Nat Struct Biol* 6, 819-824.
- Petoukhov, M.V., Franke, D., Shkumatov, A.V., Tria, G., Kikhney, A.G., Gajda, M., Gorba, C., Mertens, H.D., Konarev, P.V., and Svergun, D.I. (2012). New developments in the program package for small-angle scattering data analysis. *J Appl Crystallogr* 45, 342-350.
- Racioppi, L., and Means, A.R. (2012). Calcium/calmodulin-dependent protein kinase kinase 2: roles in signaling and pathophysiology. *J Biol Chem* 287, 31658-31665.
- Receveur-Brechot, V., and Durand, D. (2012). How random are intrinsically disordered proteins? A small angle scattering perspective. *Current protein & peptide science* 13, 55-75.
- Rellos, P., Pike, A.C., Niesen, F.H., Salah, E., Lee, W.H., von Delft, F., and Knapp, S. (2010). Structure of the CaMKII δ /calmodulin complex reveals the molecular mechanism of CaMKII kinase activation. *PLoS biology* 8, e1000426.
- Rezabkova, L., Boura, E., Herman, P., Vecer, J., Bourova, L., Sulc, M., Svoboda, P., Obsilova, V., and Obsil, T. (2010). 14-3-3 protein interacts with and affects the structure of RGS domain of regulator of G protein signaling 3 (RGS3). *J Struct Biol* 170, 451-461.
- Rezabkova, L., Kacirova, M., Sulc, M., Herman, P., Vecer, J., Stepanek, M., Obsilova, V., and Obsil, T. (2012). Structural modulation of phosphatidylcholine by phosphorylation and 14-3-3 protein binding. *Biophys J* 103, 1960-1969.
- Rosenberg, O.S., Deindl, S., Sung, R.J., Nairn, A.C., and Kuriyan, J. (2005). Structure of the autoinhibited kinase domain of CaMKII and SAXS analysis of the holoenzyme. *Cell* 123, 849-860.
- Soderling, T.R., and Stull, J.T. (2001). Structure and regulation of calcium/calmodulin-dependent protein kinases. *Chem Rev* 101, 2341-2352.
- Svergun, D.I. (1992). Determination of the Regularization Parameter in Indirect-Transform Methods Using Perceptual Criteria. *Journal of Applied Crystallography* 25, 495-503.
- Swulius, M.T., and Waxham, M.N. (2008). Ca²⁺/calmodulin-dependent protein kinases. *Cell Mol Life Sci* 65, 2637-2657.
- Tidow, H., and Nissen, P. (2013). Structural diversity of calmodulin binding to its target sites. *FEBS J* 280, 5551-5565.
- Tokumitsu, H., Iwabu, M., Ishikawa, Y., and Kobayashi, R. (2001). Differential regulatory mechanism of Ca²⁺/calmodulin-dependent protein kinase kinase isoforms. *Biochemistry* 40, 13925-13932.
- Tokumitsu, H., Muramatsu, M., Ikura, M., and Kobayashi, R. (2000). Regulatory mechanism of Ca²⁺/calmodulin-dependent protein kinase kinase. *J Biol Chem* 275, 20090-20095.
- Tokumitsu, H., Takahashi, N., Eto, K., Yano, S., Soderling, T.R., and Muramatsu, M. (1999). Substrate recognition by Ca²⁺/Calmodulin-dependent protein kinase kinase. Role of the arg-pro-rich insert domain. *J Biol Chem* 274, 15803-15810.
- Tokumitsu, H., Wayman, G.A., Muramatsu, M., and Soderling, T.R. (1997). Calcium/calmodulin-dependent protein kinase kinase: identification of regulatory domains. *Biochemistry* 36, 12823-12827.
- Tria, G., Mertens, H.D., Kachala, M., and Svergun, D.I. (2015). Advanced ensemble modelling of flexible macromolecules using X-ray solution scattering. *IUCrJ* 2, 207-217.
- Young, M.M., Tang, N., Hempel, J.C., Oshiro, C.M., Taylor, E.W., Kuntz, I.D., Gibson, B.W., and Dollinger, G. (2000). High throughput protein fold identification by using experimental constraints derived from intramolecular cross-links and mass spectrometry. *Proc Natl Acad Sci U S A* 97, 5802-5806.

Figure legends

Figure 1.

Domain organization of CaMKK2. The N-terminal regulatory region regulates autonomous activity (activity in the absence of $\text{Ca}^{2+}/\text{CaM}$) of CaMKK2. The AID, which overlaps with the CBD, blocks substrate binding to the kinase domain and/or affects the structure of the catalytic site at low intracellular Ca^{2+} concentrations. $\text{Ca}^{2+}/\text{CaM}$ binding disrupts the interaction between the AID and the kinase domain and relieves the autoinhibition.

Figure 2.

$\text{Ca}^{2+}/\text{CaM}$ -binding induced changes in the deuteration levels of CaMKK2. Plots showing the deuteration levels of CaMKK2 in the absence (black traces) and presence of $\text{Ca}^{2+}/\text{CaM}$ (red traces) after 60 seconds (A) and 5 hours (B) of deuteration. The positions of secondary structure elements of the CaMKK2 KD are indicated at the top by black rectangles. The positions of tryptophan residues used in the time-resolved fluorescence experiments are indicated by green dots. P1-P8 indicate peptides whose deuteration kinetics is shown in detail in Fig. S2.

Figure 3.

$\text{Ca}^{2+}/\text{CaM}$ binding-induced changes within the kinase domain of CaMKK2. (A) Color-coded HDX-MS results of $\text{Ca}^{2+}/\text{CaM}$ binding-induced changes in CaMKK2 mapped to the crystal structure of the CaMKK2 KD (PDB ID: 5UY6). The ATP-binding pocket is occupied by the small molecule 8R4. (B) Comparison with other CaMKs. Structures of the CaMKI KD-AID (PDB ID: 1A06) (Goldberg et al., 1996), the CaMKII KD-AID (PDB ID: 3SOA) (Chao et al., 2011), and the CaMKIV KD-AID (PDB ID: 2W4O) are shown in the same orientation as that of CaMKK2 KD in the left panel of (A). The C-terminal hub domain of CaMKII is not shown for better clarity. The AID regions of CaMKI and CaMKII are shown in dark gray with the CBD in orange.

Figure 4.

Time-resolved tryptophan fluorescence measurements of CaMKK2. (A) The crystal structure of the CaMKK2 KD (PDB ID: 5UY6) was colored as in Fig. 3A, according to HDX-MS results. Residues Trp374 and phenylalanines F267, F337, F366 and F390, which were replaced by Trp, are shown as green spheres. (B-D) Excited state lifetime distribution of

CaMKK2₉₃₋₅₁₇ W267 (panel B), W337 (panel C) and W366 (panel D) in the absence (gray-filled distributions) and presence of Ca²⁺/CaM (red distributions).

Figure 5.

SAXS Analysis of the CaMKK2:Ca²⁺/CaM Complex. (A) Scattering intensity as a function of the scattering vector s ($s = 4\pi\sin(\theta/\lambda)$, where 2θ is the scattering angle, and λ is the wavelength) of CaMKK2 (2.3 mg.mL⁻¹, shown as black squares) and the CaMKK2:Ca²⁺/CaM complex mixed at 2:1 molar stoichiometry (2.4 and 5.8 mg.mL⁻¹ shown as blue circles and red triangles, respectively). Guinier plots are shown in inset. (B) Distance distribution functions $P(r)$ calculated from scattering data using the program GNOM (Svergun, 1992). (C) Dimensionless Kratky plots. Red lines mark the maximum at a value of 1.104 for $sR_g = 1.73$, which is typical of scattering data of compact globular proteins (Receveur-Brechot and Durand, 2012). (D) Experimental scattering curve of the complex (at 2.4 mg.mL⁻¹) superimposed with the calculated curves of the ensemble selected by the program EOM (red). (E, F) Distributions of R_g and D_{\max} values of the CaMKK2:Ca²⁺/CaM complex conformations from ensemble selected by the program EOM (Tria et al., 2015).

Figure 6.

Model of the CaMKK2 KD:Ca²⁺/CaM complex. The model was prepared using the program HADDOCK (Dominguez et al., 2003) with the crystal structure of the CaMKK2 KD (PDB ID: 5UY6), the solution structure of Ca²⁺/CaM bound to the CBD of CaMKK1 (PDB ID: 1CKK) (Osawa et al., 1999), and intermolecular distance constraints assessed in chemical cross-linking experiments. The CaMKK2 KD is colored as in Fig. 3A, according to HDX-MS results.

Table 1

Summary of time-resolved fluorescence measurements

	$\tau_{mean}^{a,b}$ (ns)	$\beta_1^{c,d}$	ϕ_2 (ns)	β_2	ϕ_3 (ns)	β_3	ϕ_4^f (ns)	β_4	ϕ_{agg}^e (ns)	β_{agg}	$\beta_{fast} = \beta_1 + \beta_2 + \beta_3$
W128	4.0	0.03	0.9	0.04	3.3	0.02	61	0.13			0.09
W128+CaM	4.0	0.02	1.0	0.03	3.2	0.02	70	0.15			0.07
W267	4.8	0.01	1.2	0.01			43	0.20			0.02
W267+CaM	4.4	0.01	1.6	0.02			67	0.19			0.03
W337	4.6	0.01	1.7	0.03			44	0.18			0.04
W337+CaM	4.1	0.02	1.3	0.03			23	0.08	>200	0.09	0.05
W366	4.2	0.05	2.3	0.03	9.2	0.02	40	0.12			0.10
W366+CaM	4.4	0.04	0.6	0.01	2.9	0.02	22	0.10	>200	0.05	0.07
W374	4.3	0.03					32	0.15	>200	0.04	0.03
W374+CaM	4.3	0.04					42	0.18			0.04
W390	3.8	0.01	1.9	0.03			45	0.18			0.04
W390+CaM	3.9	0.00	2.0	0.03			25	0.11	>200	0.08	0.03

^aMean lifetimes were calculated as $\tau_{mean} = \sum_i f_i \tau_i$, where f_i is an intensity fraction of the i -th lifetime component τ_i .

^bS.D. value is ± 0.05 ns.

^cThe anisotropies $r(t)$ were analyzed for a series of exponentials by a model-independent maximum entropy method.

^dFast unresolved component with $\phi_l < 100$ ps, amplitude β_l was calculated to satisfy the requirement of $r_0 = \sum_i \beta_i = 0.22$.

^eLong correlation time resulting from minor protein aggregation; the exact value is inaccessible with ~ 4 ns Trp lifetime.

^fS.D. value is ± 10 ns.

Table 2

Structural parameters determined from SAXS data.

	c (mg.mL ⁻¹)	R_g^a (Å)	R_g^b (Å)	D_{\max} (Å)	V_p^c (nm ³)	$M_w^{d,f}$ (kDa)	$M_w^{e,f}$ (kDa)
CaMKK2	3.0	32.3 ± 0.3	32.4 ± 0.3	125	93.7	47 ± 1	59
	2.3	32.3 ± 0.3	32.5 ± 0.3	126	98.4	46 ± 1	62
Ca ²⁺ /CaM	3.9	22.2 ± 0.1	22.2 ± 0.1	71	27.6	20 ± 1	17
	1.9	22.2 ± 0.3	22.3 ± 0.1	67	28.1	21 ± 1	18
Complex (1:1)	5.8	38.4 ± 0.5	38.6 ± 0.5	124	112.1	66 ± 1	70
	2.4	37.1 ± 0.4	37.3 ± 0.4	120	110.0	64 ± 1	69

^aReciprocal space radius of gyration (R_g).^bReal space R_g .^cThe excluded volume of the hydrated particle (the Porod volume).^dMolecular weight estimated by comparing the forward scattering intensity $I(0)$ with that of the reference solution of bovine serum albumin.^eMolecular weight estimated from the Porod volume ($M_w \approx V_p \times 0.625$) (Petoukhov et al., 2012).^fTheoretical molecular weights of CaMKK2₉₃₋₅₁₇, Ca²⁺/CaM and the CaMKK2₉₃₋₅₁₇-Ca²⁺/CaM complex (with 1:1 stoichiometry) are 48, 17 and 65 kDa, respectively.

Table 3

Intermolecular cross-links between CaMKK2 and CaM obtained with DSG and DSS.

		Cross-linked peptides		Cross-linked residues	Observed mass	Theoretical mass	Error (ppm)	C_{α} - C_{α} distances from the model (Å)
		CaMKK2	CaM	CaMKK2-CaM				
DSG ^a	1	493-494	128-149	K493-K149	2888.31	2888.31	0.40	15.7
	2	430-448	76-78	K441-(K76, K78) ^b	2787.53	2787.53	-1.03	16.6, 19.9
DSS ^a	3	493-494	128-149	K493-K149	2930.36	2930.36	0.06	15.7
	4	493-494	77-87	K493-K78	1792.87	1792.87	0.19	28.5
	5	430-448	76-78	(K441-K76, K78)	2829.58	2829.58	-1.30	16.6, 19.9
	6	243-250	1-14	K250-K14 ^c	2769.37	2769.37	0.57	24

^aDSG, disuccinimidyl glutarate; DSG, disuccinimidyl suberate^bIncludes oxidation at CaM Met77^cIncludes acetylation and oxidation at CaM Met1

Figure 1

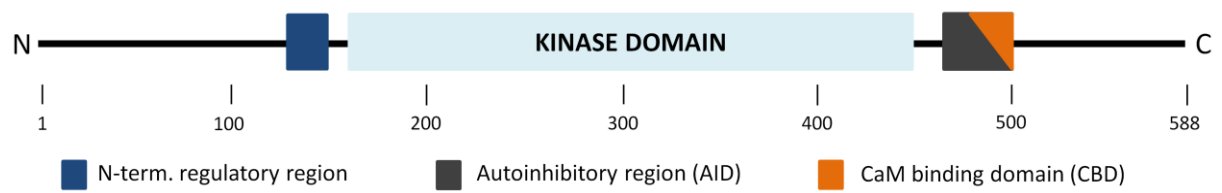


Figure 2

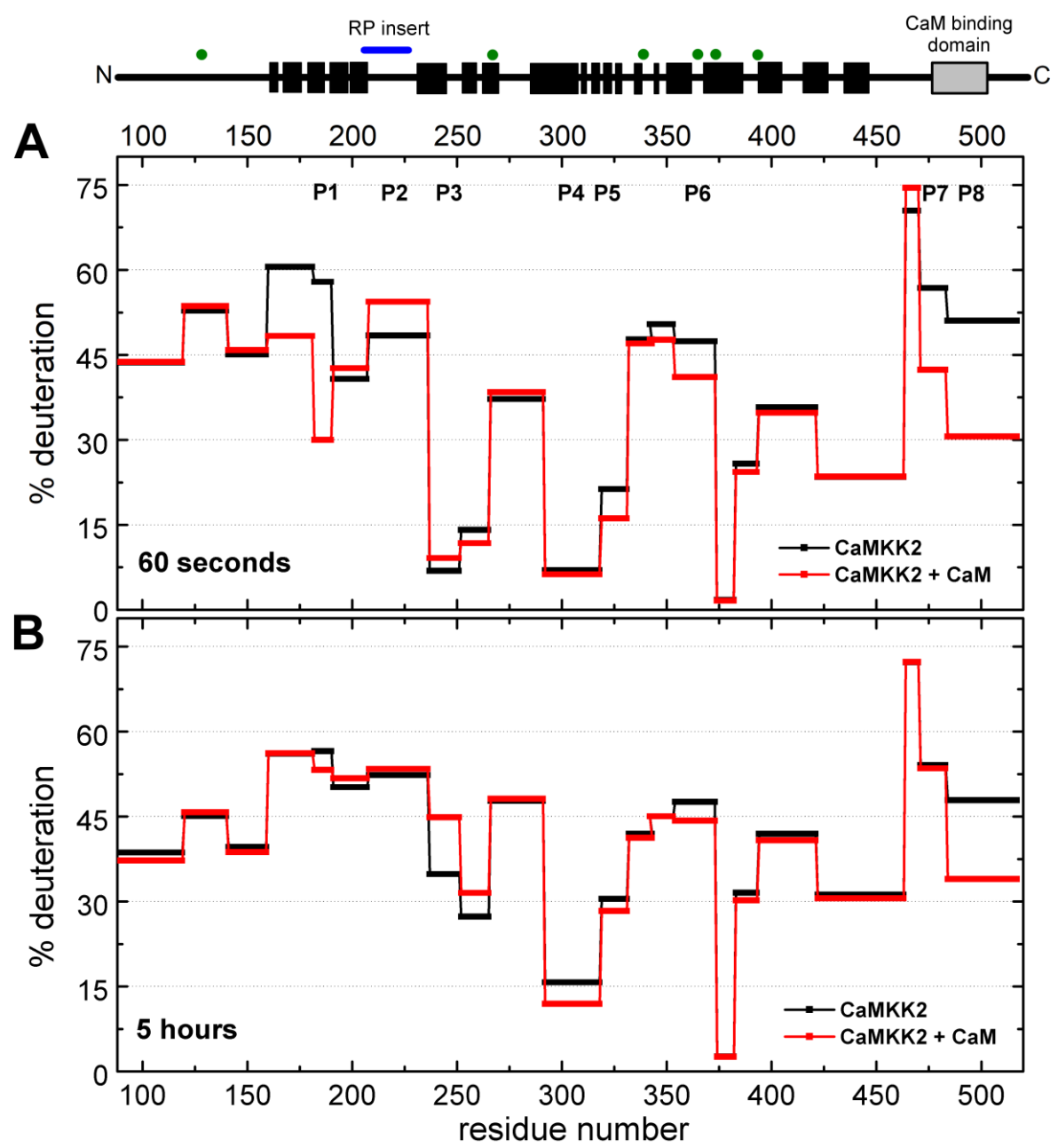


Figure 3

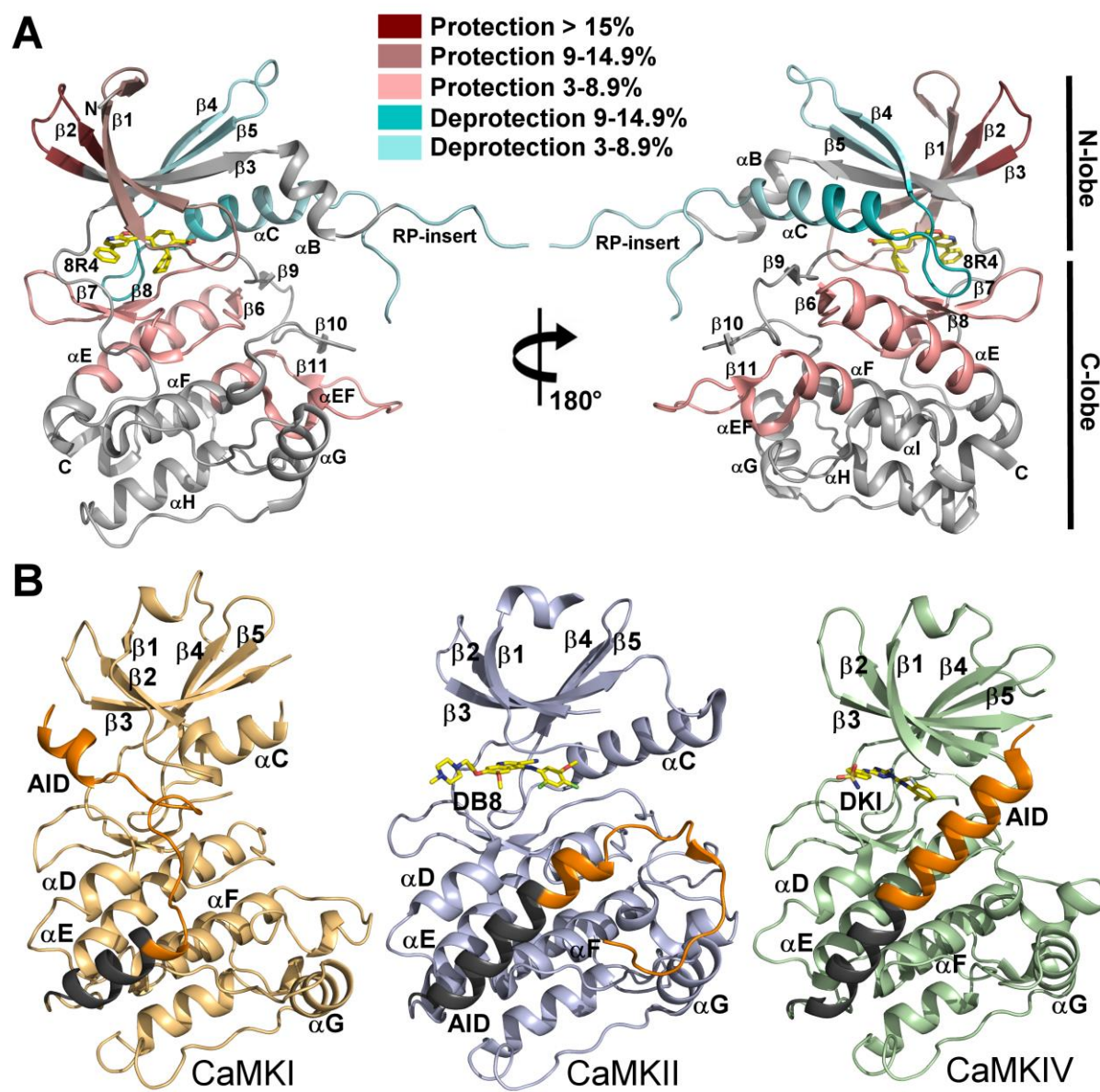


Figure 4

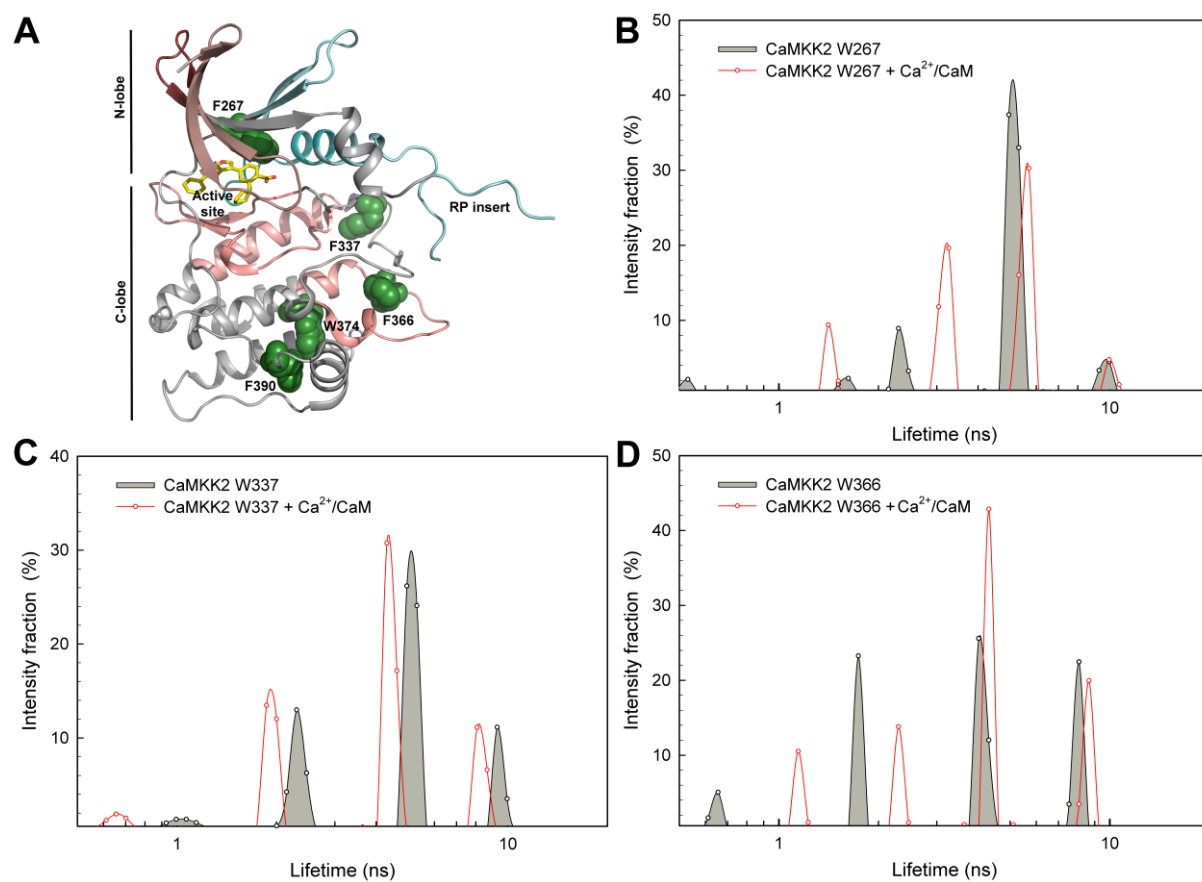


Figure 5

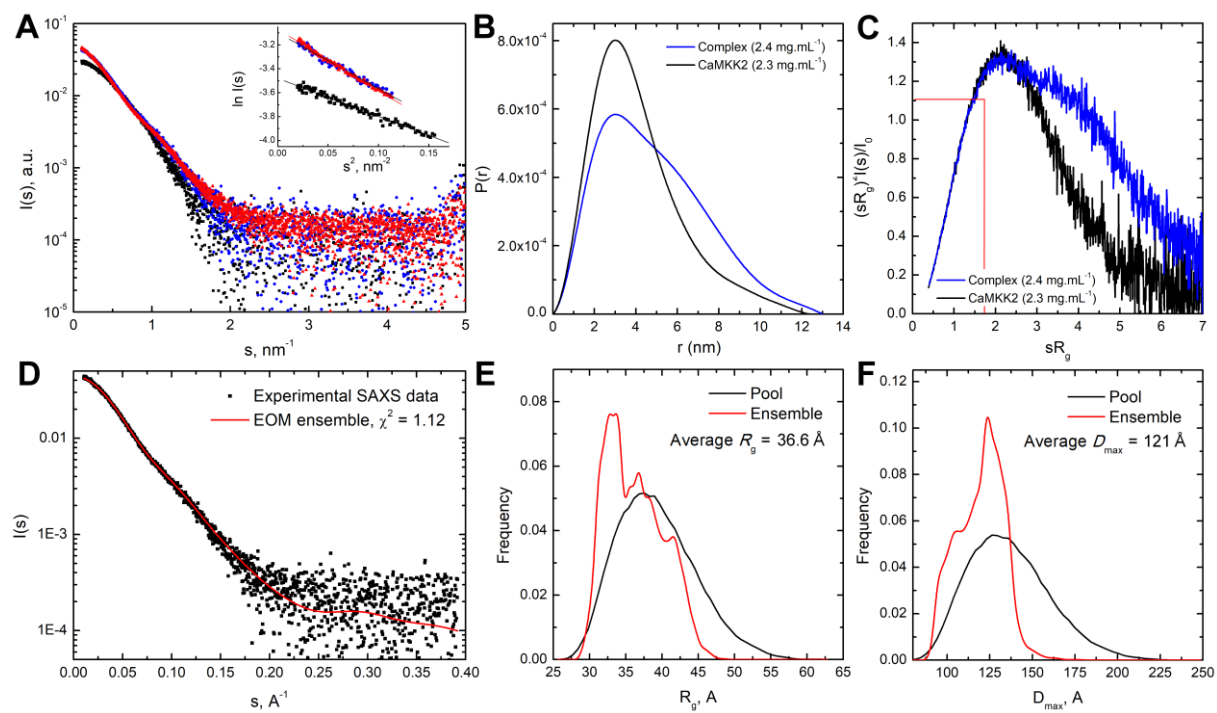
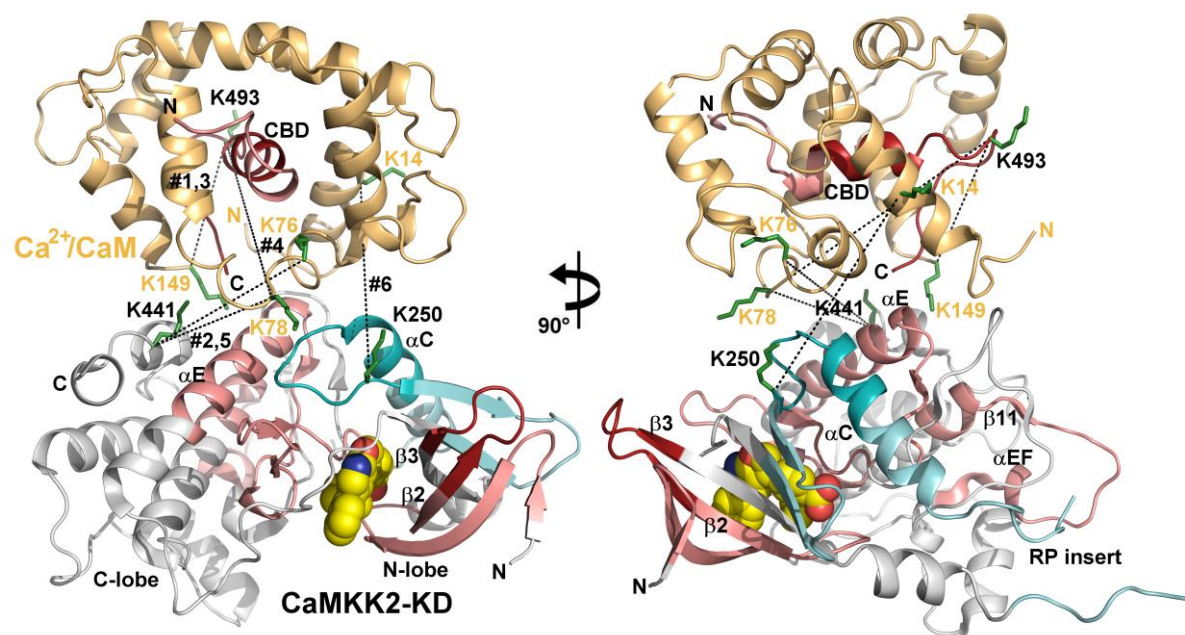


Figure 6



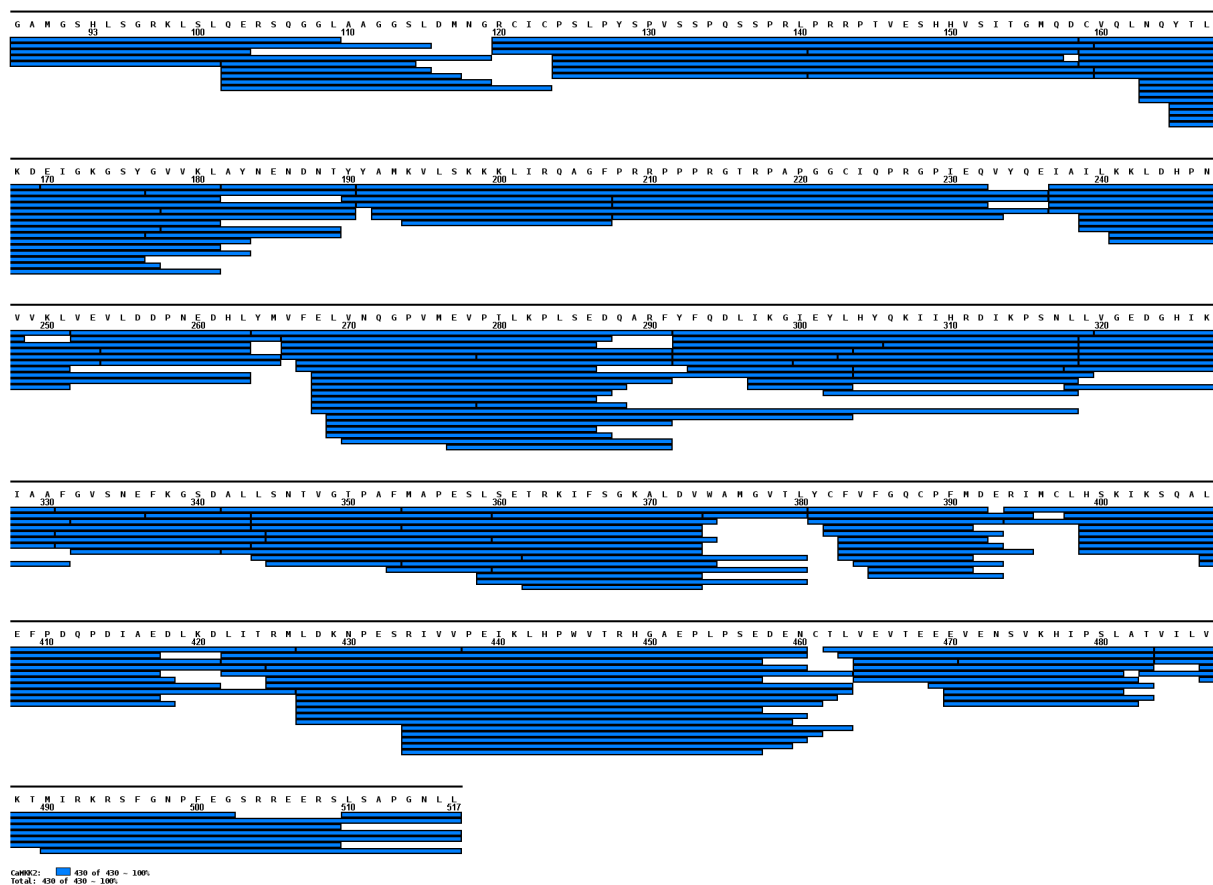


Figure S1. Related to Figure 2.

Peptide mapping of CaMKK2 after digestion with immobilized pepsin. All peptides identified by ESI-FT ICR-MS/MS analysis are shown as blue bars. The residues are numbered according to the native sequence (the first five residues are from the tag).

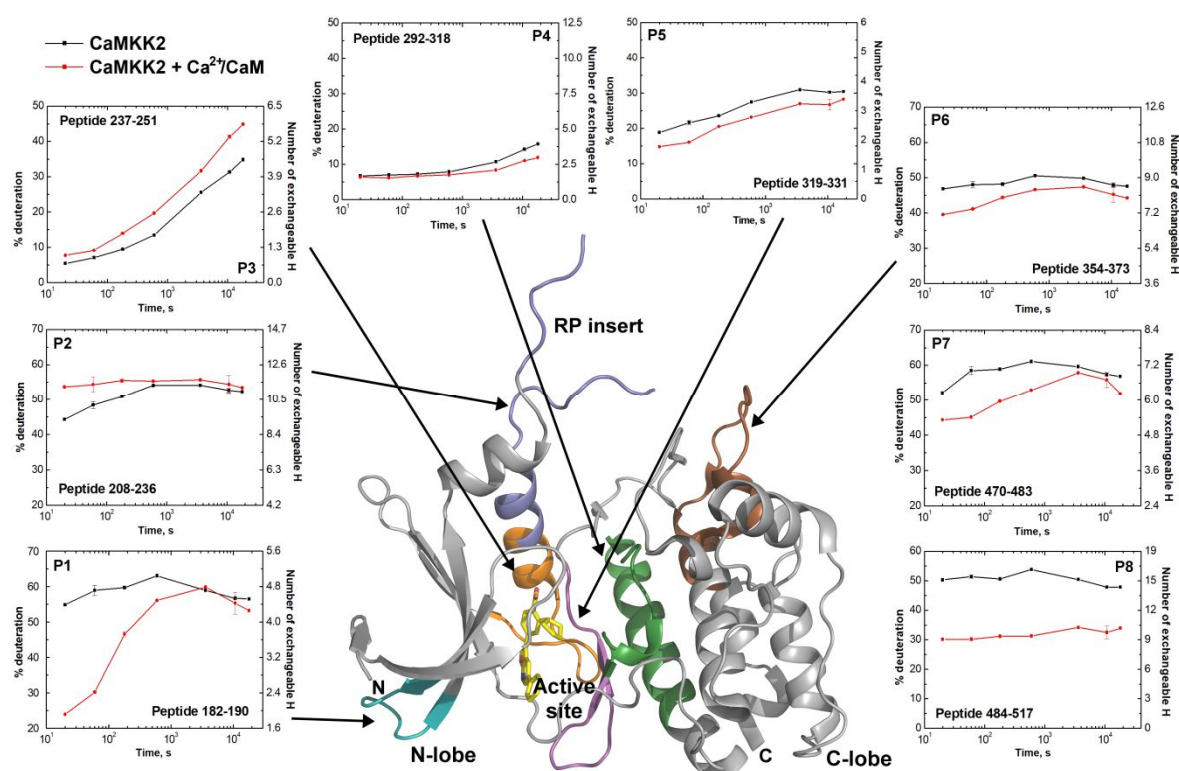


Figure S2. Related to Figure 2.

HDX kinetics for selected CaMKK2 peptides. The graphs represent the HDX kinetics of selected CaMKK2 regions that show changed deuterium exchange kinetics upon Ca²⁺/CaM binding. Deuterium exchange is expressed as percentages relative to the maximum theoretical deuteration level (left vertical axis) as well as a number of exchangeable protons (right vertical axis) of selected CaMKK2 peptides alone (black squares) and in the presence of Ca²⁺/CaM (red circles). The regions of the kinase domain (peptides P1–P6) are mapped on the surface representation of the CaMKK2 KD crystal structure (PDB ID: 5UY6).

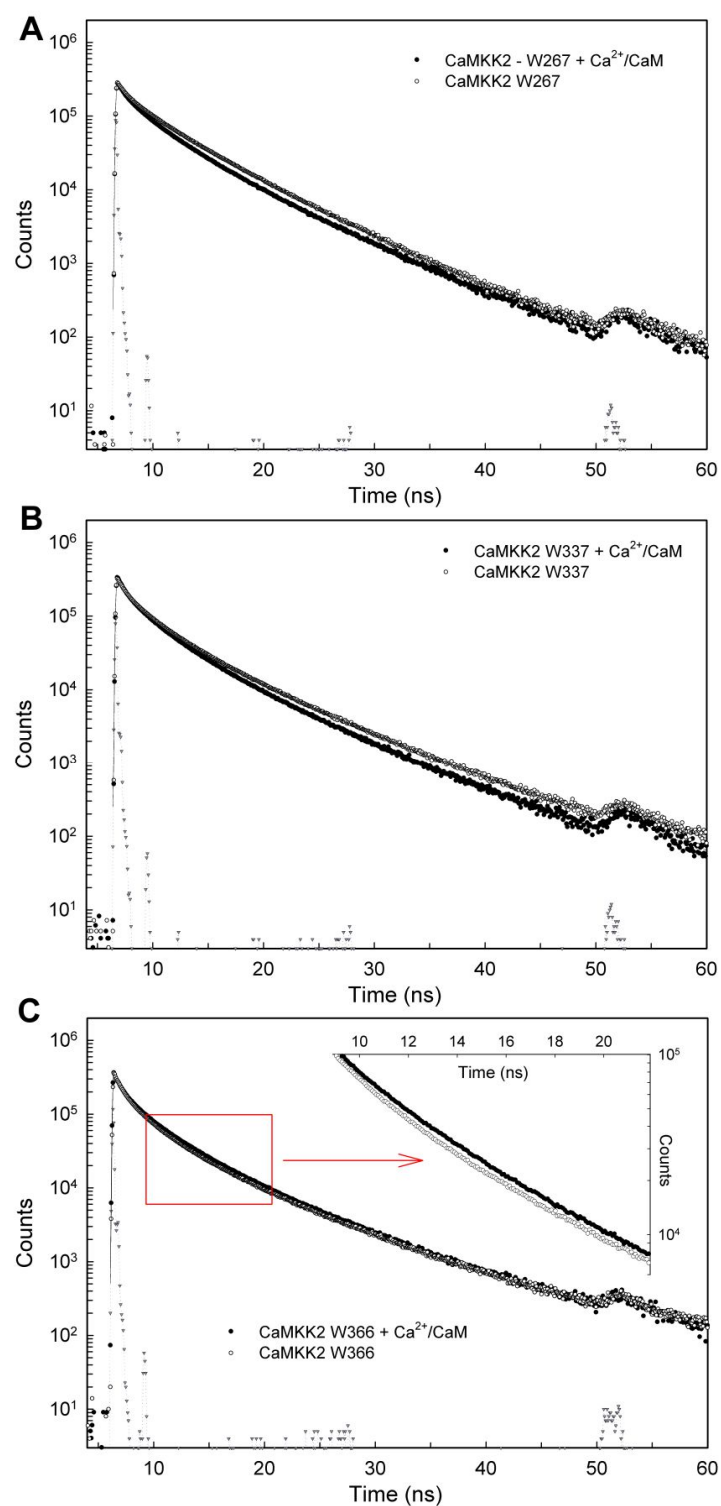


Figure S3. Related to Figure 4.

Time-resolved tryptophan fluorescence measurements. Fluorescence intensity decays of CaMKK2 W267 (A), CaMKK2 W337 (B) and CaMKK2 W366 (C) mutants in the absence and the presence of Ca^{2+} /CaM.